The Dissertation Committee for Yin Wu Certifies that this is the approved version of the following dissertation:

A NEW OPERABILITY AND PREDICTABILITY ENHANCED RISER CONTROL SYSTEM FOR DEEPWATER MARINE OPERATION - AN INTEGRATED RISER HYBRID TENSIONING SYSTEM

Committee:

Ross Baldick, Supervisor

Alexis Kwasinski

Surya Santoso

Thomas Edgar

Zhigang (David) Pan

A NEW OPERABILITY AND PREDICTABILITY ENHANCED RISER CONTROL SYSTEM FOR DEEPWATER MARINE OPERATION - AN INTEGRATED RISER HYBRID TENSIONING SYSTEM

by

Yin Wu, DIPLOME; B.E.; M.E.; M.S.E.

Dissertation

Presented to the Faculty of the Graduate School of

The University of Texas at Austin

in Partial Fulfillment

of the Requirements

for the Degree of

Doctor of Philosophy

The University of Texas at Austin

December 2015

Dedication

To my father Haixiang Wu and my mother Jiming Chen

for their unconditional love and support

Acknowledgements

This thesis represents the main results of my doctoral studies. I would like to express my appreciation to the many that made it possible.

First of all, I would like to express my gratitude to my advisor Prof. Ross Baldick for the continuous support of my Ph.D. study. I would like to thank you for his guidance and enthusiastic encouragement, for always backing me up. I am extremely grateful to his patience and trusting in my capabilities to complete the work presented herein. The flexibility and support from him allowed me to keep working in the area that I am enthusiastic about. Thanks to his patience and guidance on my primitive writing.

I also very much appreciate my committee members, Dr. Alexis Kwasinski, Dr. Surya Santoso, Dr. Thomas Edgar, and Dr. David Pan, for agreeing to serve on my committee and for their precious time to read my dissertation and their valuable input towards this works. I am very grateful to Dr. Jeffrey Bennighof, for his patient explanation on the modern modal analysis on the mechanical beam structure. It opens the door for me to exploit the vortex-induced vibration suppression method.

I offer my appreciation to Transocean Deepwater Drilling Inc, for supporting this research. I thank for the financial support of my attendances of OMAE conferences.

I convey special acknowledgement to my manager, Ed Bourgeau. Accepting me as a full time electrical engineer and part time PhD student, Ed opened the door to this journey in May 2010. His creativity inspires me to put into this research topic, his deep understanding of marine operation and higher level vision guided me through every step of difficulties. I heartily thank him for the freedom he gave to pursue this project besides regular routine engineering work of company. Without his support, I would not be able to go through this whole journey.

I would also like to thank my colleagues Aaron Barr, an excellent mechanical engineer, for his selfless sharing of knowledge on modeling and system operation. I am grateful to Dr. Philips Zhang for his guidance. His expertise on understanding of the physical system has been

invaluable help. John Kozicz should be thanked for his inspiration of innovative ideas on motion stabilizer for Drill Stem Test and his support and wide connection within this industry.

Many thanks go out to my school mates, Sheng-yang Yu, Thekla Boutsika and Yohan Sutjandra and other students I got interact during my years in UT. I am especially thankful to Ruichen Zhao for his inspiration and help on my control design theory in my first year after resuming this study.

I would like to express my gratitude to people in the Hohai Univerisity. Thanks to Prof. Xingying Chen for her guidance on my Master study on power grid dynamic stability. Thanks to Prof. Ping Ju and many others who guided and gave generous opportunities along the journey since my undergraduate study.

I am really indebted to my parents – Jiming Chen and Haixiang Wu, to whom this dissertation is dedicated to. The unconditional love and support is indeed my backbone to fight through every difficulty I had since I started this journey of my dream. Their encouragement makes me to decide finishing this dissertation and their support for baby-sitting their grandson since he was born gives me time to stay in office until 10pm in night.

And to my son, Lucas, without his birth, I would not understand the meaning of responsibility on my shoulder. Lucas, hope you would understand one day that all the work I did is for building a safer and more stable home for you to grow up happily and successfully. Mom loves you so much!

A NEW OPERABILITY AND PREDICTABILITY ENHANCED RISER CONTROL SYSTEM FOR DEEPWATER MARINE OPERATION - AN INTEGRATED RISER HYBRID TENSIONING SYSTEM

Yin Wu, Ph.D.

The University of Texas at Austin, 2015

Supervisor: Ross Baldick

This dissertation presents a novel riser hybrid tensioning system by integrating an electrically powered riser tensioning system into existing hydro-pneumatic tensioners. Compared to current passive hydro-pneumatic tensioners, this new riser hybrid tensioning system provides the capability of dynamically controlling the tension in the riser string. This feature opens a wide horizon of different active riser control strategies to achieve the systematic riser control solution. The objective of this study is to increase the predictability and safety of the whole riser system, and to extend the operability of the riser tensioning system into other operations.

An overall structure framework of this novel hybrid riser tensioning system is proposed, comprising a direct driven electrical tensioners, hydro-pneumatic tensioners, a super-capacitor based energy storage system, power dissipaters, an overall tension controller and a power management controller. Hardware configurations are suggested. A riser data logging system is introduced, providing more comprehensive riser status data. A power management control strategy and overall coordination architecture to integrate the whole system are proposed.

As the main functionality of the riser tensioning system, a new active heave compensation control strategy is analyzed in detail, by using this new riser hybrid tensioning system. A LQG controller and a H_∞ controller are designed. The position chasing technique produces predictive and accurate tension commands for the electrical tensioners. Both Matlab simulation and hardware implementation confirm the feasibility of this concept, and further

verifies that a more accurate control performance could be achieved by the electrical tensioners 180° compensating the tension fluctuation caused by the hydro-pneumatic tensioners.

A novel testability and predictability enhanced anti-recoil control algorithm is implemented in the electrical tensioners. A position control strategy is proposed with the objective of moving the riser body to a desired elevation height in a predictive manner. A system model and a Kalman estimator are built, and a LQG controller is designed. The simulation demonstrates that the riser lifting height can adjust to any reasonable value for different test environment. This anti-recoil control concept reduces the risk of catastrophic damage, and allows us to perform maintenance tests much more frequently to bring back operator's confidence.

During harsh sea state, the VIV can be suppressed by using the dynamic control of the hybrid tensioning system, at frequencies and magnitudes made available by the electrical tensioning system. The objective is to achieve the VIV suppression by avoiding the excitation of the oscillation locking into the resonance conditions, and by reducing oscillation energy to be built in riser. A modal analysis of a tensioned Euler-Bernoulli beam is studied. Two control methods are proposed. Simulations results demonstrate that the oscillation is effectively reduced at the dominant lock-in frequency.

Finally, this riser hybrid tensioning system opens the possibility to extend the tensioning system operability into other drilling operations. A motion stabilizer supporting the heave compensation of the drill pipes and the DST tools can be eliminated by connecting the drill pipes onto the telescopic joint. Another application would be that the electrical tensioners can run under position control mode after the riser is recoiled and soft hang-off on tensioners. The riser string position with respect to the seabed can still be controlled, during the vessel moving among different well heads.

Table of Contents

List of Tables

List of Figures

Chapter 1: Introduction

1.1. Background and Motivation

Offshore petroleum exploration began in the shallowest waters. As these reservoirs are exploited together with an increasing demand for oil and gas, the petroleum industry has been moving to ever deeper waters and harsher environments. Meanwhile, a wide variety of challenges have emerged over the past two decades. One among them is the ensuring with the performance and safety of the drilling riser in ultra-deep water.

1.1.1. Introduction of Hydro-Pneumatic Tensioner

Deepwater riser system, shown in Fig. 1.1, connecting the subsea blow out preventer stack (BOP) to the rig surface is necessary for circulating mud and cuttings and is an outer protection system of the drilling pipes and drill bit. It allows drill pipe, logging tools and multiple casing strings to pass through, and also provides a returning circuit for auxiliary lines such as high pressure choke and kill lines for circulating fluids from BOP to surface, and usually subsea power and well control lines, mud boost and hydraulics of BOP controls [1]. Drilling operations are conducted inside the riser pipe. The riser might be loosely considered as a temporary extension of the wellbore to the surface.

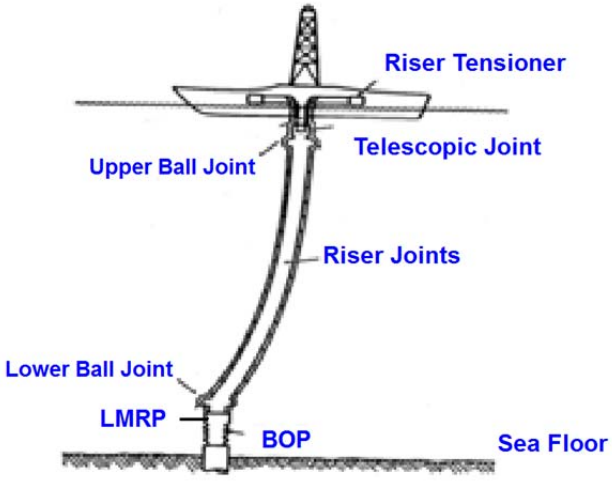

Fig. 1.1 Riser System for a Floating Drilling Rig

A riser tensioning system aims to keep the riser string in near constant vertical axial tension, while compensating for relative motions between the floating rig and the seabed that are joined by the rigid riser string. The total tension applied on the top of riser is the sum of multiple tensioners, usually 6-16 tensioners depending on the water depth, the riser weight, etc. Tensioner units are normally located on the drilling vessel near the periphery of the drill floor in a circular pattern. And the tensions balance each other and keep the riser in the middle of the moon pool, even in condition of the vessel drifting off its wellhead location, as shown in Fig. 1.2 and Fig. 1.3.

Fig. 1.2 Wire-line Type Hydro-Pneumatic Riser Tensioners

Fig. 1.3 Direct-Acting Type Hydro-Pneumatic Riser Tensioners

According to [2]-[4], nowadays the hydro-pneumatic tensioning system is the most widely used. It typically consists of hydro-pneumatic tensioner cylinders, gas/oil accumulators, gas pressure vessels, anti-recoil valves and central control console.

- Riser Tensioner Cylinder

The riser tensioner cylinders provide nearly constant tension to the riser string in order to counter balance of the combined wet weight of the riser pipes and mud. It usually provides around 15m of wire-line travel, with the cylinder diameter of 470mm. The lower side of cylinder contains high pressure hydraulic fluid. The tension on the wire-line is maintained by oil pressure in this side of the cylinder from the oil/gas accumulator pressurized by gas. A low pressure gas/oil reservoir is mounted on the tensioner. Low pressure oil is piped to the higher end of the cylinder. This provides continuous lubrication, system damping and safety control. The tensioner cylinders usually sit on the Mezzanine deck around the moon pool in pairs.

- Oil/Gas Accumulator

The high gas pressure accumulator provides the interface between the high pressure hydraulic fluid in the cylinder and the high pressure gas in the Air Pressure Vessels. The gas volume is selected to deliver the required tension conformed by engineering design. The accumulator is usually mounted beside the cylinder, to keep the hydraulic piping between the cylinder and accumulator short.

Fig. 1.4 Tensioner Cylinder and Accumulator

- Air Pressure Vessel (APV)

The riser tensioner system utilizes air pressure vessels to provide the correct stiffness of the system. APVs act as an energizer that can be compared to an enormous pneumatic spring. The large volume will ensure a "nearly constant" tension. It is very common that each tensioner cylinder is equipped with 3 APVs individually. All these APVs are connected on the air line, and the gas pressure of the APVs could be adjusted by charging or releasing air. The APVs are usually grouped together sitting at several locations of the main deck.

Fig. 1.5 Direct-Acting Type Hydro-Pneumatic Riser Tensioners

- Anti-Recoil Valve

Positioned between the accumulator and the tensioner cylinder port, this orifice type valve limits the amount of hydraulic fluid that can flow into the tensioner, thus limits the extension velocity of the tensioner ram, during emergency disconnect event, as shown in Fig. 1.6. During normal operation, this valve is fully opened allowing unrestricted flow between the accumulator and the tensioner cylinder.

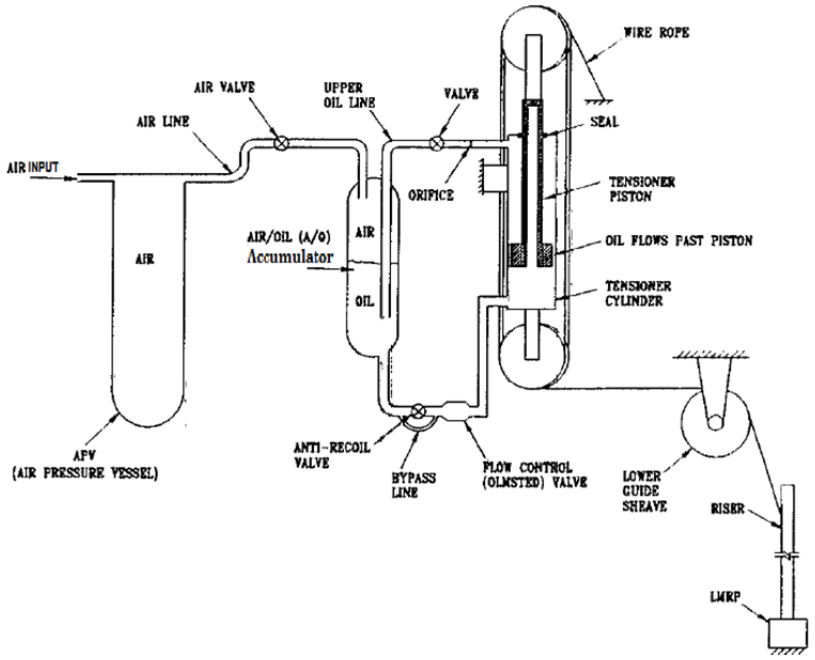

Fig. 1.6 The Main Components of a Hydro-Pneumatic Tensioning System

- Tensioner Operation Control Console

The tensioner control console monitors and controls the operation and function of the entire riser tensioning system, which involves all mechanical valves, pumps, fans and communication with riser system control console. All the control algorithms are commonly implemented in a PLC (Programmable Logic Controller).

1.1.2. Operation Modes and the Pros and Cons of Hydro-pneumatic Tensioner

Two operation modes are typically implemented in hydro-pneumatic tensioners [5].

(1) Heave Compensation Mode (Normal Operation Mode)

This mode operates during regular drilling operation, after the riser string is fully deployed in water and the LMRP is firmly connected on the BOP or the BOP is connected on the wellhead. This mode allows the riser string keeping motionless with respect to the seabed, while ocean heaves driving the vessel to move cyclically up and down. As the vessel heaves upward

on a wave, the air pressure in the oil/gas accumulators causes the tensioners to stroke out for preventing over-tension in the wire-line. Downward heaves cause the tensioners to retract for maintaining the desired tension on the marine riser.

One of the safety problems that confines drilling industry for deeper water and harsher environment is the vortex-induced vibration (VIV). VIV is a flow induced vibration caused by the shedding of vortices on a riser, when the current flow exceeds a certain speed [6]. Fig. 1.7 shows a 2D laminar description of a typical VIV. Risers subject to constant harsh current environment, such as the Gulf of Mexico, North Sea, etc, are always facing the challenge of the deep water high speed loop current [7]. The VIV not only can lead to fatigue damage in the riser connections, but also depending on the magnitude of the vibrations, significant stresses can break the riser connections and cause destructive consequences [8].

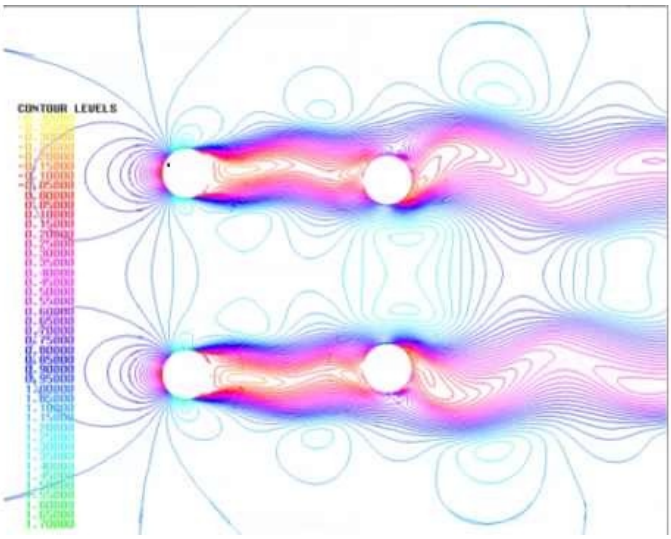

Fig. 1.7 The Vortex-Induced Shedding on Marine Riser

As shown in Fig. 1.8, nowadays, for deep water drilling operation under condition of severe lateral vibration, the drilling operation has to be suspended immediately at time t_1. If the VIV becomes more severe that may threat the riser pipe from parting, an emergency disconnect between the LMRP and the BOP has to be conducted at time t_2. And the riser has to be recoiled

and securely hang-off of the vessel. In case that the riser is disconnected from the BOP, the drilling suspension time duration could be much longer than that of riser maintaining connected, because the environmental criterion for riser reconnection is much more stringent. Reconnecting the LMRP back onto BOP requires the harsh current condition subsides substantially until a much lower level. Therefore, the riser disconnection which means more rig "down" time, is the worst circumstance for both drilling contractor and operating company. This is not only a significant step function of the spread cost, but also a huge risk for mechanical and environmental issues. Every time the riser is disconnected from the bottom, the mud column and other hydraulic fluid has to been disposed into water and it also causes the risk of broken gaskets in the riser column which may take even longer time to resume drilling.

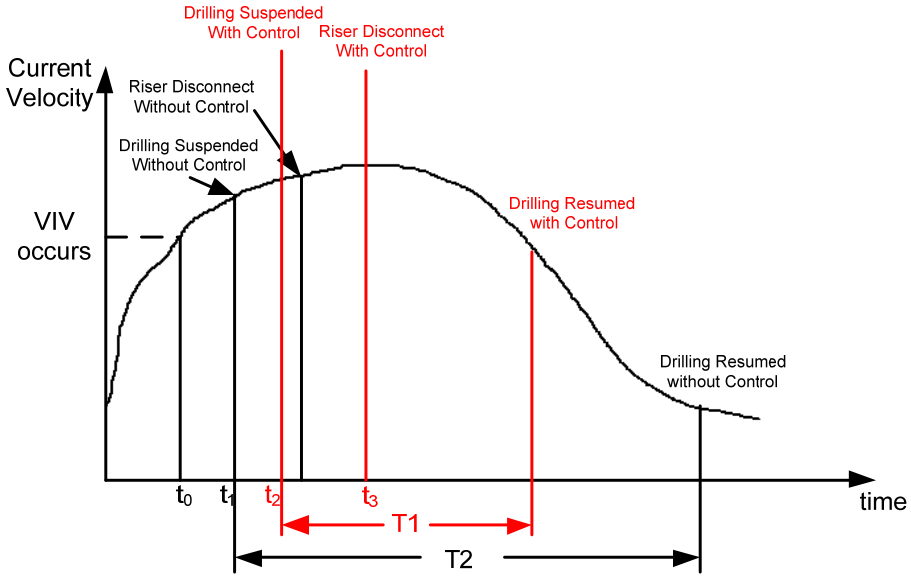

Fig. 1.8 Drilling Suspension Comparison Demonstration

In order to suppress VIV, one of the currently used control method is to increase longitudinal over-pull tension at the top end of riser [2][9] in order to stiffen the flexible pipe structure, thus to avoid the vibration frequency points. This over-pulling tension is provided by

the hydro-pneumatic tensioners in addition to the weight of the riser pipes and the circulating mud.

Another problem of the current hydro-pneumatic tensioning system is that it is actually a passive control system, which can only provide two statuses, either on or off. Thus the functionality of this large-volume hydro-pneumatic tensioning system is in fact very limited. Only after the riser is fully deployed in water and the LMRP is securely connected on the BOP or the BOP is securely connected on the wellhead using the drawworks with active heave compensation capability, then the riser is switched over to the hydro-pneumatic tensioners providing constant pulling force and the drawworks is free for other activities. In all, this hydro-pneumatic tensioning system can only be used in case that the bottom of the riser is engaged in the borehole. And it is not able to provide active position control in case that the bottom of the riser is not connected and the riser string is hanging freely on the tensioners.

(2) Anti-Recoil Mode

The riser recoil scenario occurs after a planned or an emergency riser disconnect, when the vessel heave exceeds certain height, the drill ship loses its ability to maintain position over the wellhead, or the riser fails (parts). It is necessary to disconnect the riser at the connector between the Lower Marine Riser Package (LMRP) and the BOP. The energy in the riser and in the tensioning system is very large at this point, especially when drilling conditions call for high tension requirements. Releasing the riser connector under these conditions transfers this energy into a rapid lifting force. The anti-recoil operation mode aims to maintain this riser recoil process in a controlled manner.

First of all, as a typical mechanical system, its core limitation is its slow response cycle. The operational experience has shown limitations of this anti-recoil system using a hydro-pneumatic tensioning system. Slow operation of pneumatic system and mechanical switches and valves usually manifests in a longer control response time than the requirement. In the hydro-pneumatic world, if we suppose the fluid or gas flows in an infinite free space, then changing oil

flow rate or air pressure is easy and instantaneous. But in practical, mechanical switches and valves put the fundamental bottleneck for system response speed.

In order to change the wire-line tension delivered by each tensioner, one method is to change the air pressure. To increase the tension setting, air pressure is increased by opening the air valves of the accumulators and the APVs to the higher pressure backup bottles. To decrease the tension setting, air pressure is vented from the accumulators and APVs into empty receiver [4]. To our knowledge [5], on the modern deep water class drilling rig, each tensioner usually comprises three 685 gallon APVs of rated 3000psig and four air valves. Either pumping or venting gas is very slow, can take more than 20 minute for changing 1000 psig in three APVs. And if the pressure increases exceeding the rated capacity of the valve, a rupture disk will vent the excessive gas to the atmosphere at 660 psig which wastes even more air pressure. This method is only suitable for long term planned tension regulation.

Another method that is relatively faster for the riser emergency disconnect scenario, is to change the tensioner cylinder's stiffness to limit the riser recoil distance. At this point, the anti-recoil valve, as seen in Fig. 1.6, located between the cylinder and the accumulator is activated upon receiving an electrical signal from the limit switches in the tensioner stroke. Once the anti-recoil valve is closed, local oil flow of the cylinder is isolated from the accumulators. Meanwhile, the fluid continues to flow in the bypass line for reducing the pulling force on the riser. However, the changing rate of this pulling force is usually very slow, in the range of second. At the moment of riser disconnect, the large amount of captured potential energy in riser, wire-line and tensioner is suddenly released, but the slowly changed large over-pulling force is still applied at the top. It accelerates free riser pipes to jump out, hit the drill floor, damage the riser top, the drill floor and the more sophisticated flexible joint, etc. Then the riser string is dragged down by its own mass gravity, breaking the pipe joints in the middle and falling on the BOP. Fig. 1.9 shows the rope slack of one tensioner after riser recoil [42]. This is a catastrophic consequence that can cost more than 2 months of drilling down time, billion dollars

financial loss of both the drilling contractor and the well operator, and also a potential environmental disaster.

Secondly, the detection system of riser recoil poses big safety concerns. The current detection of the emergency riser recoil situation is barely functional. It relies on the big changing rate of the hydraulic fluid flowing between the cylinder and the accumulator. If the flow rate exceeds a certain criterion, the emergency anti-recoil mode is activated. However, the time gap from the riser bottom disconnect to the flow rate change puts a big delay for activating the anti-recoil process. If the whole riser recoil process is toughly 10s, then this time gap could take around 4-5s. Moreover, this flow rate can be influenced by many factors, even an abnormal big wave heave may retract the cylinder making the flow running faster from the cylinder into accumulator. Therefore, even though the modern dynamic positioned deep water drilling rig is equipped with this recoil detection system, it is not really useful during real emergency situation. In 2005, when a critical incident of riser parting occurred on a Transocean deep water rig, the riser recoil detection system was not able to function at that moment.

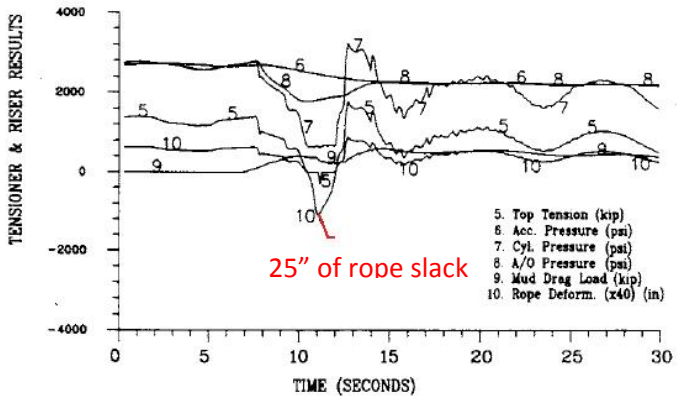

Fig. 1.9 Rope Slack during Riser Recoil Scenario

Finally, the testing of this hydro-pneumatic tensioning system and its anti-recoil system is very difficult and expensive; hence the performance during riser emergency recoil scenario is very unpredictable. By the nature of this hydro-pneumatic tensioning system, it only functions

when the bottom of the riser engaged in the borehole. For factory testing purpose of new built rigs, first of all, a test well has to be constructed in the ocean near shipyard. Then all the subsea equipment has to be lowered in water and connected onto seabed. Finally the anti-recoil system can be tested by disengaging the LMRP from BOP. This anti-recoil test itself not only is a high cost, low efficiency activity, but also has high potential of causing catastrophic damage in many aspects. Thus the test is hardly conducted before actual deployment. Thus the performance of this hydro-pneumatic tensioning and its anti-recoil system is very unpredictable and gives rig crew low confidence during real emergency situation.

Additionally, the hydro-pneumatic tensioning system requires high maintenance costs. According to [10], [11], operational experience with the cylinders has shown severe damage caused by external/internal forces in combination with corrosion, wear and fatigue after only a few months or after a few years of operation at best. Offshore maintenance work and replacement of such large piston rods in a harsh environment and on remote locations is resource demanding and extremely costly. And moreover, the significant volume of cylinders and APVs consumes the precious floor space around the moon pool.

1.2. Scope of this Research

In order to accommodate the above described safety and operability problems of current hydro-pneumatic tensioners, we proposed a research project of a novel riser hybrid tensioning system, which integrates a new electrical tensioning system into the existing hydro-pneumatic tensioning system. By using suitable control strategies on electric machines, the electrical tensioners would be capable to deliver the dynamically changed wire-line tension within mille-second. This new hybrid riser tensioning system aims not only to fulfill the active heave compensation functionality, but also to realize an enhanced system solution of dynamic tension control of the deep water riser string that helps to overcome a wide range of barriers encountered

in deep water drilling operations. The overall objectives of this project can be divided into the following:

1.2.1. Increasing the predictability and safety of the riser system

(1) More accurate active heave compensation

Nowadays, an induced cyclical force by the pressure change in hydro-pneumatic tensioners always exists on the riser, which may cause riser fatigue problem in vertical direction. By integrating electrical tensioning system into current passive hydro-pneumatic tensioner, we are aiming to eliminate this cyclical force by applying an 180° opposing force on the electrical riser tensioners. Hence more accurate and stable tension control is obtained. After theoretical research and experimental study, it can be fully confirmed that the modern electric machine control technology and power electronics technology provide us the confidence to achieve this objective.

(2) More predictable anti-recoil control

In order to overcome the above mentioned problems, a novel anti-recoil control strategy using the hybrid tensioning system is proposed in [12][14], by applying dynamic controlled tensions. There is no additional equipment needed.

The new control strategy relies on the position control of the riser string. The control objective would be to keep the riser recoil process in a dynamic profile window: (a) maintaining the air gap between the riser top and the vessel drill floor in an acceptable distance; and (b) lifting the base of the LMRP clear from the top of the BOP above a certain distance.

An improved riser-recoil detection method is proposed by adding a motion reference unit at the top of the riser. This method aims to physically detect the riser disconnect speed and timing, would be a more direct and less delayed recoil detection system.

If the confidence level of correct operating this system decreases exponentially after one successful test, the conventional anti-recoil system is one of the equipment that is not trusted at

all. But, the new anti-recoil strategy using the hybrid tensioning system would give operator the great flexibility to make frequent maintenance tests of such a massive system, without potential damage. The testing of the anti-recoil system would become much easier by using the electrical tensioning system. The displacement level is fully controllable, depending on different test environments. Furthermore, we could easily conduct the "hardware in the loop" test for each pair of electrical tensioners one by one, even they are fully under operation. By continuous testing of this new hybrid tensioning system, a more predictable performance would give people more confidence to operate. And eventually the anti-recoil system would become a safer process.

(3) Reducing fatigue on the riser string:

For Vortex-Induced Vibration, instead of over-pulling the tensioners to stiffen the riser structure or adding other cumbersome mechanical equipment, we could simply use the electrical tensioners to apply dynamically changing tensions to alternate the vortex induced force magnitude or frequency, and therefore to avoid the riser lateral movement from entering into resonant conditions. This method would become an effective and cost efficient way to control the riser stress.

During harsh weather and high current conditions, the first objective of the VIV suppression control in this project is to decrease the VIV magnitude and frequency in order to increase the allowable drilling time to t_2 under more severe environment, as shown in Fig. 1.8. After the VIV becomes too severe for the rig to continue drilling, the next objective of this VIV control is to release the stress on the riser enough to maintain the riser connection to the bottom, therefore, to extend the amount of time between the drilling suspension and the actual riser disconnect at t_3, and further to reduce the frequency of riser disconnection. As a benchmark, a typical deep water drilling riser in 2000m of water is recoverable in a 72-hour period. Note the importance of such timings in hurricane season when event occurrence predictions can be of similar timings. If we can manage to remain connected, once the current condition drops off, we can resume drilling much sooner than the scenario of riser disconnected. The combination of

these initiatives would increase the overall drilling time, reduce the risk and the cost, and improve overall performance.

Furthermore, with the cooperation of the Dynamic Positioning system, we could shift the riser string stress point by driving the vessel in a permitted diameter area. In this way, the most severe current shedding induced on the riser string could be shifted along the riser pipes. Therefore the overall stress on one particular point could be reduced, the overall fatigue life of the entire riser string is improved.

For detection of vortex-induced vibration, the abnormal torque vibration of the electrical tensioner, the riser top vertical vibration from the MRU can be measured and the excessive riser bottom angle would also be a good indication of the presence of resonance.

1.2.2. Providing new functionalities for simplifying the riser operation process:

(1) A motion stabilizer for Drill Stem Test

During the Drill Stem Test (DST), DST tool and the connected pipe or tubing must remain stationary with respect to the well. Since the rig or vessel holding the drill pipe is floating, there is a need to compensate for the motion of the vessel in the load path supporting the drill string.

A novel way to support the drill string such that it is station with respect to the well is to use the marine riser pipe as a support. Since the riser is pinned and does not move with respect to the sea floor, the top of this riser string also does not move with respect to the sea floor. By supporting the weight of the drilling pipe on this riser string, the drill pipe would also be stationary with respect to the sea floor.

Since the drill string is suspended on the riser, other motion compensation systems such as the drawworks active heave compensation system or a compensated coil tube lift frame (CCLF) will not be used during the test. This new system uses a reliable and existing

compensating system that is in continuous duty while drilling, and leaves the drawworks available to manage other activities such as making up pipe or other inventory control matters.

(2) A new riser position control operation mode

During the operation that the rig moves with riser string suspended on the vessel and hang-off in water or the waiting period that the riser is disconnected and hang on the tensioners, it is easy to build up the vertical oscillation, because of the mass spring effect of the heavy riser string excited by the vessel heave motion. If the movement between the riser string and the vessel body is 180° out of phase or this oscillation entering into the resonant condition, we would amplifier this effect to the point of damaging the vessel.

This hybrid riser system is able to provide active heave compensation to control the actual position of the riser string, i.e. to counter the excitation tension by controlling the wire-line tension of the electrical tensioners. Therefore, (1) this functionality strengthens the tolerance to keep mud in riser column by reducing the mass spring effect caused by the heavy mud, which would be an environmental helper. (2) It increases the ability to keep the riser string in water under high sea state. As we know, retracting riser pipes under storm is a very dangerous activity.

During the operation of landing the LMRP onto the BOP (or landing the BOP onto the wellhead), we are able to accurately control the distance between the LMRP and the BOP (or the distance between the BOP and the wellhead) directly by the electrical tensioners. Therefore, (a) we don't need to reconfigure the drawworks for this task, thus enable the drawworks for other important activities; (b) This functionality would allow the LMRP to reconnect back onto the BOP during harsher current condition, therefore reduce the rig down time; (c) Without human hooking up drawworks to riser handling tool using man rider, it would become a safer operation; (d) This would be a time saving method, especially when the rig needs to operate among multiple wellheads.

(3) A vessel motion stabilizer assisting the DP system

Nowadays the DP system helps to use thrusters mitigating excessive pitch and roll motion of the vessel body. Some rigs may vary the hull draft to stabilize the oscillation of the

vessel body. Especially the rigs where the derrick is not located at the center of the vessel body buoyancy gives that unsymmetrical characteristic, and is more vulnerable to this kind of roll and pitch oscillation effect. The cyclic drilling activities with drill pipes moving up and down can easily accelerate the vessel pitch into dangerous situation.

With this hybrid riser tensioning system with the heavy riser string attached on the seabed, we could apply a counter tension on the heavy riser in a small way to counter the wave heave induced force on vessel. This minor variation of the sum of the forces applied on vessel body may be accumulated and alternate the vessel motion from entering into resonant condition. Therefore, we could influence the vessel heave motion by using this hybrid riser tensioning system. If the Dynamic Positioning system helps to mitigate this vessel motion oscillation in the lateral direction, this hybrid tensioning system adds another mitigation element in the vertical direction.

1.3. Dissertation Organization

A structure framework of the integrated hybrid riser tensioning system is proposed and discussed in Chapter 2. An electrical riser tensioner using a direct drive axial flux disc machine is proposed, in order to meet the challenge of the low speed and high torque requirement. An energy storage system would be necessary to compensate the large power fluctuation produced by the electrical riser tensioning system. An ultra-capacitor based energy storage system will be a solution to provide a quick burst of power to refuel the electrical tensioners or to absorb regenerated power from the electrical tensioners. A riser top data logging system is introduced to provide the real time information of the riser status and feedback into the control system, which also serves to the riser recoil detection and riser vortex-induced vibration detection. An overall hardware control framework is proposed in this chapter. And a conceptual software Supervisory-Switched Controller is used to switch among different operation modes.

The realization of the active heave compensation operation mode using this novel hybrid tensioning system is realized in the Chapter 3, also in [13]. A mathematical model for describing this operation mode is built using electrical riser tensioners integrated into hydro-pneumatic tensioning system. One Linear Quadratic Gaussian control and one H_∞ control algorithm are proposed, implemented in Maltab and comapred. The H_∞ control is also implemented into hardware realization. The simulation results and the experimental study have confirmed us that the electrical riser tensioning system is a feasible concept with better safety and stability compared to traditional hydro-pneumatic system. The implementation of the energy storage system into the model demonstrates the overall performance of this integrated hybrid riser tensioner system, and the feasibility of harvesting wave energy. Furthermore, the test also points out that various high precision control algorithms can be implemented without difficulty in the electrical tensioning system, as oppose to the hydro-pneumatic system. The actualization of this principle control mode gives us confidence to carry on for further riser dynamic control.

A novel anti-recoil control strategy by using the riser hybrid tensioning system is proposed in Chapter 4. A more detailed mathematical model is proposed for anti-recoil control purpose. Both process plant model and control plant model are built, which includes a truncated riser string model, a detailed hydro-pneumatic tensioner model and an electrical tensioner model. Linear Quadratic Gaussian control design method is adapted in this control design. The simulation results demonstrate and also confirm our control goals of a more predictable, testable and safer anti-recoil system.

A novel vortex-induced vibration control strategy is proposed in Chapter 5 by using the electrical tensioners. A modal analysis of a typical tensioned Bernoulli-Euler beam governing model and its boundary conditions is carried out in this chapter. The modal analysis provides an easy way to identify the candidate frequencies for lock-in oscillation. A constant gain velocity control using lateral displacement estimation and a constant gain velocity control using vertical displacement feedback are proposed. The simulation demonstrates the effectiveness of this control concept. The controlled dynamic tension delivered in the vertical direction alternates the

natural resonance frequencies and stiffness of the riser string. Hence it avoids the excitation of the oscillation entering into resonant condition, and reduces the amplitude of the vibration in case that the riser is locked into resonant condition.

A concept of the motion stabilizer for drill pipe and tubing use in drill stem test is given in Chapter 6. The detailed control strategy design and experimental study of this control mode would be conducted in the future work.

The Chapter 7 concludes the proposal document, followed by a list of the reference and appendix.

Chapter 2: Framework of the New Riser Hybrid Tensioning System

Comparing to a hydro-pneumatic system, an electrical machine gives the possibility to deliver dynamically variable torque with high accuracy. Nowadays, the development of machine technology and control technology gives us solid technical and practical foundation for the implementation of the electrical riser tensioning control. In this study, we propose a hybrid tensioning system by replacing various pairs of hydro-pneumatic tensioners with the novel electrical tensioning system – forming a layout of hybrid tensioning system. This chapter details the structural framework of the novel hybrid riser tensioning system.

Fig. 2.1 shows a top view layout of the integration of the electrical tensioners into hydro-pneumatic tensioners. Assuming that, initially, the vessel employs four pairs of hydro-pneumatic tensioners, as shown in (a). The two tensioners of each pair stand in the 180° opposite direction. We propose to replace two diagonal pairs by 4 electrical tensioners, denoted as ET1 and ET2. The riser system total required tension is shared among all tensioners. Fig. 2.2 illustrates a 3D physical model of the hybrid tensioning system. And the bigger scale 3D views of this hybrid tensioning system are shown in Appendix A.

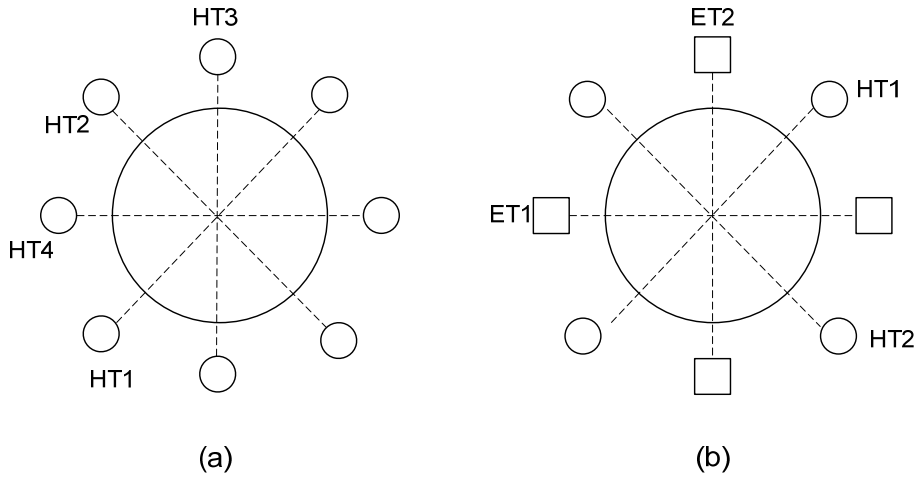

Fig. 2.1 Top-view Layout of the Electrical and Hydro-pneumatic Tensioners

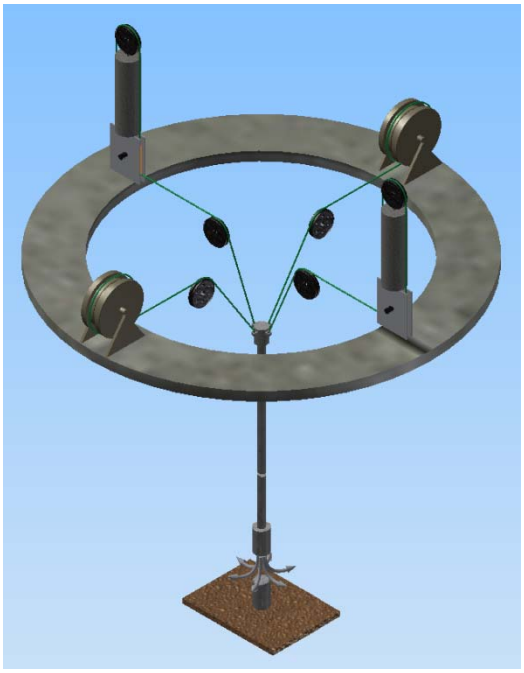

Fig. 2.2 3D Model of the New Hybrid Tensioning System

2.1. Electrical Tensioner

For the electrical tensioner, the main component is a motor that also acts as a generator (M/G). During the first half cycle of the vessel moving up, the M/G functions as a motor mechanically driven by a corresponding motion of paying out rope; and during the next half cycle of the vessel moving down, the M/G functions as a generator mechanically driven by a corresponding motion of paying in rope.

2.1.1. The Axial Flux Permanent Magnet Machine

This tensioning system is a typical high torque/low speed application. Depending on the diameter of the rotor and other mechanical couplings, the nominal torque of the M/G could be in the range of $14\ kNm$, while the speed is in the range of $0.2\ Hz$ [1]. As shown in Fig. 2.3, an electrical winch with mechanical gearbox is a suitable fit for this application. However, the main disadvantage of this electrical winch system is its big moment of inertia, caused by several stages of heavy rotating masses. During every day active heave compensation operation, the M/Gs and

their auxiliary mechanical parts are exposed to constant acceleration and deceleration. According to the second Newton's law, this significant moment of inertia requires additional power capacity of the M/G to accommodate this extended torque demand. And eventually, we have to over-size the M/G. Moreover, the constant heave motion exposes the gearbox in a high "ton-mile" environment, which requires high maintenance and may bring tensioners out of service more frequently. Therefore, an electrical tensioner with direct-drive M/G might be a better solution for this active heave compensation application.

A permanent magnet machine provides the advantage of compact size and better efficiency. Comparing to a same physical size induction machine, a permanent magnet machine may deliver 30% more usable torque due to its small heat loss and high power density [15]. Furthermore, an axial flux disc type permanent magnet machine (AFPM), which gives the suitable shape structure for wire-line direct drive, will be a better fit in this application.

Fig. 2.3 Motor Driven Electrical Winch System with Gearbox

Regarding the high power requirement, an AFPM could be designed to have a higher power-to-weight ratio resulting less core material and higher efficiency. The speed of the AFPM is driven by the vessel heave motion and the torque is directly applied on the wire-line. This simple mechanical arrangement gains more robustness comparing to gearbox transmission. And smaller moment of inertia can be obtained by the rope directly driving on the disc machine body.

Secondly, many topologies of the main air gap flux can be derived and the direction of the main air-gap flux can be varied, which provides good flexibility for machine power configuration. Finally, according to high torque/low speed requirement, multi-stator-multi-rotor form axial flux machine may be constructed, as shown in Fig. 2.4. The total delivered torque could be doubled or tripled by adding more stator and rotor discs [16].

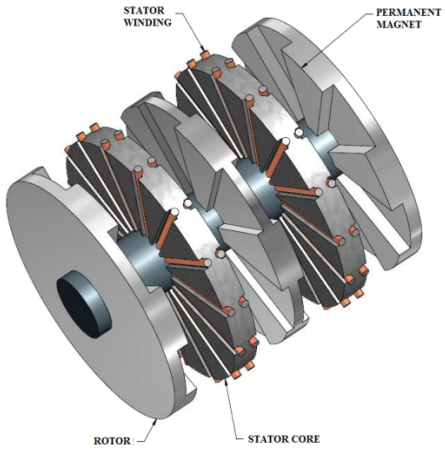

Fig. 2.4 Multi-Stator-Multi-Rotor Axial Flux Permanent Magnet Machine

Moreover, the AFPM forms a thin disc structure with bigger effective torque portions. For radial type machine, only the windings facing the rotor PMs are used for torque production, the portions of the windings on the outside surface of the stator and the portions on both sides are considered to be end windings in this topology, as shown in Fig. 2.5(b). However, in AFPM, effective portion for electromagnetic torque production is over a continuum of radii on the disc surface, not only at a constant radius, as shown in Fig. 2.5(a). The torque-per-unit-volume of AFPM is significantly improved from the radial machine [17][102]. A 2-D finite element method helps to integrate the magnetic flux along the air-gap surface.

The control technology for the AFPM should be the same as that for the conventional radial type machine.

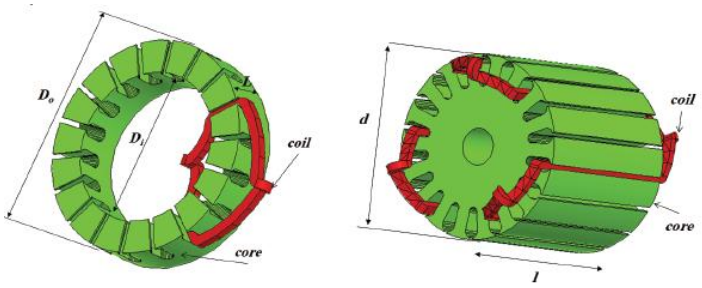

Fig. 2.5 Stator Winding Configurations (a) Axial Flux Machine, (b) Radial Flux Machine

2.1.2. Hardware Topology of the Electrical Tensioner

Fig. 2.6 shows the hardware topology of this AFPM machine. An inverter type Variable Frequency Drive (VFD) with IGBTs is in need for each AFPM, which should be able to manage power flow in both directions. The PWM IGBT firing pulses would be generated and sent from the VFD control circuit via fiber optic signals. And the system input voltage references are calculated and sent from the upper level tension controller [18]. A position sensor with high resolution is necessary for monitoring the wire-line displacement and calculating the drive control references. A resolver may be used here as they are robust and can be used in harsh environments. An integrated and analogue circuitry is necessary to interface the resolver with the digital controller. AFPM electrical measurements are also feedback to the upper level tension controller via an analogue measurement interface.

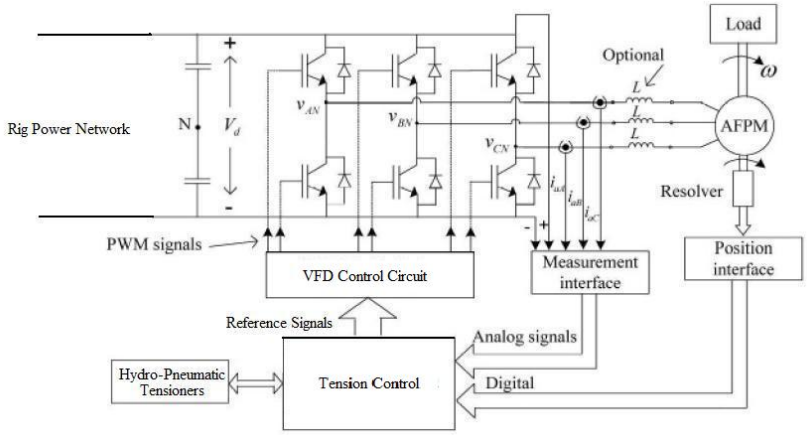

Fig. 2.6 Hardware Topology of the Electrical Tensioner Control System

2.2. Energy Storage System

As mentioned in the previous sections, the active heave compensation control mode using the electrical tensioning system is a high power cyclic operation by nature. In the first half cycle of wave motion, the energy absorbed by all electrical tensioners from the rig power network could be in the range of MJ, and the peak power required could be as high as MW [23]. Then in the next half cycle, the same amount of energy is released into the power network. First of all, this high power cyclic operation demands additional generator capacity to accommodate the maximum power consumption, and causes a disproportionately large amount of diesel consumption. Secondly, this high power fluctuation may badly affect the rig power network stability. The use of energy storage elements may help to mitigate these problems by making the whole hybrid tensioning system a low power cyclic operation. According to experimental studies, the energy storage system will help to reduce up to 20% of diesel consumption, and also avoid the instability effect to the rig power network.

Different types of energy storage device can be used in this application, such as flywheels, batteries, ultra-capacitors or the combination. However, the flywheel, as a kinetic energy storage device, has high friction loss, high maintenance cost and big volume comparing to batteries or ultra-capacitors with the same energy capacity [21]. According to the study [19], the ultra-capacitor has about 1 million cycles of lifetime if we bring down the voltage to 44% every cycle, which means extract about 80% of the energy. This is an exceptional longer life than batteries with the same energy capacity. Furthermore, as we know, ultra-capacitors are high power density device, currently around $0.5 - 2\ kW/kg$, in comparison to batteries. And it is also high energy density device, around $5 - 6kWh/kg$ in comparison to other types of capacitor. Hence, we choose ultra-capacitors which are the most suitable energy storage device for AHC application.

Fig. 2.7 Example of Ultra-Capacitor Banks for Energy Storage System

However, in condition of the constant heave motion that repeated every 8-12 seconds, the ultra-capacitor's life of charging and discharging cycle is still facing a big challenge. If we size the ultra-capacitor bank (UCB) to discharge 80% of the total capacity during each heave period, their life may only last for 140 days. In order to tolerate heavy duty cycle and high RMS current, the total capacity of the UCB has to be de-rated in order to achieve a longer lifespan [20]. It is proposed that, in order to achieve maximum life, the UCB's total Farad capacity should be large enough to satisfy both:

(1) 1.2 times of the maximum vessel heave for the most significant sea state criterion;

(2) 5 times of the regular sea state heave, while discharging to the lowest 20% of the total capacity.

Fig. 2.8 shows the hardware topology of this energy storage system. The ultra-capacitor modules could be divided into several banks. A DC/DC power converter (also called chopper) with power semiconductors controls the power flow into and out of each bank. The main difference between ultra-capacitor control and battery control is that ultra-capacitors' voltage varies significantly in relation to its state of charge (SOC), while the battery voltage stays almost constant until depletion. In this case, a half bridge buck-boost converter will manage the energy

transfer in both directions, while the voltage keeps uni-directional. An upper level coordination UCB controller could be used to monitor the health of the UCB strings, and distribute the power demand among them according to their charging level. This UCB controller communicates with the tension controller, so that the power demand from the electrical tensioners is transferred to the energy storage system as a reference.

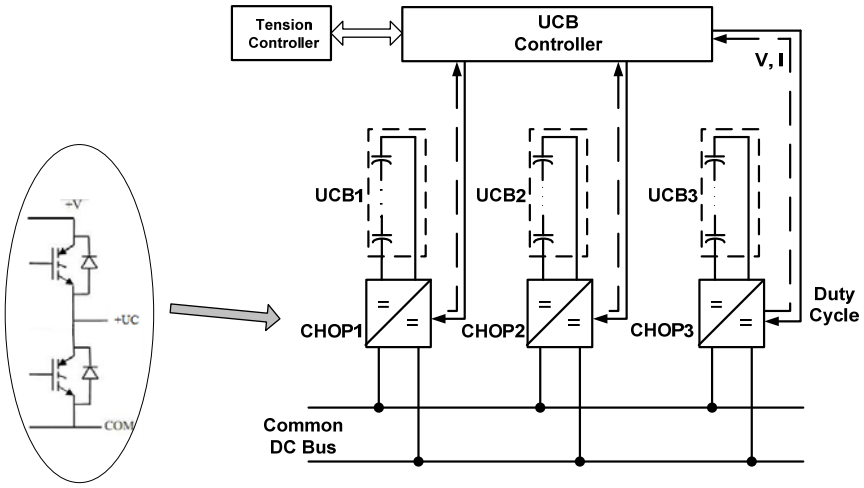

Fig. 2.8 Hardware Topology of the Energy Storage System

As described in Fig. 2.9, a power management controller is necessary in this topology to keep energy equalized in each UCB, in order to avoid the over-depletion on a certain UCB, so that the life cycles of all UCBs are balanced. A power management algorithm should be developed [22]. When the energy surge is regenerated from the electrical tensioners, the amount of power flowed into the energy storage system should be distributed to each UCB according the percentage of its free volume versus the total free volume of all UCBs, as shown in equation (2.1):

$$P_i = \frac{C_i\left(V_{i\_FULL}^2 - V_i^2\right)}{C_1\left(V_{1\_FULL}^2 - V_1^2\right) + \cdots + C_i\left(V_{i\_FULL}^2 - V_i^2\right) + \cdots + C_m\left(V_{m\_FULL}^2 - V_m^2\right)} P_{TOTAL} \tag{2.1}$$

where P_i with $i = 1, \ldots, m$, is the power distributed to the i^{th} UCB, P_{TOTAL} is the total power regenerated from the tensioning system, C_i is the capacitance of the i^{th} UCB, V_i and V_{i_FULL} are the actual voltage and the nominal voltage of the i^{th} UCB. And when the energy is consumed by electrical tensioners, the amount of the power transferred out of the energy storage system should be withdrawn from each UCB according to the percentage of its state of charge (SOC) versus the total SOC of all UCBs, as shown in equation (2.2):

$$P_i = \frac{C_i V_i^2}{C_1 V_1^2 + \cdots + C_i V_i^2 + \cdots + C_m V_m^2} P_{TOTAL} \tag{2.2}$$

A feedback controller with faster sampling rate would be used to regulate the power, voltage and current inside of each UCB based on the KW reference received from the power management controller. An outer power control loop predefines the UCB voltage set point. Then the difference between this reference voltage and the measured UCB voltage is fed through a voltage regulator which sets the UCB current reference. Finally, the chopper duty cycle may be generated by the current regulator based on the error between the current reference and the measured values.

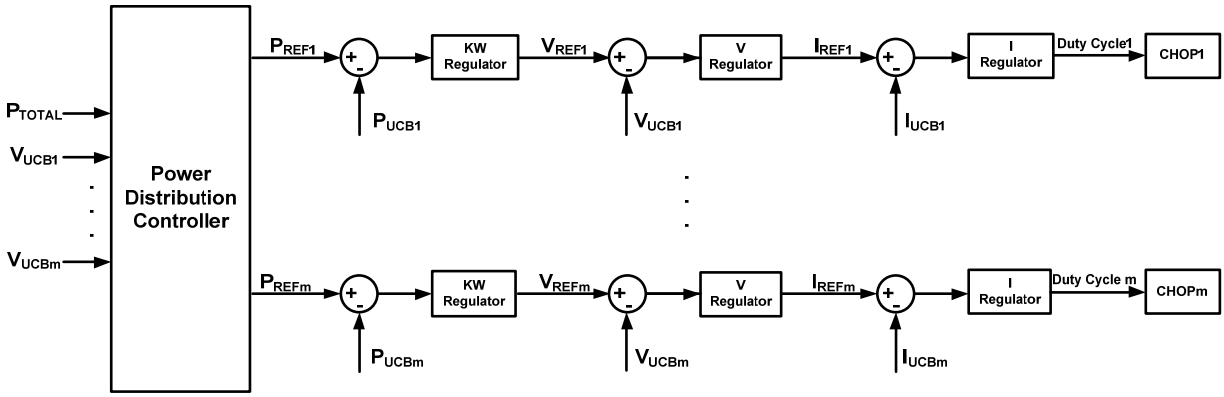

Fig. 2.9 Control Scheme of the Energy Storage System

In condition that each UCB contains a large number of cells, then a switching network can be used to switch the capacitors in series and/or in parallel. While charging capacitors, more capacitors can be put in parallel, so that the string voltage is lower for shorter converter duty

cycle and lower loss. While discharging, more capacitors can be put in series for the same reason [24].

2.3. Power Dissipater

As far as safe operation is concerned, several electrical power dissipaters, such as resistors or any power consumption devices, should be connected on the same DC bus. In the scenario that the energy storage system is fully charged and the rig power network is very lightly loaded, not able to absorb large regenerated power from the electrical tensioners, a safe operation algorithm should route the regenerated energy into these dissipaters. A uni-directional chopper may regulate the amount of energy dissipating in each resistor.

Fig. 2.10 Example of Water Cooled Power Resistor for Power Dissipation

2.4. Integrated Hybrid Riser Tensioning System

2.4.1. Novel Electrical Tensioning System

Fig. 2.11 represents the framework of the novel electrical tensioning system. The main components consist of multiple electrical tensioners, one energy storage system, several power

dissipaters and one Active Front End rectifier (AFE). All these components are connected on a common DC bus.

The rig power is usually produced by five to eight diesel engine-generator sets with approximately 50 MW capacity in total. The main problem with diesel generators is their high inertia. With rapidly varying load demand, the diesel gen-set may not be able to deliver the required power demand profile. Plus it consumes more kilogram of fuel to deliver the same amount of energy, in comparison with that of steady state or slowly varying load. The AFE, a controlled IGBT rectifier with bi-directional power capability, is introduced here as a part of the electrical tensioning system. It is used not only as a rectifier interfacing between AC and DC, but also as a regulator that controls the DC bus voltage by moving power flow from the DC bus to the AC rig power grid or reversely from the AC power grid to the DC bus.

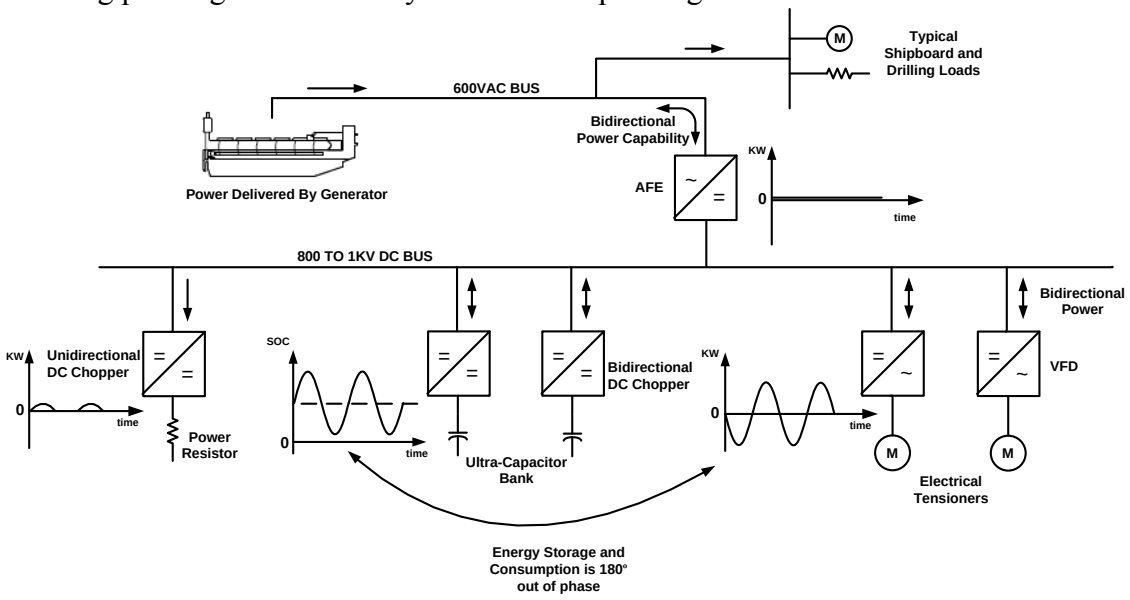

Fig. 2.11 One-Line Framework of the Electrical Tensioning System

2.4.2. Power Management Control Strategy

The coordination among various power sources of the electrical tensioning system requires a higher level power management control. A real time power distribution control

strategy is in need for energy routing among different power sources: the electrical tensioner, the energy storage system, the AFE, and the power dissipater. The energy routing topology is shown in Fig. 2.12.

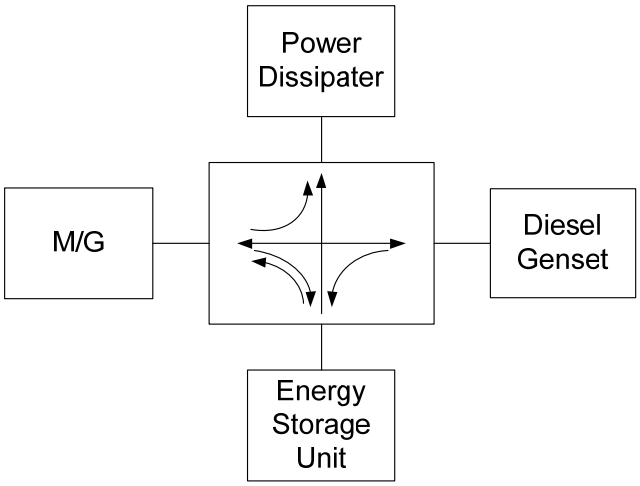

Fig. 2.12 Energy Routing Topology

The DC bus voltage and AC bus frequency, as a good indication of the system power demand, could be used as a coordinate for load sharing. We could pre-configure the energy routing topology in the overall power management system before the real-time operation. Three alarms could be set:

(1) DC bus voltage above $1000V$ indicates all UCBs are fully charged;

(2) DC bus voltage below $800V$ indicates all UCBs are depleted, only less than 20% of the total capacity is left for protection;

(3) AC bus frequency above $60.5Hz$ indicates the rig power grid is too lightly loaded and cannot absorb any regenerated energy.

As illustrated in Fig. 2.13(b), when the DC bus voltage varies between $820V$ and $980V$, the AFE should stay inactive. Meanwhile, the energy storage system should take the full load, as shown in Fig. 2.13(a). The power flow into and out of the energy storage system could be simply designed as a linear relationship (or a PID controller) with the DC bus voltage, which is

an effective index of system power demand. When the DC bus voltage increases above $1000V$, the energy storage system is fully charged, the AFE becomes active, and the remaining regenerated power will be routed back into the rig power grid. If the power grid frequency on the AC side of the AFE increases above $60.5Hz$, this indicates that the grid is under-load, the diesel engine is in an unstable condition, the power dissipater becomes active and burns the remaining regenerated energy into heat for safety operation. When the DC bus voltage decreases below $800V$, the UCBs are depleted less than 20% of its total SOC, the AFE is activated, and the additional power has to be obtained from the rig power grid.

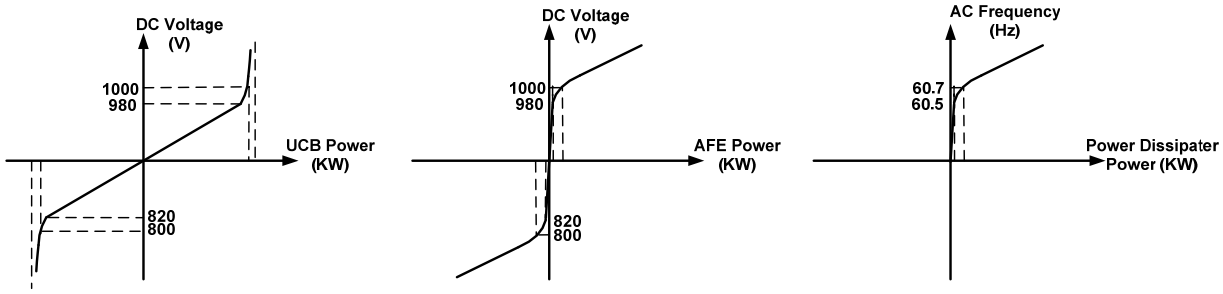

Fig. 2.13 Load Sharing Profile (a) the Energy Storage System (b) the AFE (c) the Power Dissipater

Theoretically, as long as we assume the losses and auxiliary service are negligible, this electrical tensioning system is an independent energy conversion system with almost no energy consumption from the rig power grid. However, in fact, various losses could be involved in this electrical tensioning system, such as the mechanical frictions, motor heat loss, UCB leaking, IGBT conducting loss, etc. Plus the auxiliary services, such as cooling blower motors, low voltage control power, are all pre-requisite for supporting the normal functionality of main power components. Hence, in long term probability point of view, the energy stored in UCBs will be depleted eventually. In order to maintain the independence of this electrical tensioning system, we propose to harvest wave energy by means of applying variable tensions. Fig. 2.14 shows that, during the half period of vessel rising up, we may apply the minimum allowable tension on

the wire-lines, so that less energy is converted to potential energy, and during the half period of vessel falling down, we change the wire-line tensions to the maximum allowable value, so that more electrical energy is harvested from the wave motion. By applying this method during normal active heave compensation operation, we may be able to not only harvest enough energy to counter all losses, but also feed back to the rig power grid in a constant manner by using UCBs as the power buffer.

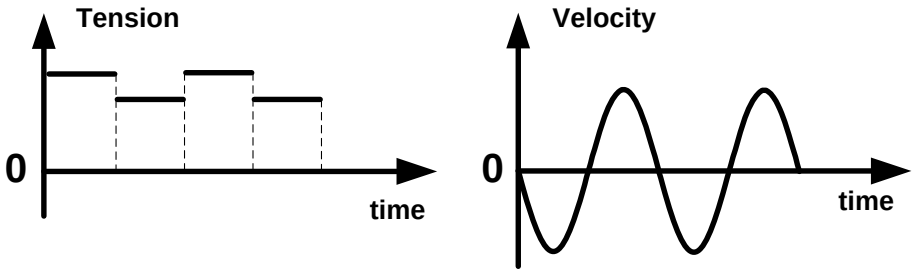

Fig. 2.14 Tension Applied on Wire-line vs. the Vessel Position for Harvesting Wave Energy

One of questions that the application engineers most concerns about is what will the electrical riser tensioning system behave in case of rig power blackout? First of all, despite all the disadvantages described in Chapter 1, hydro-pneumatic tensioners are passive and self-contained system which has no power exchange with external systems. It has good resistibility to disturbances or fluctuations. It is a mature and commercial available product with low risk. So we still need hydro-pneumatic tensioners to further ensure the safety and the stability of the whole riser system. Secondly, the energy storage system is in fact a large, high quality Uninterruptible Power Source (UPS). In condition of grid power outage, the energy that stored in UCBs and the energy recycled from the tensioners should sustain the normal operation until the power outage ride-through. The only energy consumption in this tensioning system would be through losses and auxiliary service. Thirdly, if we could manipulate the wire-line tension as described in Fig. 2.14 and harvest wave energy, the regenerated energy may not only satisfy the

tensioning system itself, but also send back into the rig power grid for emergency use, such as blackout restoration.

2.4.3. Integrated Hybrid Riser Tensioning System

Fig. 2.15 depicts the proposed architecture of the coordination control strategy among the entire hydro-pneumatic riser tensioning system and the electrical tensioning system. Two main controllers could be used for the entire hybrid riser tensioning system control: an intelligent controller for overall tension control and an intelligent controller for power management.

First of all, the tension controller is responsible to regulate the wire-line tensions of all the electrical and hydro-pneumatic tensioners. All the control modes would be embedded in this controller and switch over each other according to the supervisory control. This overall tension controller sends the commands and the reference signals to all the VFDs of electrical tensioners and to the hydro-pneumatic tensioner controller, and receives the status feedback of all the tensioners, as shown in Fig. 2.15 by signal arrows. It is worthwhile to mention that for simplification, the tensioners, as drawn in Fig. 2.15, are paired between one electrical tensioner and one hydro-pneumatic tensioner. However, as a matter of fact, both electrical tensioners and hydro-pneumatic tensioners have to be pairs with their own type, as shown in Fig. 2.2. Moreover, the system arrangement has to be symmetrical. If one of the tensioners failed, the opposite one has to be set free. The remaining $(N-1)$ pairs of tensioners must carry the entire load.

Secondly, the controller of power management communicates among the overall tension controller, the AFE controller, the UCB controller, the Power Resistor (PR) controller. It closely monitors the DC bus voltage and the AC bus frequency through a voltage sensing device. As described in the previous section 2.4.2, the power management strategy would be implemented in this controller.

Auxiliary services are necessary for ensuring the normal functionality of the whole system. The AFPM cooling system, such as air-forced blowers or water cooling circulation, is necessary to optimize the AFPM size and efficiency. The Motor Control Centers (MCC), that provide basic control to the blower motors, are supplied by either AC power from the grid (close CONTACT1) or wave energy from the electrical tensioning system (close CONTACT2). The blower air pressures and the AFPM temperatures are monitored individually in VFD controller. The Emergency Stop is hardwired to all main power devices for direct shutdown. Meanwhile, the disc brakes are placed on all AFPMs, the electrical tensioners are hang-off and withdraw from service.

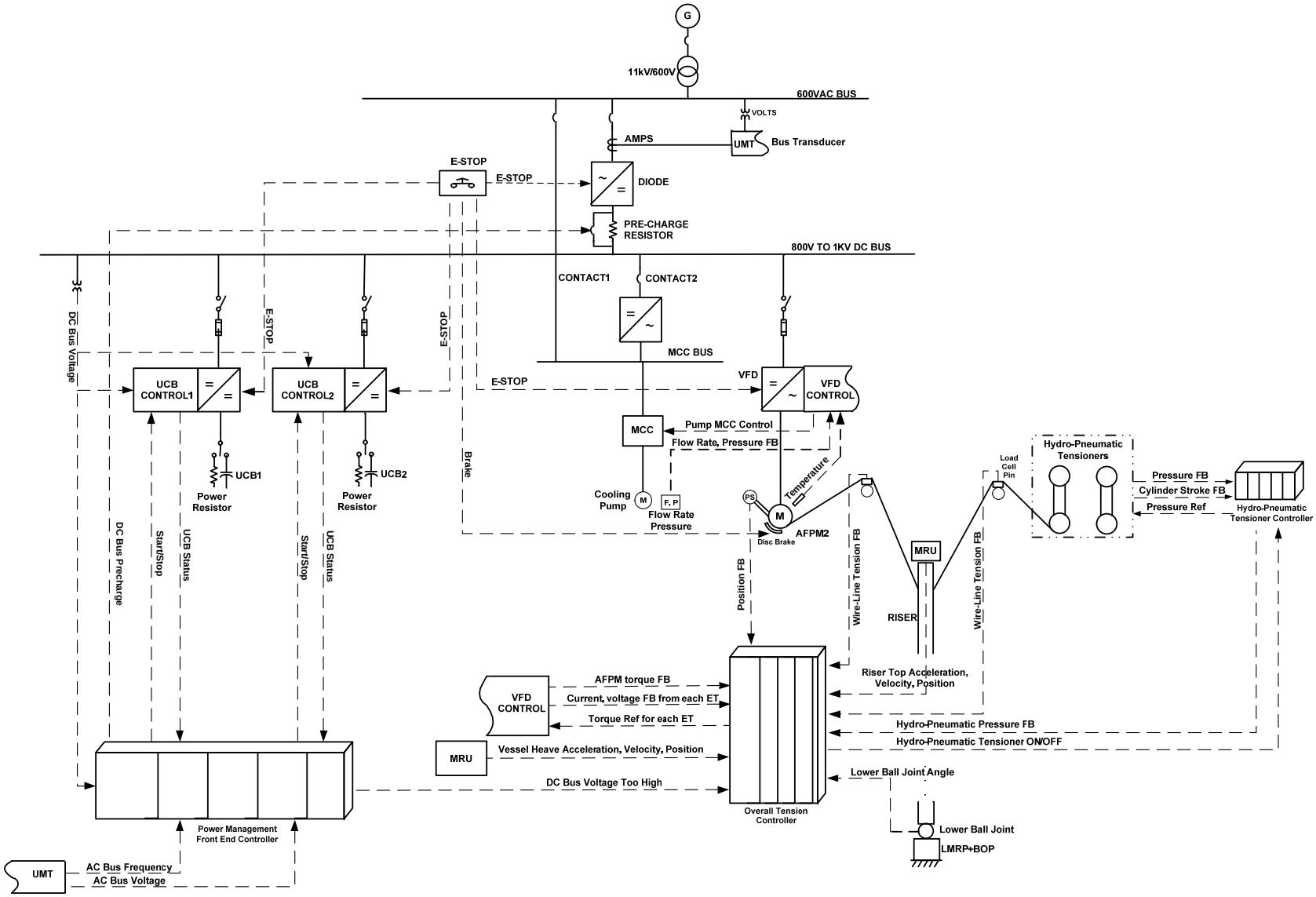

Fig. 2.15 Coordination Control Architecture of the Hybrid Riser Tensioning System

The tensions delivered by the hydro-pneumatic tensioners F_{HT} are measured and feedback to the controller. The total tension reference for the whole riser system F_{ref} is calculated by the closed loop control laws. The actual tension command provided to each electrical tensioner is a time variable values satisfying:

$$F_{ref\_ETi}(t) = \left(F_{ref}(t) - \sum_{j=1}^{n_{HT}} F_{HTj}(t) \right) / n_{ET} \tag{2.3}$$

where F_{ref_ETi} denotes a tension reference signal delivered by the controller to each electrical tensioner., while F_{HTj} is the tension delivered by the hydro-pneumatic tensioner j at any given time. The n_{HT} and n_{ET} are the total number of hydro-pneumatic and electrical tensioners.

2.4.4. Future Work - Supervisory-Switched Controller

2.4.4.1. Introduction of Switching Control

As environmental condition varies, the plant controller should also change. This motivates the supervisory control which has the ability to automatically switch among different operation modes depending on the situation [27][38].

The switching control consists of two main parts: the supervisor and the bank of controllers, as shown in Fig. 2.16. The supervisor compares the preset criterions to the actual riser behavior, and decides which model and controller are best to control the ongoing process.

The bank of models is given by

$$\mathcal{M} := \bigcup_{p \in \mathcal{P}} \mathcal{M}_p \tag{2.4}$$

There will be at least one controller designed for each operation mode. The set of controllers is denoted as

$$\mathcal{C} \coloneqq \bigcup_{q \in \mathcal{Q}} \mathcal{C}_q \tag{2.5}$$

where $\mathcal{P}$ and $\mathcal{Q}$ are the set of models and controllers, p and q denote the p^{th} model and q^{th} controller respectively. When the switching is made, an index signal σ in the feedback loop determines the selected controller. The supervisor's main task is monitoring of the feedback signals from the data logging system, deciding which control action to perform and trigging the correct controller.

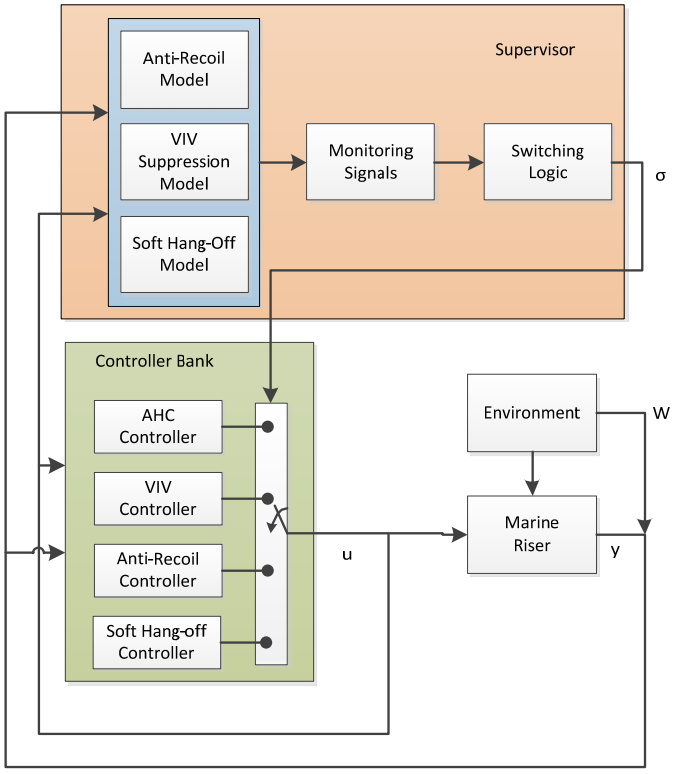

Fig. 2.16 Structure of Switching Control Concept

2.4.4.2. Switching Logic

The index σ of the controller in the feedback loop is determined by the switching logic shown below in Fig. 2.17. In order to provide smooth transition between controllers, some

weighting factors can be introduced. And some hysteresis factors can be included in the switching logic to prevent chatting effect.

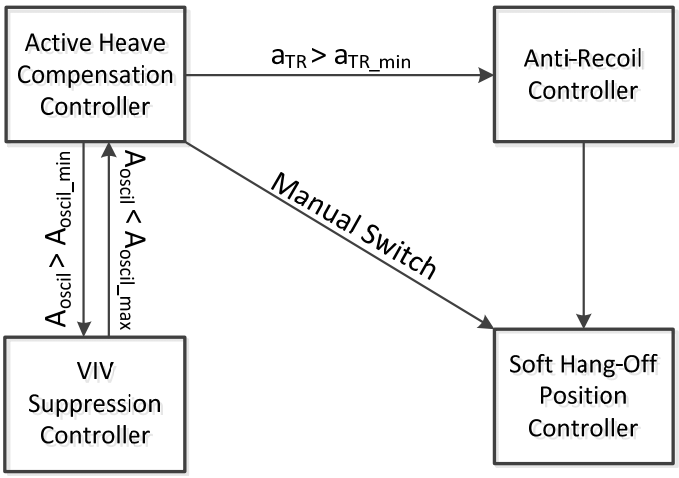

Fig. 2.17 The Switching Logic for Supervisory Control

2.5. Data Logging System for the Riser Controller

As introduced in previous sections, a new riser data logging system will be installed to provide real time information of the riser system, instead of relying on sensors installed on tensioners.

A Motion Reference Units (MRUs) is usually a solid state (MEMS type) motion reference device. It usually has three accelerometers, capable of measuring surge, sway and heave, and also has three rotation rate sensors for pitch, roll, and yaw, to a high degree of accuracy.

The vessel that is considered as a rigid body has 6 degrees of freedom, which are measured with several MRUs distributed evenly at different locations. The heave measurements installed on vessel at different locations will give different heave values, as well as the vessel pitches and rolls with the wave. Thus the accurate heave position of the vessel $h(t)$ should be calculated by the average value of all the available MRU signals.

Fig. 2.18 The Telescopic Joint at the Top of the Riser

A small Inertial Navigation System should be built to monitor the riser top displacement x_{TR} by installing a MRU on the riser top, as shown in Fig. 2.18. A small electronic control board can be installed in the MRU. In order to minimize the errors like sensor noise, bias, and misalignment of the accelerometers, and ensure a stable integration, it is necessary to design a Kalman filter for signal conditioning in the future [33]. The position, velocity and acceleration signals from the two MRUs, placed on top of the riser and on the vessel body respectively, are critical here for the entire riser control algorithm.

The new riser recoil detection system now becomes independent of the wire line fleet angle and any motion of the vessel. By monitoring the acceleration of the riser top, the detection will become much more reliable and faster, potentially detecting the condition within 1 second. If the acceleration exceeds a certain limit, the electrical tensioners are able to reduce the wire-line tension instantaneously, providing a much more effective anti-recoil control. The VIV can also be detected by monitoring the displacement velocity signal. The amplitude and the frequency of the riser high speed vibration can be calculated based on the riser model built in Chapter 5.

The tensions applied on the wire-lines F_{L_ET} and F_{L_HT} should be measured as primary feedback signals, which control the tension compensation between the hydro-pneumatic and electrical tensioners. A strain-gauge type load cell can be placed underneath the tensioner sheaves, or can be connected in line with the wire-lines. Moreover, by monitoring the tension, we are able to observe the VIV oscillation pattern, thus can serve as a backup VIV detection method, in addition to the velocity of the riser top.

The upper and lower riser angle signals θ_{TOP} and θ_{BOTTOM} can be sent to the riser control system as well. The riser angle signals are available now for the riser management system, as a part of the Dynamic Positioning control [28]. It is used to assist the optimization of the vessel position with respect to the well head, and to prevent vessel drift off. This signal can be imported to the riser top data logging system, so it provides valuable information to estimate the shape and the location of the riser under water.

The velocities of the electrical tensioners are necessary feedback signals for the motor control strategy. They also provide critical information for monitoring the wire-line slack incident.

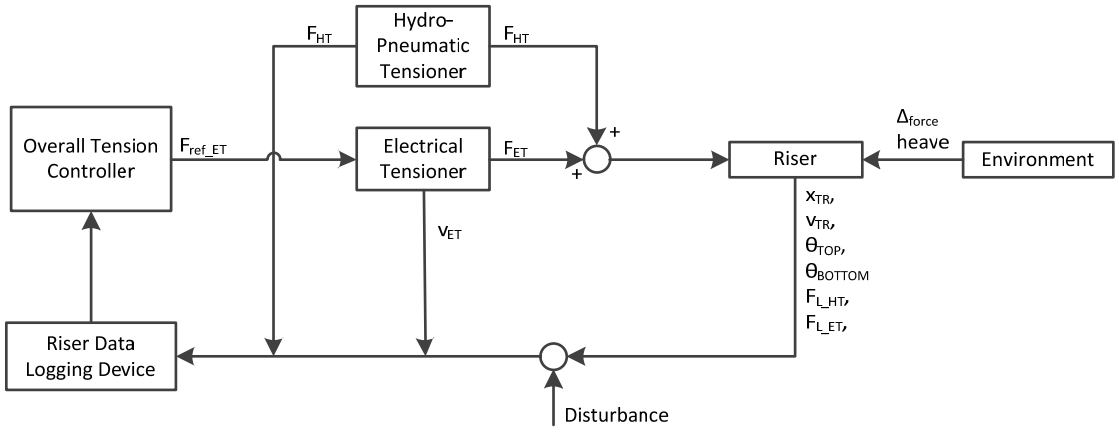

Fig. 2.19 A Block Diagram of the Load Sharing Strategy

Chapter 3: Modeling and Control Design of the AHC Control Mode[1]

3.1. Previous Work

Based on linear and nonlinear control theories, a number of active heave compensation techniques for deep water marine applications have been proposed in the literature. Refer to, for example, K.D. Do and J. Pan [29] and [30], who proposed a nonlinear controller for the active heave compensation system, by adding an additional electric controlled hydraulic double rod actuator on the crown block compensator at the derrick top. Nevertheless, only one set of this controlled actuator is installed per rig providing rough heave compensation for the drilling string. B. Leira and M. Blanke [31] discussed a nonlinear back-stepping controller by reducing top and bottom angels through vertical control of active heave compensator. This controller is aimed to the riser tensioners, however is also driven by a hydraulic double rod actuator. These control designs are proven to be effective; however their operation still suffers from the slow response by the nature of hydro-pneumatic system and the maintenance and potential leakage problems.

More literature related to active heave compensation using electrical machines is found in connection with crane lifting and module handling systems. S. Kuchler et el [33] designed a feed-forward controller to compensate the vertical motion disturbance using the predicted motion for the crane system in harsh sea condition. The crane payload moves at the assigned reference velocity decoupled from the wave-induced vessel motion. L. Li and S. Liu [34] described an optimal controller based on the dynamic vibration absorber concept for deep-sea mining lift pipes. Umesh Korde [35] proposed a general active heave compensation controller for the case of the drilling string engaged in the borehole. These papers are mainly focused on the physical analysis of heave compensation control solution, but do not consider the application control by means of the riser top tensioner. Recently, an investigation about riser top tension control was

[1] Yin Wu, "Enhanced Active Heave Compensation Control Design for New Riser Hybrid Tensioning System in Deepwater Drilling", OMAE 2015- 41675.

made in [38] where the purpose was to avoid collision between two risers for production platforms. In this paper several PI controls were applied to maintain the effective length of the risers by adjusting the top tension.

A set-point chasing controller with respect to the vertical riser top end position is proposed below for controlling the dynamic riser top tension of the novel hybrid riser tensioning system. This chapter focuses on the vertical wire-line displacement control during active heave compensation operation mode and the horizontal offset is assumed to be controlled by the dynamic positioning system.

3.2. Mathematical Modeling of the Hybrid Riser Tensioning System for AHC Control

3.2.1. Electrical Tensioner Model

The concept of the electrical riser tensioner is shown in Fig. 3.1. An electric winch driven by a permanent magnet synchronous motor drive (PMSM) is considered to be the main component of the electrical tensioner. From control design perspective, the control technology for the radial type PMSM is the same for the axial type motor. In this chapter, we use radial type PMSM which is more accessible as the example, to design the active heave compensation control.

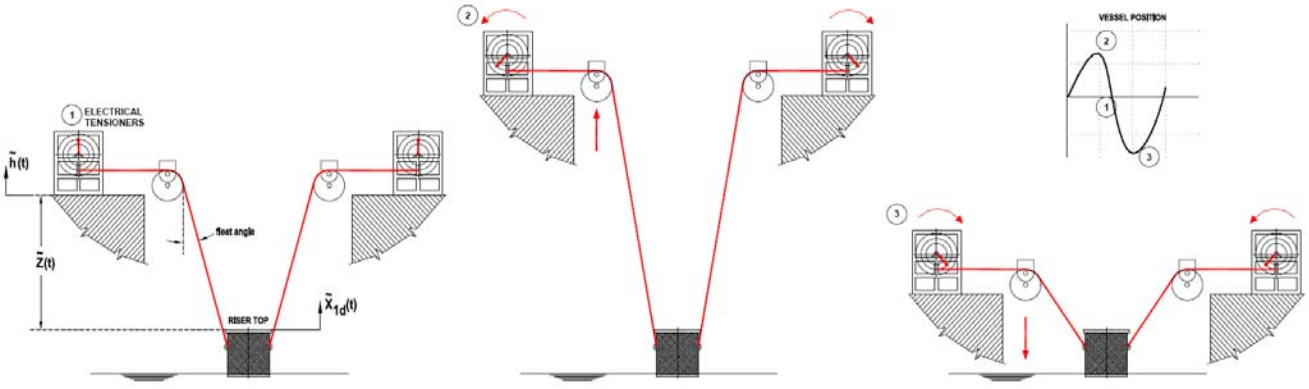

Fig. 3.1 Heave Compensation by Electrical Tensioners with Heave Motion

A direct drive PMSM without gearbox is modelled here. Fig. 3.1 shows that the wire-lines of the winch roll out following the vessel heave, when the vessel rises up; and the wire-lines roll in, when the vessel falls down.

The system model of a PMSM can be described in the rotor rotating reference frame as follows [36], [37]:

$$\begin{cases} v_q = R_E i_q + \dot{\lambda}_q + \omega_s \lambda_d \\ v_d = R_E i_d + \dot{\lambda}_d - \omega_s \lambda_q \end{cases} \tag{3.1}$$

With

$$\lambda_q = L_q i_q \tag{3.2}$$

$$\lambda_d = L_d i_d + L_{md} I_{fd} \tag{3.3}$$

$$\omega_s = P \omega_r \tag{3.4}$$

where v_d and v_q are the d, q axis stator voltages, i_d and i_q are the d, q axis stator current, L_d and L_q are the d, q axis stator inductance, R_E is the stator resistance, ω_s is the motor electrical frequency, ω_r is the rotor speed, I_{fd} is the equivalent d-axis magnetizing current, L_{md} is the d-axis mutual inductance, P is the number of pole pairs.

The electric torque can be expressed as

$$T_{ET} = 3P\left[L_{md} I_{fd} i_q + \left(L_d - L_q\right) i_d i_q\right]/2 \tag{3.5}$$

and the equation of the motor dynamics is:

$$J_r \dot{\omega}_r = T_{ET} - T_{L\_ET} - b\omega_r \tag{3.6}$$

In equation (3.6), T_{L_ET} stands for the load torque, b represents the damping coefficient and J_r is the moment of inertia of the rotor.

Considering the field-oriented control for PMSM, the rotor current vector is oriented perpendicular to the stator magnetic field, by this means the control scheme is to make $i_d = 0$.

In equation (3.2) and (3.3), since L_{md} and I_{fd} are constant for a PMSM; the electromagnetic torque T_{ET} is then proportional to i_q; which is determined by closed loop control. The rotor flux is produced in the d-axis only, while the current vector is generated in the q-axis for the field-oriented control. Since the generated torque is linearly proportional to the q-axis current as the d-axis rotor flux is constant in equation (3.5), the maximum torque per ampere can be achieved.

The electrical tensioner system model can be rewritten as:

$$\begin{cases} \ddot{x}_L = \dfrac{{r_{winch}}^2}{J_{eff}}\left(\dfrac{3PL_{md}I_{fd}}{2r_{winch}}\, i_q - B_E\dot{x}_L - \dfrac{F_{L\_ET}}{cos\theta}\right) \\ \dot{i_q} = \dfrac{1}{L_q}\left(v_q - R_E i_q - \dfrac{L_{md}I_{fd}P}{r_{winch}}\,\dot{x}_{ET}\right) \end{cases} \tag{3.7}$$

where x_L represents the wire-line displacement of the tensioner, r_{winch} is the radius of the electric winch J_{eff} indicates the effective moment of inertia including the inertia of the motor, winch and sheaves. $B_E = b/r_{winch}^2$. The active control input into this electrical system is the quadratic axis stator voltage v_q.

3.2.2. Hydro-pneumatic Tensioner Model

The hydro-pneumatic tensioner consists of pneumatic, hydraulic as well as mechanical components. In order to simplify the system model, some assumptions are presented as follow:

(1) The oil density is high and not compressible comparing to the air;

(2) The heave motion is slow enough to neglect the hydraulic part of the system;

(3) The pressure in the low pressure chamber of the hydraulic cylinder is negligible comparing to that of the high pressure cylinder chamber;

(4) All the pressure drops across all the pipes and valves are summed together and modeled as a constant parameter R_H;

(5) The active heave compensation operation does not require extensively fast response of the tensioners, so that we assume that the temperature remains constant;

According to the ideal gas law, we have:

$$p_H V_H = nRT \tag{3.8}$$

where p_H represents the actual pressure in the high pressure cylinder chamber and V_H represents the total volume of the high pressure gas in the accumulator and the APVs. n here is the chemical amount in moles of the contained gas. R is the gas constant. T represents the gas temperature in Kelvin.

The pressure gradient of the piston is given by the following expression:

$$\dot{p}_H = \frac{1}{V_H}(\dot{m}_g RT - p_H \dot{V}_H - R_H p_H) \tag{3.9}$$

where $V_H = V_{av} + V_{accu\_midstroke} - A_H x_L$, R_H is the equivalent flow resistance. $\dot{m}_g$ is the mass flow rate of gas entering into the APVs with $m_g = n \times 28.97 g/mol$. The control input into this hydro-pneumatic system is $\dot{m}_g$, which is very slow.

The mechanical state variables x_L, $\dot{x}_L$ are to be found by means of a second Newton's law applied for piston equilibrium, as shown in Fig. 3.2:

$$p_H A_H = m_{eff}\ddot{x}_L + B_H \dot{x}_L + m_{eff} g + F_f + F_{L\_HT} \tag{3.10}$$

where the x_L hydro-pneumatic system indicates the cylinder piston displacement from the mid-stroke, $\dot{x}_L$ is the piston velocity, the A_H is the cylinder piston area, m_{eff} is the mass of the piston including mass of the sheaves, bearings, shaft and a bracket. F_{L_HT} is the load force, F_f is the friction force. B_H represents the viscous coefficient.

The hydro-pneumatic tensioning system can be rewritten as:

$$\begin{cases} \ddot{x}_L = \dfrac{1}{m_{eff}}(p_H A_H - B_H \dot{x}_L - m_{eff} g - F_f - F_{L\_HT} \\ \dot{p}_H = \dfrac{1}{V_{av} + V_{accu\_midstroke} - A_H x_L}(\dot{m}_g RT + p_H A_H \dot{x}_L - R_H p_H) \end{cases} \tag{3.11}$$

From equation (3.11), we can see another problem of the hydro-pneumatic tensioners. Any volume variation with vessel heave motion will cause the pressure change in the hydro-pneumatic cylinder, thus the tension fluctuation in the wire-line.

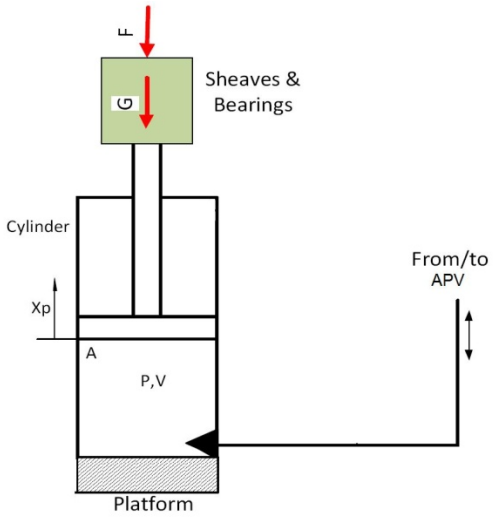

Fig. 3.2 Model Representation of the Hydro-Pneumatic Tensioner

3.2.3. Integrated Electrical and Hydro-pneumatic Tensioning System Model

A non-modeled dynamic force disturbance $\bar{\Delta}(t, x_L, z, \dot{x}_L, \dot{z})$ acting at the riser top is introduced into the system model. This disturbance force is too complicated to derive an explicit formula, which would depend on many factors such as $x_L, z, \dot{x}_L, \dot{z}$, the initial tension in the riser, the weight of the riser, the current profile and current magnitude acting on the riser, and the shape of the riser, etc. In addition, the $\bar{\Delta}(t, x_L, z, \dot{x}_L, \dot{z})$ may include non-modeled force interacting between the electrical tensioners and hydro-pneumatic tensioners. It is noted that there would be a force from the riser acting on the tensioners in the horizontal plane. This force will affect the motions in sway and surge. However, we do not consider sway and surge motion in this chapter.

3.2.3.1. Non-Linear Dynamic Model

Assuming that the number of hydro-pneumatic tensioners is N_{HT} and the number of electrical tensioners is N_{ET}, the load force of the wet riser and circulating mud is F_{L_Total}. The system model of the hybrid riser tensioning system can be rewritten as follows:

$$\begin{cases} \ddot{x}_L = \dfrac{1}{\left(\dfrac{N_{ET}J_{eff}}{r_{winch}^2} + N_{HT}m_{eff}\right)}\left[\dfrac{3N_{ET}PL_{md}I_{fd}}{2r_{winch}}i_q + N_{HT}p_HA_H - (N_{ET}B_E + N_{HT}B_H)\dot{x}_L \right. \\ \qquad\qquad \left. -N_{HT}m_{eff}g - N_{HT}F_f - F_{L\_Total} - \bar{\Delta}(t, x_L, z, \dot{x}_L, \dot{z})\right] \\ i_q = \dfrac{1}{L_q}\left(v_q - R_Ei_q - \dfrac{L_{md}I_{fd}P}{r_{winch}}\dot{x}_L\right) \\ \dot{p}_H = \dfrac{1}{V_{av} + V_{accu\_midstroke} - A_Hx_L}(\dot{m}_gRT + p_HA_H\dot{x}_L - R_Hp_H) \end{cases} \tag{3.12}$$

For the purpose of control design, we rewrite equation (3.12) in a standard state space form as follows:

$$\begin{cases} \dot{x}_1 = x_2 \\ \dot{x}_2 = \theta_{21}x_4 + \theta_{22}x_2 + \theta_{23}x_3 + \Delta(t, x_L, z, \dot{x}_L, \dot{z}) \\ \dot{x}_3 = \theta_{31}g(x_1)x_2x_3 + \theta_{32}g(x_1)x_3 + \theta_{33}g(x_1)\dot{m}_g \\ \dot{x}_4 = \theta_{41}x_2 + \theta_{42}x_4 + \theta_{43}v_q \end{cases} \tag{3.13}$$

with $x_1 = x_L$, $x_2 = \dot{x}_L$, $x_3 = p_H$, $x_4 = i_q$

$$\theta_{21} = \frac{3N_{ET}PL_{md}I_{fd}}{2r_{winch}\left(\frac{N_{ET}J_{eff}}{r_{winch}^2}+N_{HT}m_{eff}\right)};\ \theta_{22} = -\frac{N_{ET}B_E+N_{HT}B_H}{\frac{N_{ET}J_{eff}}{r_{winch}^2}+N_{HT}m_{eff}};\ \theta_{23} = \frac{N_{HT}A_H}{\frac{N_{ET}J_{eff}}{r_{winch}^2}+N_{HT}m_{eff}};$$

$$\Delta(t, x_L, z, \dot{x}_L, \dot{z}) = -\frac{F_{L\_Total}+N_{HT}m_{eff}g+N_{HT}F_f}{\frac{N_{ET}J_{eff}}{r_{winch}^2}+N_{HT}m_{eff}} - \frac{\bar{\Delta}(t,x_L,z,\dot{x}_L,\dot{z})}{\frac{N_{ET}J_{eff}}{r_{winch}^2}+N_{HT}m_{eff}};$$

$$\theta_{31} = A_H;\ g(x_1) = \frac{1}{V_{av}+V_{accu\_midstroke}-A_Hx_L};\ \theta_{32} = R_H;\ \theta_{33} = RT$$

$$\theta_{41} = -\frac{L_{md}I_{fd}P}{L_qr_{winch}};\ \theta_{42} = -\frac{R_E}{L_q};\ \theta_{43} = \frac{1}{L_q} \tag{3.14}$$

The tension force on the wire line of the hydro-pneumatic tensioner:

$$F_{HT} = p_H A_H - B_H \dot{x}_L - m_{eff} g - F_f \tag{3.15}$$

whose rate of change mainly depends on the pressure change of the cylinder.

And the tension force delivered by the electrical tensioner:

$$F_{ET} = \frac{3PL_{md}I_{fd}}{2r_{winch}} i_q - B_H \dot{x}_L \tag{3.16}$$

whose rate of change depends on the current change of the machine. Based on the mathematical interpretation, we can easily see that the electrical tension rate of change could be much faster than that of the hydro-pneumatic tensioner.

3.2.3.2. Small Signal Model

The model described in equations (3.13) and (3.14) is the physical first principle model. A close look shows that this system is of non-linear form. A linear model can be obtained by introducing deviation variables based on steady-state operating points. Using Taylor expansion, we can further linearize the equations (3.13).

Consider that the state variables $x_i(t)$, the steady state equilibrium values X_i and the respective perturbed variables $\tilde{x}_i(t)$ are related by

$$x_i(t) = X_i + \tilde{x}_i(t)$$

Also consider that, equivalently, the control inputs and the disturbance can be related with their respective constant value at the equilibrium point and perturbed values through:

$$u(t) = [\dot{m}_g \quad v_q]^T = U + \tilde{u}(t)$$

$$\Delta(t, x_L, z, \dot{x}_L, \dot{z}) = \Delta_0 + \tilde{\Delta}(t, x_L, z, \dot{x}_L, \dot{z})$$

If we suppose that the load force F_{L_Total} is constant, the small signal state space representation of the riser hybrid tensioning system is indicated below in equation (3.17):

$$\begin{cases} \dot{\tilde{x}}_1 = \tilde{x}_2 \\ \dot{\tilde{x}}_2 = \tilde{\theta}_{21}\tilde{x}_2 + \tilde{\theta}_{22}\tilde{x}_3 + \tilde{\theta}_{23}\tilde{x}_4 + \tilde{\Delta}(t, x_L, z, \dot{x}_L, \dot{z}) \\ \dot{\tilde{x}}_3 = \tilde{\theta}_{31}\tilde{x}_1 + \tilde{\theta}_{32}\tilde{x}_2 + \tilde{\theta}_{33}\tilde{x}_3 + \tilde{\theta}_{34}\tilde{u}_1 \\ \dot{\tilde{x}}_4 = \tilde{\theta}_{41}\tilde{x}_2 + \tilde{\theta}_{42}\tilde{x}_4 + \tilde{\theta}_{43}\tilde{u}_2 \end{cases} \tag{3.17}$$

where

$$\tilde{\theta}_{21} = -\frac{N_{ET}B_E + N_{HT}B_H}{\frac{N_{ET}J_{eff}}{r_{winch}^2} + N_{HT}m_{eff}};\ \tilde{\theta}_{22} = \frac{N_{HT}A_H}{\frac{N_{ET}J_{eff}}{r_{winch}^2} + N_{HT}m_{eff}};\ \tilde{\theta}_{23} = \frac{3N_{ET}PL_{md}I_{fd}}{2r_{winch}\left(\frac{N_{ET}J_{eff}}{r_{winch}^2} + N_{HT}m_{eff}\right)};$$

$$\tilde{\Delta}(t, x_L, z, \dot{x}_L, \dot{z}) = -\frac{\bar{\Delta}(t, x_L, z, \dot{x}_L, \dot{z})}{\frac{N_{ET}J_{eff}}{r_{winch}^2} + N_{HT}m_{eff}};$$

$$\tilde{\theta}_{31} = \frac{A_H^2X_2X_3 + A_HR_HX_3 + A_HRT\dot{M}_g}{(V_{av} + V_{accu\_midstroke} - A_Hx_1)^2};\ \tilde{\theta}_{32} = \frac{A_HX_3}{V_{av} + V_{accu\_midstroke} - A_Hx_1};\ \tilde{\theta}_{33} = \frac{A_HX_2 + R_H}{V_{av} + V_{accu\_midstroke} - A_Hx_1};$$

$$\tilde{\theta}_{34} = \frac{RT}{V_{av} + V_{accu\_midstroke} - A_Hx_1};\quad \tilde{\theta}_{41} = -\frac{PL_{md}I_{fd}}{L_qr_{winch}};\quad \tilde{\theta}_{42} = -\frac{R_E}{L_q};\quad \tilde{\theta}_{43} = \frac{1}{L_q} \tag{3.18}$$

Equation (3.17) and (3.18) can be rewritten into the standard form:

$$\begin{cases} \dot{\tilde{\boldsymbol{x}}} = \boldsymbol{A}\tilde{\boldsymbol{x}} + \boldsymbol{B}\tilde{\boldsymbol{u}} + \boldsymbol{B_d}\tilde{\boldsymbol{d}} \\ \tilde{\boldsymbol{y}} = \boldsymbol{C}\tilde{\boldsymbol{x}} + \boldsymbol{D}\tilde{\boldsymbol{u}} + \boldsymbol{D_d}\tilde{\boldsymbol{d}} \end{cases} \tag{3.19}$$

$$\dot{\tilde{x}} = \begin{bmatrix} 0 & 1 & 0 & 0 \\ 0 & \tilde{\theta}_{21} & \tilde{\theta}_{22} & \tilde{\theta}_{23} \\ \tilde{\theta}_{31} & \tilde{\theta}_{32} & \tilde{\theta}_{33} & 0 \\ 0 & \tilde{\theta}_{41} & 0 & \tilde{\theta}_{42} \end{bmatrix}\dot{x} + \begin{bmatrix} 0 & 0 \\ 0 & 0 \\ \tilde{\theta}_{34} & 0 \\ 0 & \tilde{\theta}_{43} \end{bmatrix}\tilde{u} + \begin{bmatrix} 0 \\ \tilde{\theta}_{24} \\ 0 \\ 0 \end{bmatrix}\tilde{d} \tag{3.20}$$

Measurements are set to be: $[y_1 \quad y_2]^T = [x_1 \quad x_2]^T$

$$\tilde{y} = \begin{bmatrix} \tilde{\theta}_{51} & 0 & 0 & 0 \\ 0 & \tilde{\theta}_{51} & 0 & 0 \end{bmatrix}\tilde{x} \qquad with\ \tilde{\theta}_{51} = \tilde{\theta}_{52} = 1 \tag{3.21}$$

According to the data given in Table 3.1, the minimum required tension F_{L_min} at the riser top is calculated as follows:

$$F_{L\_min} = \Big[(6.8 \times 10^5 kg + 1.99 \times 10^4 kg) \times 1.05 - 4.191 \times 10^5 kg \times 0.96 + 0.64 m^2$$

$$\times \left(1444 \frac{kg}{m^3} \times 3000m - 1030 \frac{kg}{m^3} \times 3000m\right)\Big] \times 9.8 \frac{m}{s^2} = 10919.18\ kN$$

Table 3.1: Nominal input data – the parameters of the riser

Parameter	*Description*	*Value*	*Unit*
H_r	Length of drilling riser	3000	m
A_r	Internal cross section of the riser	0.64	m^2
M_r	Mass of marine riser + LMRP + BOP	6.8×10^5	kg
M_{TR}	Mass of tensioner ring	1.99×10^4	kg
D_m	Density of drilling fluid	1444	kg/m^3
D_r	100 x 15m joints with buoyancy	4191	$kg/section$
R_f	Reduction factor for fleet angle and mechanical efficiency	0.95	
N_{ET}	Number of electrical tensioners	4	
N_{HT}	Number of hydro-pneumatic tensioners	4	

The stability requirement of the riser operation puts high reliability demand on the tensioning system. According to $(n-1)$ rule, the operating tension setting is required to ensure, so that the effective tension should be sufficiently high to keep positive in all parts of the riser in case of one pair of tensioners' failure. (In most case the minimum effective tension is encountered at the bottom of the riser.)

The effective tension of the equilibrium point is determined by:

$$F_{L\_Total} = \frac{F_{L\_min}(N_{HT}+N_{ET})}{R_f(N_{HT}+N_{ET}-2)} = 15325.16\ kN \tag{3.22}$$

Table 3.2 lists the steady state parameters of a hydro-pneumatic tensioner installed on the Transocean rig:

Table 3.2: Nominal input data – the parameters of the hydro-pneumatic tensioner

Parameter	*Description*	*Value*	*Unit*
A_H	Piston Area	0.173	m^2
V_{av}	Gas Bank Volume	3.2	m^3
$V_{accu\_midstroke}$	Gas Volume of Accumulator	35	$liter$
m_{eff}	Piston Mass + Sheave	2920	kg
B_H	Viscous Coefficient	40	$N.s/m$
F_f	Friction Force	4%	
R_H	Flow Resistance	1.72×10^{-5}	m^3/s
R	Gas Constant	287	$Pa * m^3/kg/K$
T	Gas Temperature	290	K

The following is the parameters of the permanent magnet electrical winch derived from the data of one manufacture, DRS:

Table 3.3: Nominal input data – the parameters of the electrical tensioner

Parameter	*Description*	*Value*	*Unit*
r_{winch}	Winch Radium	0.62	m
J_{eff}	Moment of Inertia	1580	$kg.m^2$
B_E	Viscous Coefficient	20	$N.s/m$
P	Motor Pole Pair	15	
R_E	Stator Resistance	0.2159	ohm
L_q	q axis Stator Inductance	12.66	mH
$\lambda_d = L_{md} I_{fd}$	d axis Stator Flux	33.4	Wb

The equilibrium state space variables are calculated as follows:

$X_1 = 0,\ X_2 = 0,\ X_3 = 111.5\ bar,\quad X_4 = 1.592\ kA\ (rms),\quad U_1 = 0\ kg/s,\quad U_2 = 343.8\ V(rms)$

All the coefficients of equation (3.17) are calculated shown in Table 3.4.

As a pre-requisite step of the control design, scaling is applied on this small signal model (3.17), so that the system performance is bounded by the preset maximum requirements in Table 3.5. Decisions are made on the expected maximum magnitude of disturbances and reference

changes, on the allowed maximum magnitudes of the input signals. The system small signal model after scaling is shown in Table 3.6.

Table 3.4: The parameters of the hybrid tensioning system model before scaling

Parameter	*Value*
$\tilde{\theta}_{21}$	-0.00853
$\tilde{\theta}_{22}$	2.4608×10^{-5}
$\tilde{\theta}_{23}$	0.1724
$\tilde{\theta}_{24}$	1
$\tilde{\theta}_{31}$	1.023
$\tilde{\theta}_{32}$	3.4115
$\tilde{\theta}_{33}$	1.785×10^{-6}
$\tilde{\theta}_{34}$	8669.8
$\tilde{\theta}_{41}$	-6.382×10^{4}
$\tilde{\theta}_{42}$	-17.05
$\tilde{\theta}_{43}$	79.00
$\tilde{\theta}_{51}$	1
$\tilde{\theta}_{52}$	1

Table 3.5: The maximum deviation of the hybrid tensioning system model

Parameter	*Description*	*Value*	*Unit*
$\tilde{\Delta}_{max}$	Unmodeled Tension disturbance	290.03	kN
x_{1max}	Wire-Line Displacement	4.8	m
x_{2max}	Wire-Line Velocity	4.5	m/s
x_{3max}	Cylinder Pressure	2.09	bar
x_{4max}	q axis stator current	29.9	A
z_{max}	Vessel Heave	4.8	m
v_{qmax}	q axis stator voltage	170	V
$\dot{m}_{gmax}$	Gas mass flow rate	1.95	g/s
e_{max}	control error	0.25	m

Table 3.6: The parameters of the hybrid tensioning system model after scaling

Parameter	*Value*
$\tilde{\theta}_{21}$	-0.00853
$\tilde{\theta}_{22}$	2.4608×10^{-5}
$\tilde{\theta}_{23}$	0.1724
$\tilde{\theta}_{24}$	6.445×10^{4}
$\tilde{\theta}_{31}$	1.023
$\tilde{\theta}_{32}$	3.4115
$\tilde{\theta}_{33}$	1.785×10^{-6}
$\tilde{\theta}_{34}$	0.0809
$\tilde{\theta}_{41}$	-6.382×10^{4}
$\tilde{\theta}_{42}$	-17.05
$\tilde{\theta}_{43}$	449.16
$\tilde{\theta}_{51}$	19.2
$\tilde{\theta}_{52}$	18

The controllability matrix for this system model is a 4×8 matrix given by:

$$C = [B \vdots \quad AB \quad A^2B \quad A^3B \quad A^4B] \text{ with } rank(C) = 4$$

The rank of the matrix C is 4 implies the system under consideration is controllable.

The observability matrix for this system model is a 8×4 matrix given by:

$$O = [C \vdots \quad CA \quad CA^2 \quad CA^3 \quad CA^4] \text{ with } rank(O) = 4$$

The rank of the matrix O is 4 implies the system under consideration is observable.

The linear process model transfer function can be represented as equation (3.23) and the controller design could be studied as a first order approximation.

$$\tilde{\boldsymbol{y}}(\boldsymbol{s}) = \boldsymbol{G}(\boldsymbol{s})\tilde{\boldsymbol{u}}(\boldsymbol{s}) + \boldsymbol{G_d}(\boldsymbol{s})\tilde{\boldsymbol{d}}(\boldsymbol{s}) \tag{3.23}$$

where $\boldsymbol{G}(s)$ represents the effect of the inputs $\tilde{\boldsymbol{u}}$ on the outputs $\tilde{\boldsymbol{y}}$, whereas $\boldsymbol{G_d}(s)$represents the effect on $\tilde{\boldsymbol{y}}$ of the disturbances $\tilde{\boldsymbol{d}}$. The transfer functions are given by (3.24):

$$G(s) = \begin{bmatrix} G_{11}(s) & G_{12}(s) \\ G_{21}(s) & G_{22}(s) \end{bmatrix} = \frac{1}{J(s)} \begin{bmatrix} N_{11}(s) & N_{12}(s) \\ N_{21}(s) & N_{22}(s) \end{bmatrix} \tag{3.24}$$

$$G_d(s) = \begin{bmatrix} G_{13}(s) \\ G_{23}(s) \end{bmatrix} = \frac{1}{J(s)} \begin{bmatrix} N_{13}(s) \\ N_{23}(s) \end{bmatrix}$$

Table 3.7: Coefficients of Open-Loop Transfer Function Matrix

$$J(s) = \frac{1}{s^4 - (\tilde{\theta}_{21}+\tilde{\theta}_{33}+\tilde{\theta}_{42})s^3 + (\tilde{\theta}_{21}\tilde{\theta}_{33}+\tilde{\theta}_{21}\tilde{\theta}_{42}-\tilde{\theta}_{22}\tilde{\theta}_{32}-\tilde{\theta}_{23}\tilde{\theta}_{41}+\tilde{\theta}_{33}\tilde{\theta}_{42})s^2 + (\tilde{\theta}_{22}\tilde{\theta}_{32}\tilde{\theta}_{42}+\tilde{\theta}_{23}\tilde{\theta}_{33}\tilde{\theta}_{41}-\tilde{\theta}_{21}\tilde{\theta}_{33}\tilde{\theta}_{42}-\tilde{\theta}_{22}\tilde{\theta}_{31})s + \tilde{\theta}_{22}\tilde{\theta}_{31}\tilde{\theta}_{42}}$$

$$N_{11}(s) = \tilde{\theta}_{22}\tilde{\theta}_{34}\tilde{\theta}_{51}s - \tilde{\theta}_{22}\tilde{\theta}_{34}\tilde{\theta}_{42}\tilde{\theta}_{51} \qquad N_{12}(s) = \tilde{\theta}_{23}\tilde{\theta}_{43}\tilde{\theta}_{51}s - \tilde{\theta}_{23}\tilde{\theta}_{43}\tilde{\theta}_{33}\tilde{\theta}_{51}$$

$$N_{21}(s) = \tilde{\theta}_{22}\tilde{\theta}_{34}\tilde{\theta}_{52}s^2 - \tilde{\theta}_{22}\tilde{\theta}_{34}\tilde{\theta}_{42}\tilde{\theta}_{52}s \qquad N_{22}(s) = \tilde{\theta}_{23}\tilde{\theta}_{43}\tilde{\theta}_{52}s^2 - \tilde{\theta}_{23}\tilde{\theta}_{43}\tilde{\theta}_{33}\tilde{\theta}_{52}s$$

$$N_{13}(s) = \tilde{\theta}_{24}\tilde{\theta}_{51}s^2 - \left(\tilde{\theta}_{33}\tilde{\theta}_{24}\tilde{\theta}_{51} + \tilde{\theta}_{42}\tilde{\theta}_{24}\tilde{\theta}_{51}\right)s + \tilde{\theta}_{33}\tilde{\theta}_{42}\tilde{\theta}_{24}\tilde{\theta}_{51}$$

$$N_{23}(s) = \tilde{\theta}_{24}\tilde{\theta}_{52}s^2 - \left(\tilde{\theta}_{33}\tilde{\theta}_{24}\tilde{\theta}_{52} + \tilde{\theta}_{42}\tilde{\theta}_{24}\tilde{\theta}_{52}\right)s + \tilde{\theta}_{33}\tilde{\theta}_{42}\tilde{\theta}_{24}\tilde{\theta}_{52}$$

The model described in equation (3.23) and (3.24) is a multi-input-multi-output (MIMO) linear system, as shown in Fig. 3.3.

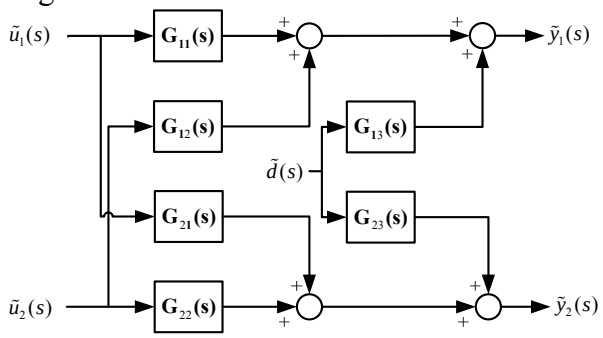

Fig. 3.3 System Block Diagram of the Hybrid Riser Tensioning System

3.3. The Choice of Control Strategy

The active heave compensation (AHC) technology has been used in various deep water applications. Generally speaking such AHC applications is characterized by its big inertia and large disturbance. The control objective of this hybrid riser tensioning system is set to track the desired vessel heave trajectory $\tilde{z}(t)$ in the riser top reference frame, where to keep the tension applied at the riser top to be in a safe range. It is worthwhile to notice that the reference $\tilde{z}(t)$ with $\tilde{z}(t) = \tilde{h}(t) - \tilde{x}_{1d}$, represents the heave motion of the vessel with respect to the riser top position, as shown in Fig. 3.1.

As shown in Fig. 3.3, this is a MIMO system with non-modeled disturbance. It may be argued that a decentralized controller, which consists of several SISO controllers, may be applied by several PID controllers. However, a multivariable control approach could be a better fit than a decentralized control method for the following reasons:

(1) This decentralized controller approximates the MIMO system with independent SISO systems. The multivariable interactions in this decentralized controller are treated as disturbances, which usually causes performance loss and even unstable behaviors. Especially for this application, the wire-line displacement and the riser top tension highly depend on both the electrical tensioners and hydro-pneumatic tensioners.

(2) There is no general framework for a decentralized controller design that allows for disturbance-attenuation and robustness. Instead, a multivariable controller can achieve robust stability and performance with a modern control design theory.

The Fig. 3.4 shows the brief step change simulation of the PI control in this application. It gives slow and very high overshoot performance in this application.

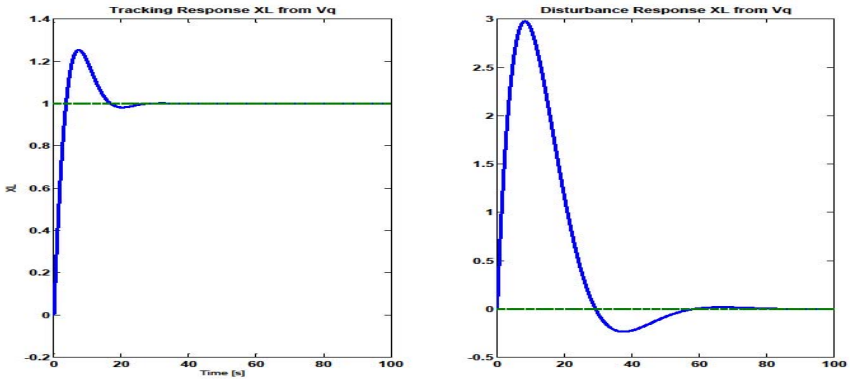

Fig. 3.4 LQG Controller: Step in $\tilde{x}_L$ Reference Signal and $\tilde{\Delta}$ Disturbance Signal

3.3.1. Linear-Quadratic Gaussian Controller Design and its stability analysis

The system model equation (3.19) and (3.20) described in the previous section is a linear dynamic model. And generally speaking, the force disturbance induced on riser $\tilde{\Delta}(t, x_L, z, \dot{x}_L, \dot{z})$ and the wave heave motion $\tilde{z}(t)$ are both random factors, thus could be considered as white Gaussian noises. It is desirable to optimize the control objective by building a quadratic cost function with the system state variables and control inputs. A Linear-Quadratic Gaussian (LQG) controller, as a fundamental optimal control design technique, produces a linear dynamic feedback control law that is easy to compute and implement. Therefore, a LQG controller is designed here for the first trial.

A new state variable is introduced, $\tilde{x}_e = \tilde{x}_1 - \tilde{z}(t)$, which integrates the reference signal into the state space equations, and also augment the plant dynamics with an auxiliary state of integral action. $\tilde{x}_e$ represents the error between the wire-line displacement and the vessel heave motion in the riser top reference frame. Therefore, state variables are chosen as $\tilde{x}_e$, $\tilde{x}_1 = \tilde{x}_L$, $\tilde{x}_2 = \dot{\tilde{x}}_L$, $\tilde{x}_3 = \tilde{p}_H$, $\tilde{x}_4 = \tilde{\iota}_q$.

This LQG controller is designed using Matlab Control System Toolbox. Numerical values of the controller K_r and K_f is given as below:

$$K_r = \begin{bmatrix} -1.7531 & 3.3527 & 11.5687 & 3.1623 \times 10^4 & 2.0687 \times 10^{-4} \\ 1 \times 10^5 & 6.6899 \times 10^3 & 142.4648 & 55.4371 & 0.3817 \end{bmatrix}$$

$$K_f = \begin{bmatrix} 0.0025 & -0.0043 \\ 1.2379 \times 10^{-5} & -0.0040 \\ 6.6703 \times 10^{-10} & -3.3008 \times 10^{-4} \\ 2.7614 \times 10^{-4} & -163.02 \\ -4.2630 \times 10^{-8} & 245.61 \end{bmatrix}$$

Two different simulations were performed:

(1) Step in reference signal $\tilde{x}_L$

(2) Step in disturbance $\tilde{\Delta}$

Results of these simulations are shown in Fig. 3.5.

The left two curves of Fig. 3.5 illustrate the closed loop system response to the control input $\tilde{v}_q$'s step change, while the right two curves illustrate the closed loop system response to the disturbance $\tilde{\Delta}$'s step change. We can observe that the plant stability is obtained by the LQG controller. However, the response is especially bad with respect to the step in the disturbance. This is not surprising, as Skogestad pointed in his book [63] that the LQG controlled system has good stability margins at the plant inputs, and a Kalman filter gives good stability at the inputs to K_f, but there is no guarantee of satisfactory robustness properties, especially for the low frequency sinusoidal disturbance which is typical ocean heave.

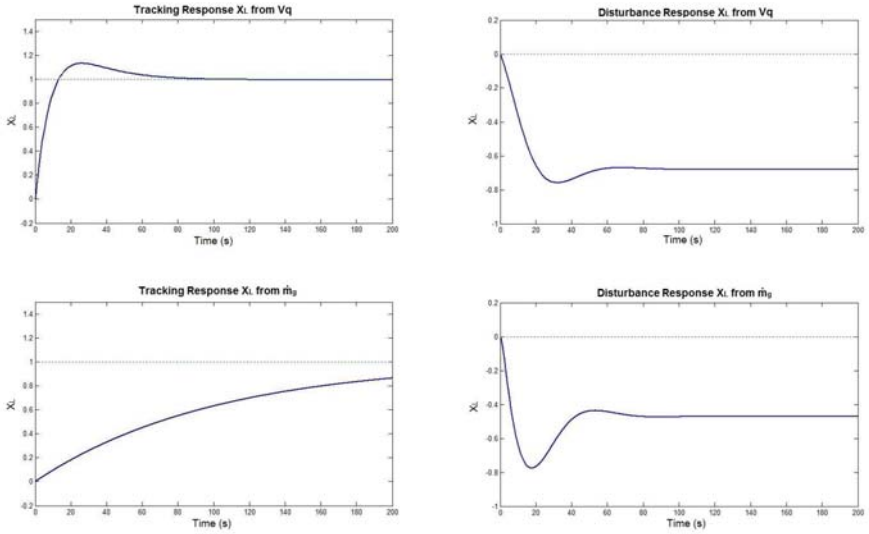

Fig. 3.5 LQG Controller: Step in $\tilde{x}_L$ Reference Signal and $\tilde{\Delta}$ Disturbance Signal

3.3.2. H_∞ Controller Design and its stability analysis

Comparing to LQG control, H_∞ control technique can be used to synthesize controllers achieving robust performance or stabilization, by minimizing the closed loop impact of a disturbance. As we can see that the LQG controller design is based on time domain state equations, while the H_∞ controller design is a frequency domain based technique, which provides better stability margin and robustness for noises or disturbance.

The control objective for the H_∞ controller is set to regulate $|\tilde{x}_L(t) - \tilde{z}(t)|$ as small as possible, where $\tilde{z}(t)$ is the vessel heave by nature. The transfer function described in equation (3.23) is used as the system model in this controller design, recapturing as $\tilde{\boldsymbol{y}}(\boldsymbol{s}) = \boldsymbol{G}(\boldsymbol{s})\tilde{\boldsymbol{u}}(\boldsymbol{s}) + \boldsymbol{G_d}(\boldsymbol{s})\tilde{\boldsymbol{d}}(\boldsymbol{s})$.

The standard setup of the H_∞ control problem can be represented using the schematic block diagram shown in Fig. 3.6. The basic idea of this controller design is to find all stabilizing controllers K such that the H_∞-norm of the closed loop transfer function (3.25) is less than a given positive number γ, which is a much more strict control criterion than the LQG control.

$$\|\boldsymbol{F_l}(\boldsymbol{P},\boldsymbol{K})\|_\infty = \boldsymbol{max}_{\boldsymbol{\omega}} \frac{\|\boldsymbol{\alpha}(\boldsymbol{t})\|_2}{\|\boldsymbol{\omega}(\boldsymbol{t})\|_2} < \boldsymbol{\gamma} \tag{3.25}$$

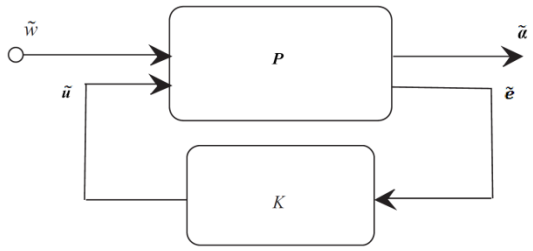

Fig. 3.6 Standard Setup of the H_∞ Control Problem

$\boldsymbol{P}$ is the generalized plant presentation of the system. We define new output vectors of the plant $\boldsymbol{P}$ to be $\tilde{\alpha}$ and $\tilde{e}$, the input vector to be $\tilde{\omega}$ and $\tilde{u}$, where:

$$\tilde{e} = \tilde{r} - \tilde{y} \tag{3.26}$$

$$\tilde{\omega} = \begin{bmatrix} \tilde{d} \\ \tilde{r} \end{bmatrix}$$

Using this control design, there is no need to create a new state variable in purpose, since the generalized transfer function $\boldsymbol{P}$ already takes the reference signal $\tilde{r}$ into consideration, as shown in the new system input $\tilde{\omega}$. Then the new generalized transfer function is augmented to be:

$$\begin{bmatrix} \tilde{\boldsymbol{\alpha}} \\ \tilde{\boldsymbol{e}} \end{bmatrix} = \boldsymbol{P} \begin{bmatrix} \tilde{\boldsymbol{\omega}} \\ \tilde{\boldsymbol{u}} \end{bmatrix} \tag{3.27}$$

In light of control theory in [63], we added weights in the generalized $\boldsymbol{P}$, in order to pursue a synthesis optimization problem with physical meanings. The system block diagram of the control plant for the weighting mixed-sensitivity optimization is shown in Fig. 3.7.

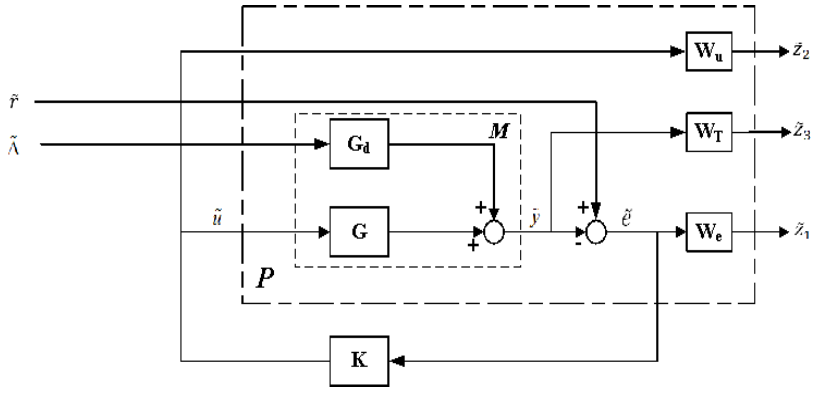

Fig. 3.7 Block Diagram of the Control Plant for the Mixed-Sensitivity Optimization

The control purpose here is making $\tilde{\boldsymbol{e}}(\boldsymbol{t})$ asymptotically zero, i.e. $\tilde{e}(\infty) = 0$, as the disturbance d is applied. The closed-loop transfer functions from $\tilde{\omega}$ to $\tilde{e}$, $\tilde{u}$ and $\tilde{y}$ are:

$S = (I + L)^{-1}$

$R = K(I + L)^{-1} = KS$

$T = L(I + L)^{-1} = LS$

where $L = KM$ is the open loop transfer function of the system, S the sensitivity function, R the control sensitivity function and T the auxiliary sensitivity function. Considering the standard frame of the weighting mixed sensitivity problem:

$$\begin{bmatrix} \boldsymbol{W_e}\tilde{\boldsymbol{e}} \\ \boldsymbol{W_u}\tilde{\boldsymbol{u}} \\ \boldsymbol{W_T}\tilde{\boldsymbol{y}} \\ \tilde{\boldsymbol{e}} \end{bmatrix} = \begin{bmatrix} \boldsymbol{W_e} & -\boldsymbol{W_e G_d} & -\boldsymbol{W_e G} \\ \boldsymbol{0} & \boldsymbol{0} & \boldsymbol{W_u} \\ \boldsymbol{0} & \boldsymbol{W_T G_d} & \boldsymbol{W_T G} \\ \boldsymbol{I} & \boldsymbol{G_d} & \boldsymbol{G} \end{bmatrix} \begin{bmatrix} \tilde{\boldsymbol{r}} \\ \tilde{\boldsymbol{d}} \\ \tilde{\boldsymbol{u}} \end{bmatrix} \tag{3.28}$$

where W_e, W_u and W_T are the weighting functions selected to meet the design requirement. $W_e(j\omega)$ reflects demand of the closed-loop system on the disturbance resistance, $W_u(j\omega)$ denotes the norm limitation of the additive perturbation, and $W_T(j\omega)$ denotes the norm limitation of the additive multiplicative perturbation. This generalized plant $\boldsymbol{P}$ could be rewritten in partitioning form in equation (3.29) with the state space realization:

$$\begin{bmatrix}\tilde{\alpha}\\ \tilde{e}\end{bmatrix} = \begin{bmatrix}P_{11}(s) & P_{12}(s)\\ P_{21}(s) & P_{22}(s)\end{bmatrix}\begin{bmatrix}\tilde{\omega}\\ \tilde{u}\end{bmatrix} \tag{3.29}$$

Based on linear fraction transformation (LFT), the transfer function matrix of the closed-loop system from $\tilde{\omega}$ to $\tilde{\alpha}$ is:

$$F_{\tilde{\alpha}\tilde{\omega}}(s) = \begin{bmatrix}W_e\frac{I}{I+PK}\\ W_u\frac{K}{I+PK}\\ W_T\frac{PK}{I+PK}\end{bmatrix} = \begin{bmatrix}W_eS\\ W_uR\\ W_TT\end{bmatrix} \tag{3.30}$$

The weight functions W_e, W_u and W_T are selected as shown in equation (3.31). We see that $|W_T(j\omega)|^{-1}$ is equal to A at low frequencies and is equal to M at high frequency, and the asymptote crosses 1 at the frequency ω_B^*, which is approximately the band width requirement. A weight of sharper slope is applied on W_e. Fig. 3.8 shows the performance of the weights.

$$W_u = I_{2\times2} \tag{3.31}$$

$$W_T = \frac{s/M+\omega_B^*}{s+\omega_B^*A}I_{2\times2}$$

$$W_e = \frac{\left(s/M^{1/2}+\omega_B^*\right)^2}{\left(s+\omega_B^*A^{1/2}\right)^2}I_{2\times2}$$

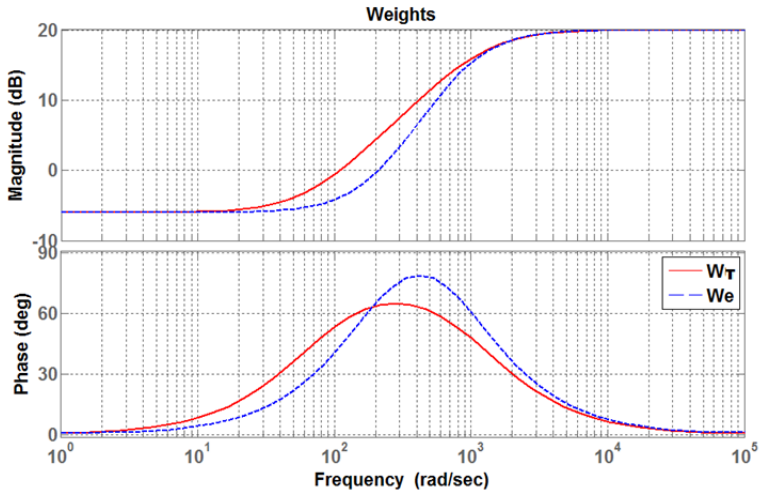

Fig. 3.8 The Weight Performance

The state space presentation of the generalized plant can be written as:

$$\begin{bmatrix} \dot{x} \\ \dot{x}_K \\ \cdots \\ \alpha \\ \cdots \\ y_k \\ y \end{bmatrix} = \left[\begin{array}{cccccccc} A & 0 & \vdots & B_1 & \vdots & B_2 & 0 \\ 0 & A_K & \vdots & 0 & \vdots & 0 & B_K \\ \cdots & \cdots & \cdots & \cdots & \cdots & \cdots & \cdots \\ C_1 & 0 & \vdots & D_{11} & \vdots & D_{12} & 0 \\ \cdots & \cdots & \cdots & \cdots & \cdots & \cdots & \cdots \\ 0 & C_K & \vdots & 0 & \vdots & 0 & D_K \\ C_2 & 0 & \vdots & D_{21} & \vdots & D_{22} & 0 \end{array}\right] \begin{bmatrix} x \\ x_K \\ \cdots \\ \omega \\ \cdots \\ u \\ u_K \end{bmatrix} = \begin{bmatrix} A & B_1 & B_2 \\ C_1 & D_{11} & D_{12} \\ C_2 & D_{21} & D_{22} \end{bmatrix} \begin{bmatrix} x \\ x_K \\ \omega \\ u \\ u_K \end{bmatrix} \tag{3.32}$$

There are several methods to come to the H_∞ controller $K(s)$. The Riccati based approach was studied here. By solving two algebraic Riccati equations as follows, the X_∞ and Y_∞ are obtained.

$$\begin{cases} A^T X_\infty + X_\infty A + C_1^T C_1 + X_\infty(\gamma^{-2} B_1 B_1^T - B_2 B_2^T) X_\infty = 0 \\ A Y_\infty + Y_\infty A^T + B_1^T B_1 + Y_\infty(\gamma^{-2} C_1^T C_1 - C_2^T C_2) Y_\infty = 0 \end{cases}$$

The controller $K(s)$ can be calculated by:

$$K(s) = -Z_\infty L_\infty (sI - A_\infty)^{-1} F_\infty \tag{3.33}$$

where $\boldsymbol{F_\infty = -B_2^T X_\infty}$, $\boldsymbol{L_\infty = -Y_\infty C_2^T}$, $\boldsymbol{Z_\infty = (I - \gamma^{-2} Y_\infty X_\infty)^{-1}}$ and $\boldsymbol{A_\infty = A + \gamma^{-2} B_1 B_1^T X_\infty + B_2 F_\infty + Z_\infty L_\infty C_2}$.

The H_∞ feedback controller K is calculated by Matlab Robust Control Toolbox:

$$K(s) = \begin{bmatrix} \frac{-2.851s^2+1.582s+6.253}{9.084s^2+1.68s+1.717} & \frac{3.045s+6.253}{9.084s^2+1.68s+1.717} \\ \frac{0.1598s^2-0.0645s0.7413}{9.084s^2+1.68s+1.717} & \frac{-5.878s+1.078}{9.084s^2+1.68s+1.717} \end{bmatrix}$$

Two different simulations were performed:

(1) Step in reference signal $\tilde{x}_L$

(2) Step in disturbance $\tilde{\Delta}$

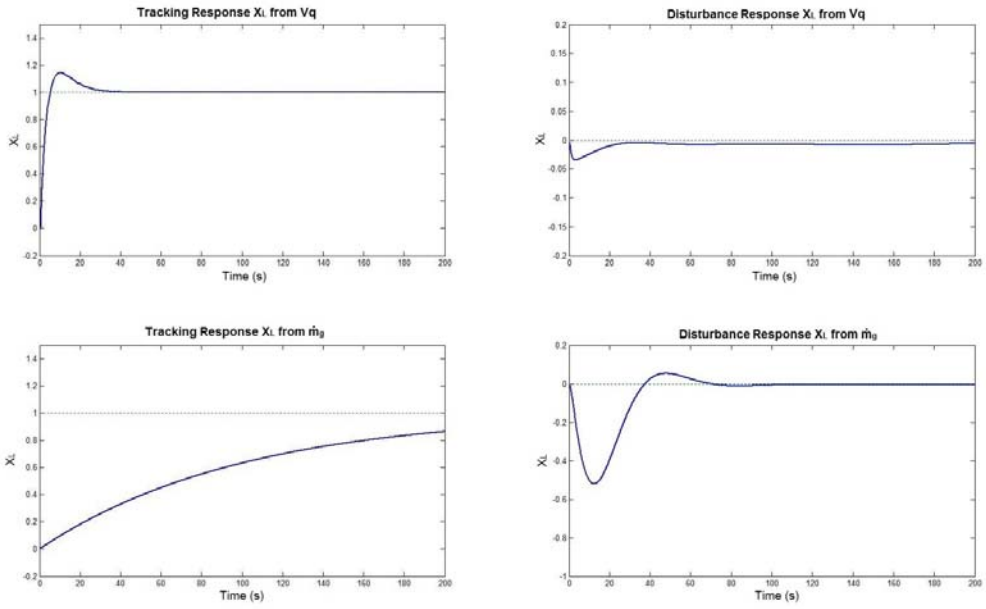

Fig. 3.9 H_∞ Controller: Step in $\tilde{x}_L$ Reference Signal

Results of these simulations are shown in Fig. 3.9. The left two curves illustrate the closed loop system in response to the control input $\tilde{v}_q$'s step change, while the right two curves illustrate the closed loop system in response to the disturbance $\tilde{\Delta}$ step change. We can observe that the step response to control inputs is almost the same as that of the LQG controller, but the

responses to the disturbance are much more satisfactory than the LQG controller, confirming the effectiveness of the H_∞ controller.

3.4. Performance Verification through Matlab Simulation

A Matlab model is simulated for demonstrating the fundamental functionality and performance of this hybrid riser tensioning system. The electrical tensioners, the hydro-pneumatic tensioners and the overall tension controller, the power management controller, the energy storage unit are all implemented here.

3.4.1. The Heave Motion Simulation

The vertical heave motion of the vessel with respect to the riser top can be represented as a sum of sinusoids at different frequencies, amplitudes and phases as follows, see [25] and [26].

$$z(t) = \sum_{i=1}^{N_W}(A_{Wi}k_{Wi}\,sin(\omega_{Wi}t - \varphi_{Wi})) \tag{3.34}$$

where the wave amplitude A_{Wi}, coefficient k_{Wi}, frequency ω_{Wi}, phase φ_{Wi} of the wave i^{th} are given by:

$$\omega_{Wi} = \omega_m + \frac{\omega_m - \omega_M}{N_W} \tag{3.35}$$

$$A_{Wi} = \sqrt{2S_{Wi}\frac{\omega_m - \omega_M}{N_W}}$$

$$S_{Wi} = \frac{1.25}{4}\frac{\omega_0^4}{\omega_{Wi}^4}H_{SW}^2 e^{-1.25(\omega_0/\omega_{Wi})^4}$$

$$k_{Wi} = \frac{\omega_{Wi}^2}{9.8},\ \varphi_{Wi} = 2\pi rand()$$

In equation (3.35), the minimum and maximum wave frequencies are $\omega_m = 0.59\,rad/s$, $\omega_M = 2.1\,rad/s$; the two-parameter Bretschneider spectrum S_{Wi} is used with the significant wave height $H_{SW} = 4\,m$; the modal frequency $\omega_0 = \frac{2\pi}{T_W}$ with the period $T_W = 7.8$; $N_W = 10$; and $rand()$ is a random number between 0 and 1.

The force disturbance $\tilde{\Delta}$ acting from the riser to the wire-lines of the tensioners is modeled as [35]:

$$\tilde{\Delta} = E_r A_r \left(\sum_{n=1}^{N_m} \mp n\pi C_n + \delta\right) \tag{3.36}$$

with C_n being generated by

$$\ddot{C}_n + c_d \dot{C}_n + \frac{E_r A_r n^2 \pi^2}{\rho_r L^2} C_n = \mp \frac{2}{n\pi}(c_d \dot{\delta} + \ddot{\delta}) \tag{3.37}$$

where $\delta = z - x_L$, the riser pipe cross section are $A_r = \frac{\pi d_r^2}{4} = 0.64\ m^2$, the Young's modulus $E_r = 2 \times 10^8 \frac{kg}{m^2}$, the pipe density $\rho_r = 8200 \frac{kg}{m^3}$, the length $L = 3000m$, the damping coefficient $C_d = 0.01 \frac{m^3}{s}$ and the notation $\mp$ takes the positive sign if $n = 2,4,6,$ ... and negative sign of $n = 1,3,5,$ ..., and N_m is the number of modes.

In the simulations, we take the number of modes in equation (3.36) as $N_m = 5$, and the values of C_n are initialized to be zero. In the system simulation, as shown in Fig. 3.10, we tuned the maximum magnitude of the vessel heave to be around $3.5m$ and the maximum force disturbance to be $300\ kN$. We can see that the tension disturbance is stronger with more severe heave motion, which makes sense.

3.4.2. The Simulation of the Hybrid Riser Tensioning System Performance

Fig. 3.11 depicts the wire-line displacement of the tensioners during active heave compensation mode. Comparing the two waveforms, we can see that the wire-line displacement of tensioners strictly follows the vessel heave position, which is a hard-and-fast rule to ensure that the tensions in the ropes keep positive all the time. The ropes never go slack off.

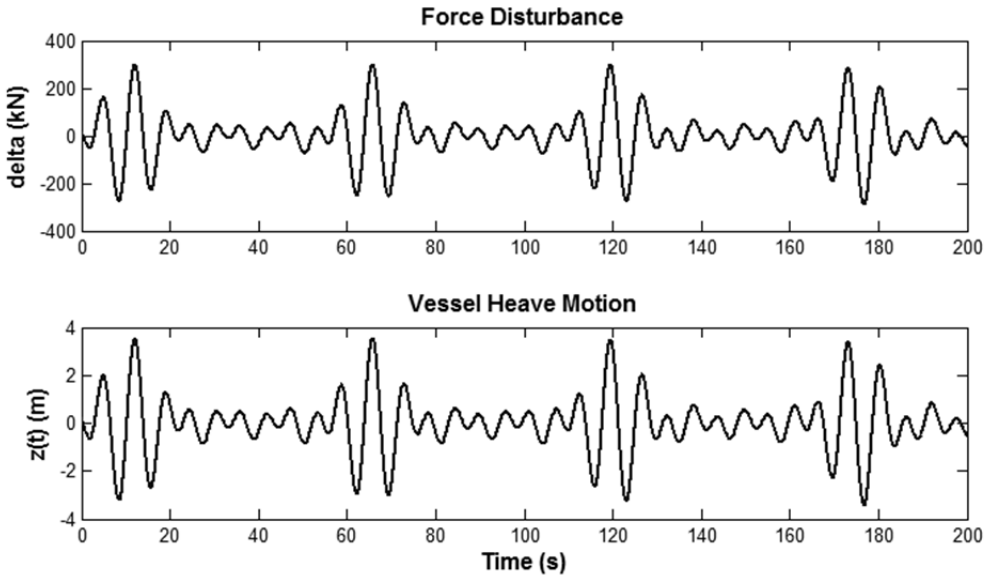

Fig. 3.10 The Simulation of the Force Disturbance $\tilde{\Delta}$ and the Vessel Heave Motion $\tilde{z}(t)$

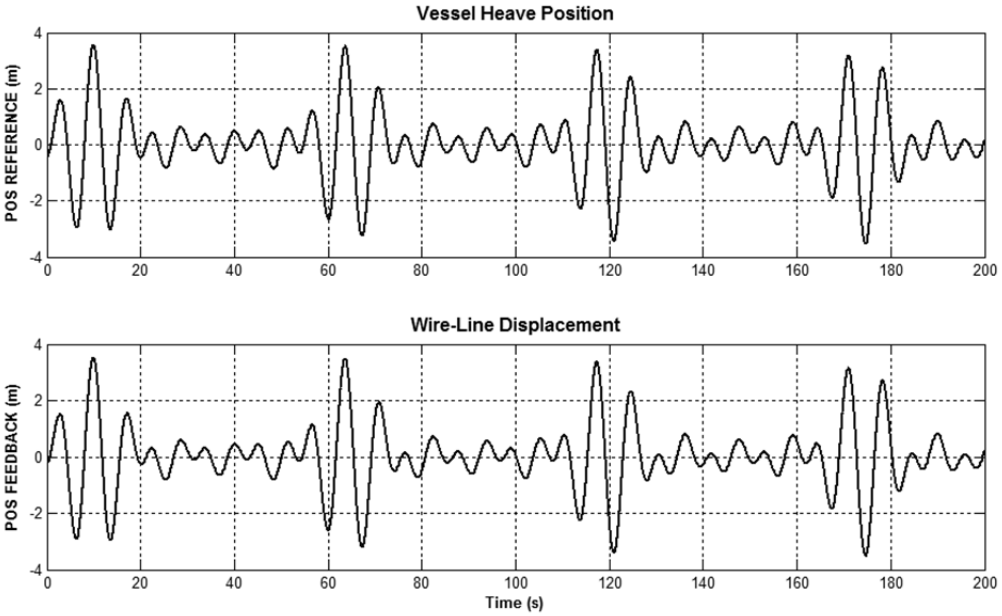

Fig. 3.11 Comparison of the Vessel Heave Position and the Wire-Line Displacement

The Matlab simulation of the hybrid riser tensioning system is performed for the active heave compensation operation, as shown in Fig. 3.12. The top waveform shows us the load

tension required at top of the riser. The steady state tension at the top of the riser is $15.33 \times 10^3\ kN$, and splits among the electrical and hydro-pneumatic tensioners in the middle and bottom waveforms respectively. The dynamically variable tensions for AHC control purpose are superimposed on top of the steady state values. In the hydro-pneumatic tensioner, even we have the control input $\dot{m}_g$ for the hydro-pneumatic tensioning system; the air pressure fluctuation, caused by the heave motion of vessel, puts larger tension fluctuation on riser than the load requirement. Meanwhile, the electrical tensioner produces a counter tension to compensate this tension fluctuation by $180°$, so that the summation of the total tension applied on the riser top is consistent with the load requirement. This confirms our expectation that the electrical tensioning system is able to deliver tensions dynamically with very high changing rate, thus the electrical tension compensates the overshoot part of the hydro-pneumatic tensioners.

Nowadays, as long as the riser string is deployed in water, this cyclical force produced by the pressure fluctuation of hydro-pneumatic tensioners exists on the riser all the time, which gives a big chance to cause any riser fatigue problem. The riser string right now is loosely designed to accommodate this problem. However, if we want to extend the riser operating time or deploy riser in more complicated deeper water environment, it may become necessary to inspect riser in a longer period of intermittent time. Therefore, the reduction of this cyclical loading on the string could be accommodated by being able to control the top tension dynamically and easily. The electrical tensioners help to compensate this cyclical load, make the whole riser system much more robust. This would also be benefit for clip risers, which is usually more sensitive and less robust than flange risers.

Fig. 3.13 shows us that the maximum tension error at the riser top is approximately $14kN$ using the LQG controller and $2.5kN$ using H_∞ controller. Hence, we can conclude that the H_∞ controller provides better performance than the LQG controller.

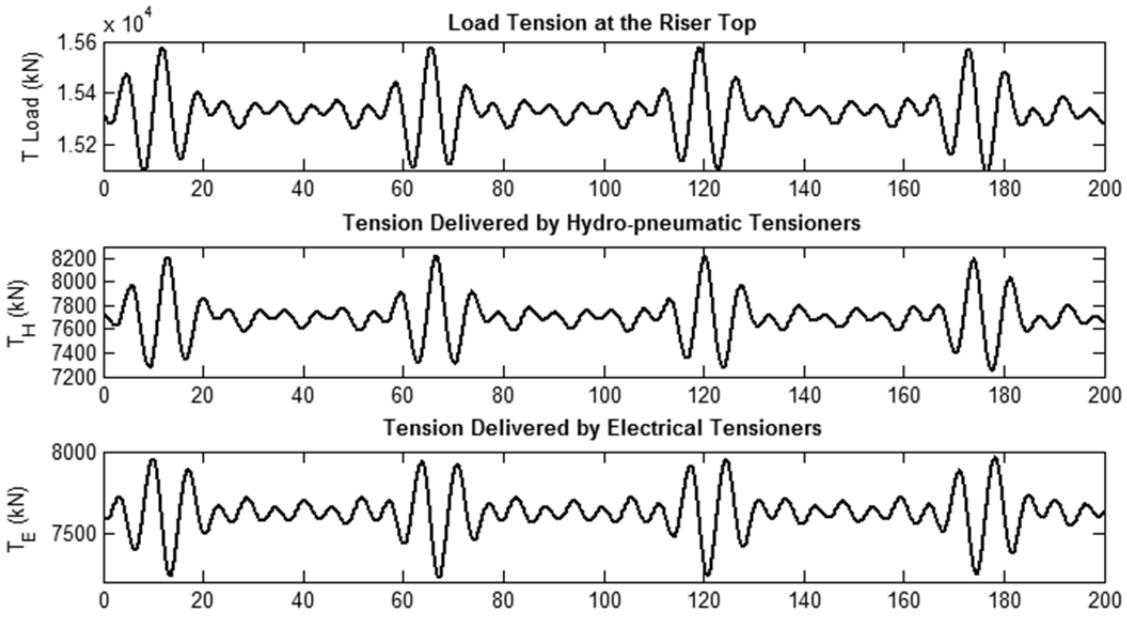

Fig. 3.12 The Simulation Results of the Tension Responses

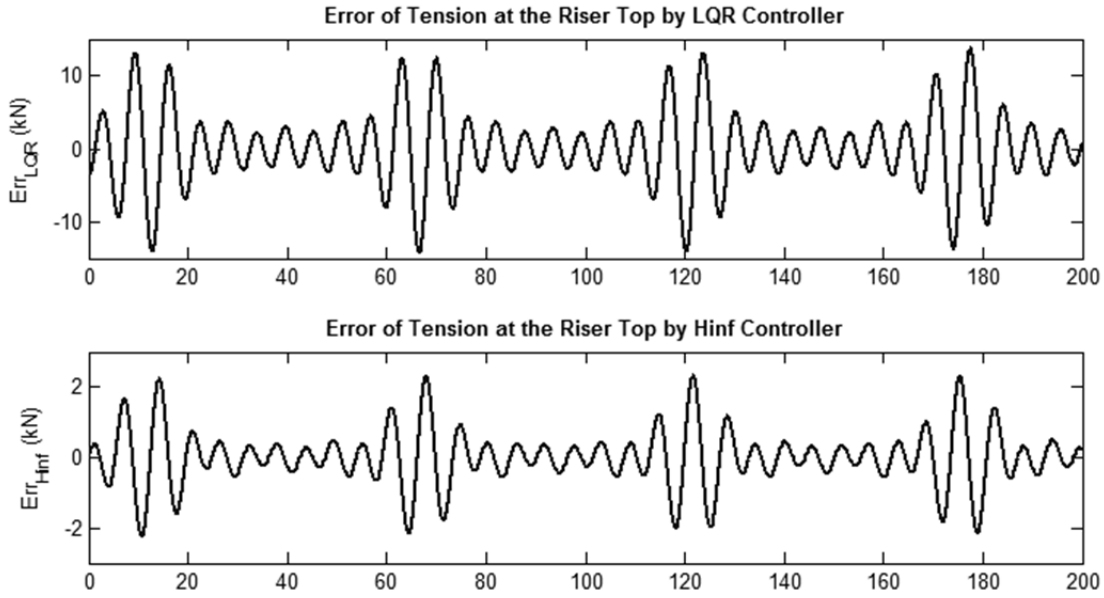

Fig. 3.13 The Simulation Results of the Tension Errors Using Both Controllers

3.4.3. Simulation of the Power Management Performance

The ultra-capacitor can be represented by a simple RC equivalent circuit described in Fig. 3.14. In this application, we would use four Maxwell heavy duty ultra-capacitor modules of rated $125V$, $63F$ in series. The nominal voltage of the UCB would be $500V$. The Equivalent Series Resistance (ESR) for each module is $18\ m\Omega$.

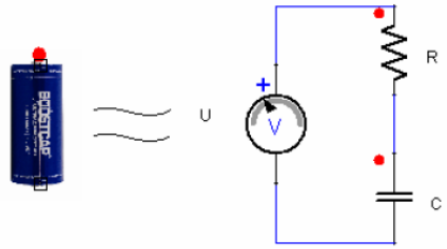

Fig. 3.14 Mathematical Model for One Cell of Ultra-capacitor

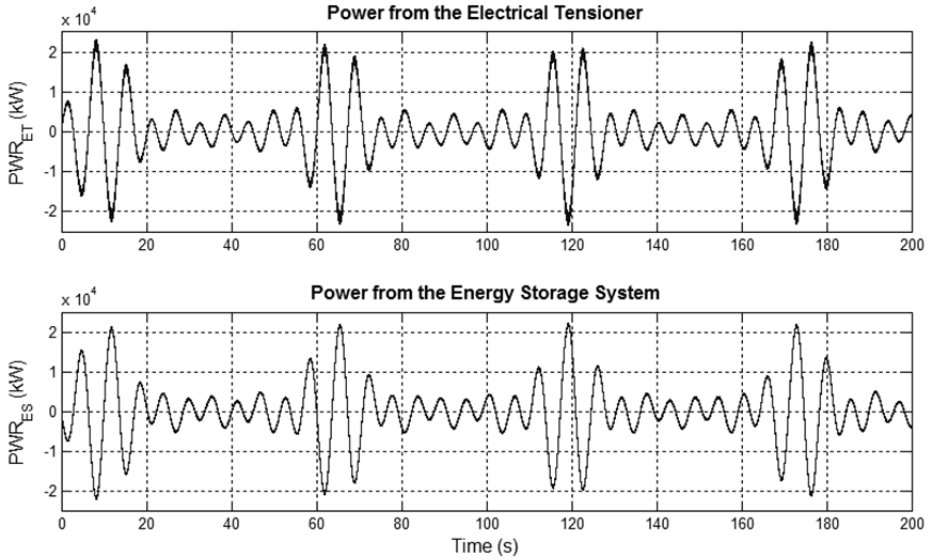

Fig. 3.15 Power Waveforms of the Electrical Tensioner and the Energy Storage System

The instantaneous power flowing into and out of the electrical tensioner is calculated by multiplying the three phase voltages and currents at the machine inlet. The instantaneous power of the energy storage system is calculated by multiplying the voltage and current of the chopper feeder at the DC bus. Fig. 3.15 shows the two waveforms are exactly $180°$ out of phase, which

confirms the effectiveness of the power management strategy. The power demand of the electrical tensioner is compensated by the power into and out of the energy storage system. Hence, the rig power grid would not experience the large power fluctuation. Thus, the reliability of the rig power grid will not be affected by the load of the tensioning system.

The voltage waveforms in Fig. 3.16 show us that the UCB voltage varies between $224V$ and $500V$, which indicates the energy stored in the UCBs varies between 20% and 100% for high sea states. Meanwhile, the DC bus voltage also varies in a much small range following the same pattern of the UCB voltage. So it is verified that the DC bus voltage could be a good indication of the system power demand. It is worthwhile to observe that the UCB voltage decreases, from $400V$ average to $320V$ in $200s$. This explains our discussion earlier that the losses in system will exhaust all stored energy eventually, if we don't charge the UCB from any external source.

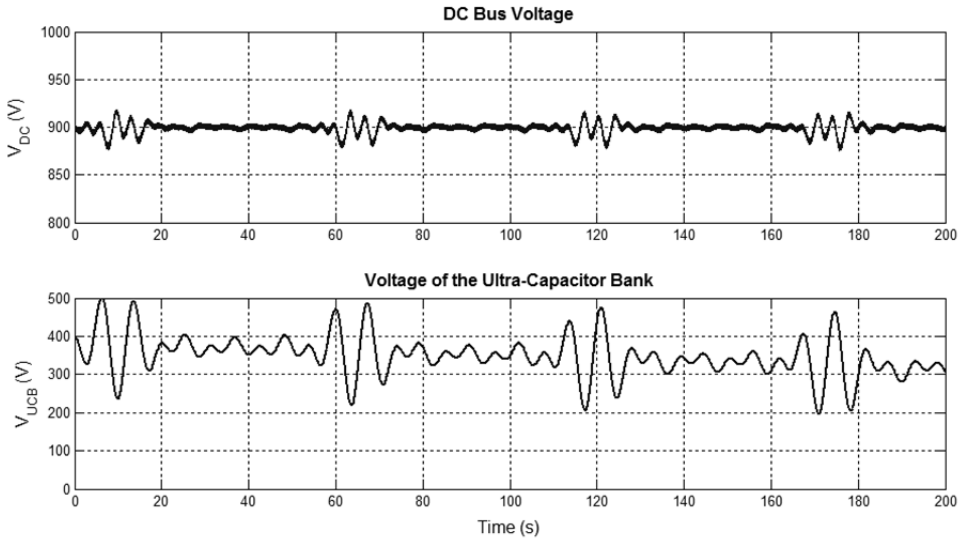

Fig. 3.16 Voltage Waveforms of the DC Bus and the Ultra-Capacitor Terminals (Without Wave Energy)

According to the simulation, we verified our concept that it might be feasible to gain a certain amount of wave energy to compensate the losses, if we pull $5kN$ less tension when the wave velocity is positive and $5kN$ more tension when the wave velocity is negative. As shown

in Fig. 3.17, the voltage level of the UCBs rises from $350V$ to $400V$ as opposite to falling down in Fig. 3.16, which indicates that the UCBs are being charged during regular active heave compensation cycles. We could expect the electrical tensioning system to be a standalone system with very low power transfer with the rig power grid. Hence, the reliability of the whole hybrid riser tensioning system would not be affected by the disturbance of external rig power grid.

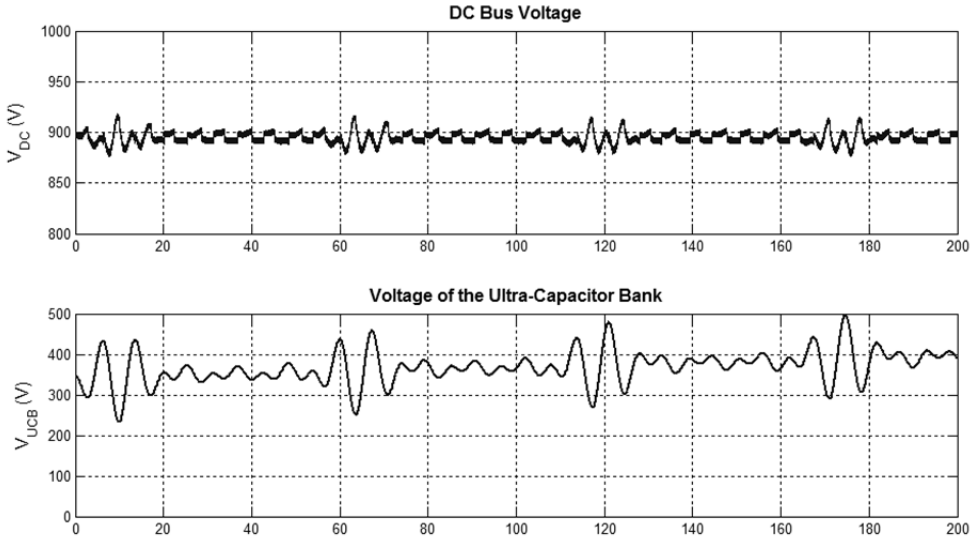

Fig. 3.17 Voltage Waveforms of the DC Bus and the Ultra-Capacitor Terminals (With Wave Energy)

3.5. Performance Verification through Experimental Test

A test bench is built in Transocean Houston factory for further verifying the concept of this hybrid riser tensioning system. The detailed test schematic is shown in Appendix B. The test bench basically consists of one permanent magnet synchronous motor of $4.7kW$ and a forced fan cooled shunt DC motor of $7.5kW$ mounted on the common shaft, an encoder, a PLC (Programmable Logic Controller), a HMI (Human Machine Interface), and the associated auxiliary components.

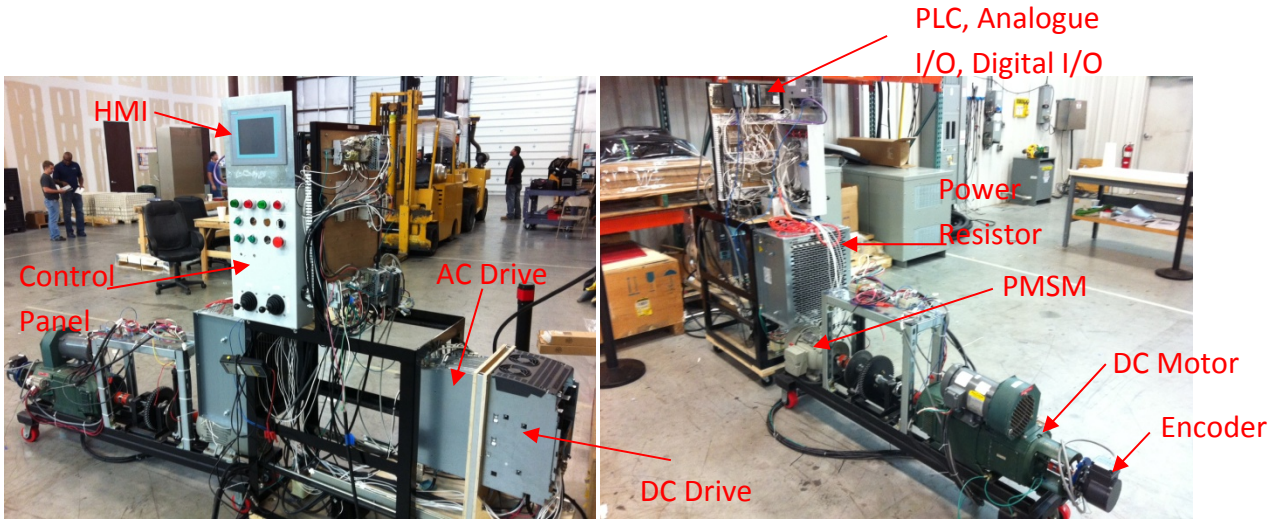

Fig. 3.18 Photos of the Test Bench

The AC motor drive is Siemens S120, including a diode bridge rectifier which converts from $480V$ AC to DC and a bi-directional IGBT inverter which converts DC to variable frequency and variable voltage AC. There is one inductor of $0.46mH$ connected in front of the S120 for providing continuous energy into the AC motor. There is a Siemens power resistor of 20Ω connected on the DC bus for absorbing regenerated energy from the PMSM. For the future work, an ultra-capacitor bank and its chopper will be connected on the same DC bus for energy recycling. The DC motor drive is Siemens DCM, which is bi-directional configuration of back-to-back SCR rectifier. The DC motor field is regulated by another SCR rectifier for variable speed regulation and is supplied by a $480/230V$ one phase transformer. The PLC and its I/O modules are Siemens 315 series, with $24VDC$ power supply, and Profibus communication. The main control algorithm is coded in the PLC using ladder diagram. The reference signals are configured to be finger typing into the HMI. The shaft speed transducer is a four quadrant incremental encoder with two pulse train outputs.

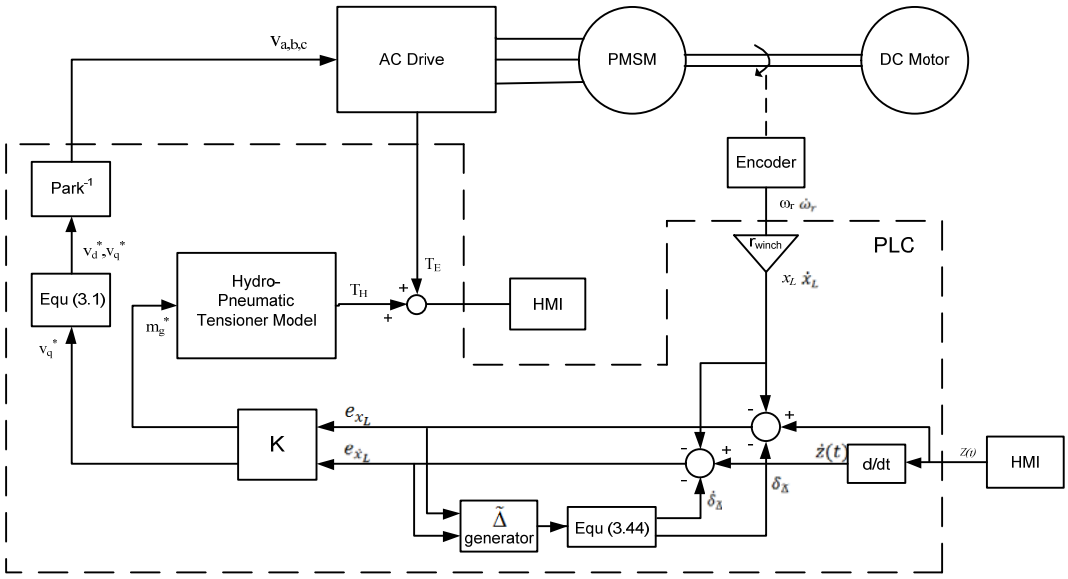

Fig. 3.19 Block Diagram of Test Arrangement

We assume that wire-line can never go slack, i.e. a positive tension always exists in the wire-line. The riser load is simulated by the DC motor drive and the electrical tensioner is simulated by the AC motor drive. The three phase voltage references $v_{a,b,c}$ are calculated in PLC and send to the AC drive for IGBT gating. The hydro-pneumatic tensioner model, as a more predictable device, gives us more confidence of its performance. Its model is programmed in the PLC. And the wire-line displacement x_L, the velocity $\dot{x}_L$ and the tension $T_E + T_H$ are real-time monitored by the HMI. The test data is captured into a computer on $50\ ms$ base, using the software "Service Lab for Simatic". The control block diagram is embedded in the PLC as shown in Fig. 3.19. The H_∞ controller is embedded in the block K.

Fig. 3.20 shows the performance of the electrical riser tensioners on heave compensation. The motor torque and the rotational speed are measured. The speed of the electrical tensioner is driven by the ocean heave, which is simulated by the powerful DC motor, so that the electrical tensioner is forced to follow the speed. The tension generated by the electrical tensioner is the summation of the equivalent value and the disturbance. The H_∞ controller is examined to successfully perform the tension regulation by position chasing. The power consumed by the

electrical tensioner is approximately the opposite of the load power of the DC motor. The torque of the DC motor has more noise, this is because the low speed command gives some difficulty to the DC motor drive to control. Another possible cause is the unstable windings of the old refurbished DC motor.

Overall, this experiment demonstrates that the hybrid riser tensioning system for the active heave compensation operation mode is fully feasible in practice.

Furthermore, the tension response of the electrical tensioner is very fast, in the range of milli-second, compared to that of the hydro-pneumatic tensioner. Fig. 3.21 shows the tension of the electrical tensioner changes from the full torque of $46N.m$ to 13% torque of $5.8N.m$ in less than $50ms$. The data sampling rate of the software "ServiceLab" is $50ms$, the tension changing rate is faster than this. Therefore this software in use was not able to capture the transient behavior of the tension change. The tension step change at $154s$ proves that the system is stable even during the severe heave condition. This experimental result verifies that the feasibility of a faster and more accurate anti-recoil operation control by using the electrical tensioning system.

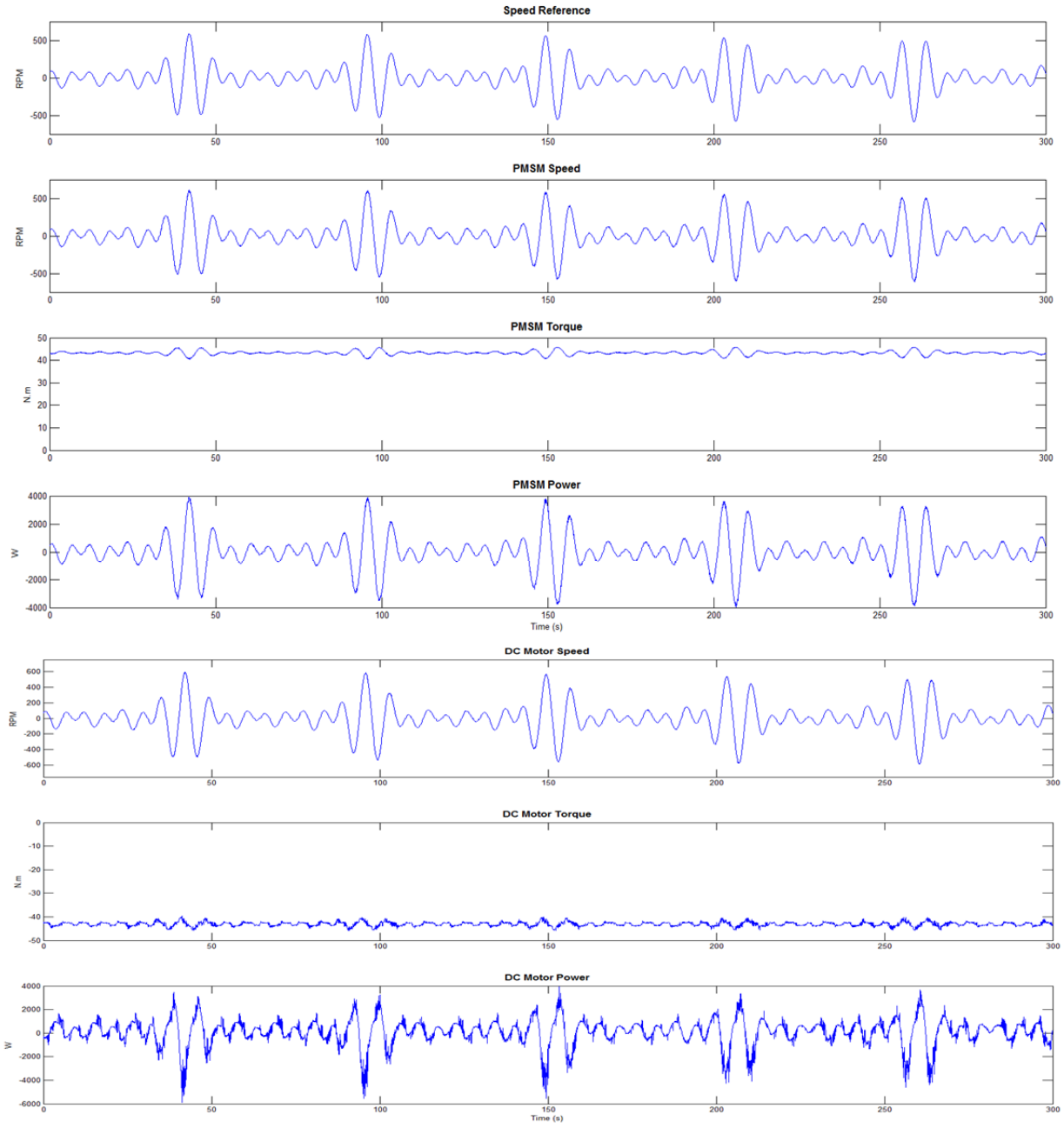

Fig. 3.20 The Electrical Tensioner Test Results for Active Heave Compensation Mode

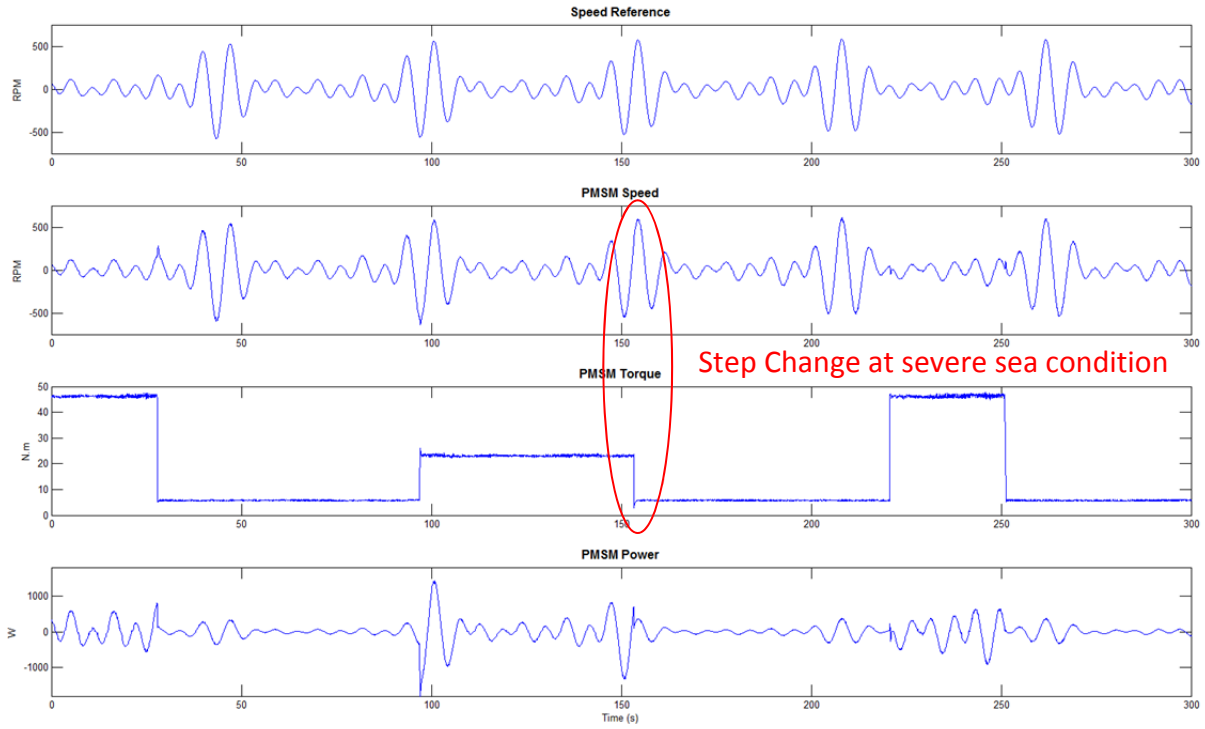

Fig. 3.21 The Torque Fast Step Response of the Electrical Tensioner

Chapter 4: Modeling and Control Design of the Anti-Recoil Control Mode[2]

4.1. Previous Work

Nowadays, the anti-recoil control system of the hydro-pneumatic tensioner becomes a mature and commercially available product by major oil service companies, such as NOV, Control Flow, etc. Various anti-recoil control strategies exist for control the Olmsted valve in the event of a planned or emergency riser disconnect. In most practical cases, the valve position is based on a fixed relationship with the tensioner stroke [51][52]. In some cases requiring more accurate control result, a feedback control loop is used to regulate the valve position. In order to restrict the flow into the reverse direction, some anti-recoil valve is designed to put different flow coefficients for the opposite directions. Some anti-recoil control systems close additional sets of isolation valves at the APVs, which restrict the flow of high pressure air to the high pressure air/oil accumulator. Moreover, large amount of literatures of art and project reports are carried out for specific challenging projects, which describe practical experience of their riser analysis and control strategies, such as [39] - [45].

Most research in the field of the anti-recoil control of the riser tensioning system focuses exclusively on the detailed simulation model on the hydro-pneumatic tensioning system, for the purpose of equipment selection or the Olmsted valve control strategy to meet the recoil criterions.

A. Yu and S. Bhat [46] derive the fundamental equations; evaluate key performance parameters of long-stroke high-tension hydro-pneumatic tensioners for ultra-deepwater application, and their impact on the riser and vessel response. This paper also proposes data measurement locations and methods to collect field data for calibrating the key performance parameters.

[2] Yin Wu, "An Anti-Recoil Control Design using the New Riser Hybrid Tensioning System in Deepwater Drilling", OMAE 2015- 42022

G. Grytoyr et al [47] proposed a model for the dynamic analysis of marine drilling riser disconnect and recoil using general purpose riser finite element analysis program. The model includes the effects of mud column discharge, and the effects of pressure loss in the hydraulic lines for the riser tensioners. This model can be applied to any riser system, both wire-line and direct acting tensioners.

To achieve successful catching of the riser at the moment that the riser is elevated to a suitable height, an algorithm to search catching timing from prediction of both riser motion and vessel heave motion is developed by S. Tanaka et al [48]. It also considers the coupled response of the riser and the dynamic response of internal and external fluid. A deterministic auto-regressive moving average method is used to estimate the heave and riser movement.

A three dimensional non-linear computer model is built by D. Lang et al., [49] to simulate the cases of DP system failure to keep the vessel on station. The recoil control system and the fluid flow model are also developed in this software. This model also takes the lateral loading derived from the riser tension into consideration. The finite element method is used in this model.

G. Grytoyr et al [50][64] developed a model of Completion and Work Over riser systems (CWO) for planned riser disconnect analysis in random sea states. CWO riser system is different from regular marine drilling riser, which may be simultaneously connected to both the riser tensioner system and the top motion compensator system. The Monte Carlo time domain simulation technique and the irregular wave approach are used in this paper.

The above mentioned riser anti-recoil system studies are all designed for current hydro-pneumatic tensioners. However, as mentioned in Chapter I, operational experience shows us a lot of short-comings, such as lack of test, slow and ambiguous disconnect detection method, slow response, etc. Due to these problems, the recoil response of the riser becomes very unpredictable. Catastrophic consequences may occur with high potential.

Furthermore, conservative assumptions regarding vessel response and sea state data are typically applied in the current riser recoil studies, resulting in a restrictive level of conservatism

for drilling riser operability and feasibility, especially for locations with more onerous sea states. In many cases these conservative assumptions regarding system response and environmental data can result in zero operability being predicted whereas in reality some level of operability will exist for these conditions [53][59].

The goal of this anti-recoil control design using the new riser hybrid tensioning system is to extend the drilling or production vessel operating envelope.

4.2. Problem Formulation

Mathematical models can be formulated in various levels of complexity. In this application, we distinguish the models between the process plant model and control plant model. The process plant model is a more comprehensive model of the actual physical plant. The main purpose of this model is to simulate the real operational dynamics, including the hydrodynamics between the riser and seawater, the dynamics of the mud discharge flow, ocean current load disturbance, heave motion, etc. This more detailed process plant model is necessary for verification of the control design. On the other hand, the control plant model is simplified from the process plant model containing only the principle physical properties. It is the "backbone" of the simulation plant model, ensuring that all essential physical effects are properly accounted for a specific control objective.

The mathematical model developed in this chapter describes the dynamic behaviors for both:

(1) normal drilling operation

(2) riser recoil operation

This mathematical model involves

(1) a riser string model with the behavior of mud discharge,

(2) a hydro-pneumatic tensioner model with anti-recoil valve

(3) an electrical tensioner controlled by its variable frequency drive.

The plurality of both electrical and hydro-pneumatic tensioners could be described by simply multiplying the capacity of the model. A Kalman estimator is built, so that the position of the riser bottom, or any other location along the riser string can be detected based on the riser model and the feedback signals of the data logging system mentioned above. This model describes the dynamics of the riser displacement in vertical direction only.

4.2.1. Coordinate Reference Frame

The seabed fixed coordinate frame is used in this model. The connection between the LMRP and the BOP are considered to be the center zero. The positions of all the riser nodes are described in this frame, but focus at their local initial positions before recoil. So the dynamic position of each node initially starts from zero. And the local initial position is fixed based on the natural length of stacked riser string with external tension applied. The hydraulic tensioner piston stroke movement is described with respect to the vessel heave movement. The vessel position follows the heave motion, varying in the sinusoidal way.

4.2.2. Riser System Model

The concept of the riser system model is shown in Fig. 4.1. The model resembles a mass-spring-damper with N lumped masses, totaling the mass of the riser and the mass of the tension ring on top and the mass of the LMRP at bottom. The model is built from engineering principles and uses empirically derived coefficients to set the response [65]. It consists of a series of non-linear differential equations.

The governing equations of motion may be divided into four types, as shown in equation (4.1):

(1) the top node including the mass of tension ring,

(2) the middle, or riser nodes,

(3) the bottom node including the mass of LMRP,

(4) the mud column, considered as one lump of mass.

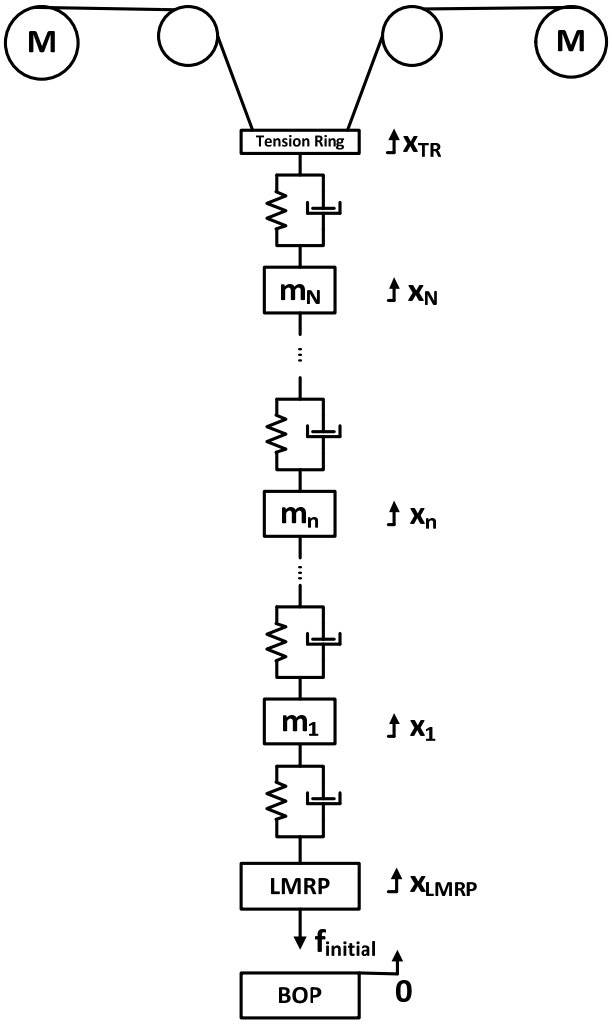

Fig. 4.1 Schematic of Model of Marine Riser and Tensioning System

The system governing equations are listed before:

$$
\begin{cases}
m_{TR}\ddot{x}_{TR} & = (F_{ET}N_{ET} + F_{HT}N_{HT}) - k_r(x_{TR} - x_1) - d_r(\dot{x}_{TR} - \dot{x}_1) - W_{TR} \\
 & \vdots \\
 & \vdots \\
m_n\ddot{x}_n & = k_r(x_{n-1} - x_n) + d_r(\dot{x}_{n-1} - \dot{x}_n) - k_r(x_n - x_{n+1}) \\
 & \quad -d_r(\dot{x}_n - \dot{x}_{n+1}) - W_n - 0.5\rho_w C_d \dot{x}_n|\dot{x}_n|A_r - F_{mud\_drag}/N \\
 & \vdots \\
 & \vdots \\
m_{LMRP}\ddot{x}_{LMRP} & = k_r(x_{LMRP} - x_1) + d_r(\dot{x}_{LMRP} - \dot{x}_1) - k_{LMRP}x_{LMRP} - W_{LMRP} \\
 & \quad -0.5\rho_w C_{d_{LMRP}} \dot{x}_{LMRP}|\dot{x}_{LMRP}|A_{LMRP} - F_{mud\_drag}/N - F_{thrust} \\
m_{mud}\ddot{x}_{mud} & = \rho_w A_i L_{riser} + F_{mud\_drag} + F_{thrust} - \rho_{mud} A_r (L_{riser} - x_{mud})
\end{cases}
\tag{4.1}
$$

Suppose that the riser is divided into N sections. x_{TR}, x_n and x_{LMRP} are the position of the tension ring, riser node n and the LMRP. x_{mud} is the mud discharge distance, which travels in the opposite direction of the x_{TR}, x_n and x_{LMRP}. F_{ET} and F_{HT} are the wire-line tensions provided by each electrical and hydro-pneumatic tensioners, and N_{ET} and N_{HT} are the number of electrical and hydro-pneumatic tensioners respectively. k_r and d_r are marine riser material stiffness and dampening. m_{TR} and W_{TR} are the mass and the weight of the tension ring plus the last node of riser pipe. m_n and W_n are the mass and the wet weight of the riser node n ($1 \leq n \leq N$). C_d is the drag coefficient along the vertical axis of the riser, and C_{d_LMRP} is the drag coefficient of the LMRP. ρ_w is seawater density, A_r is the area of a buoyant riser joint. L_{riser} is the length of riser pipe.

k_{LMRP}, the connection stiffness of the LMRP, changes from the value of riser stiffness k_r to zero at the moment of disconnect, $t = 0^+$, which provides the initial condition of tension applied on LMRP before the disconnect.

Immediately after the LMRP is disconnected from the BOP, the drilling mud column is no longer supported and effectively collapses, leading to a flow of drilling mud out of the riser. This flow will continue until the mud column reaches hydrostatic equilibrium with the ocean, or until the drilling mud is completely evacuated from the riser and the riser is seawater filled. The behavior of the column of drilling mud in the riser is one of the major factors that affect the

recoil response of the riser. Hence, the mud column modeling is included in the process plant model. As the drilling mud flows out of the riser, it imparts:

(1) a drag loading along the riser which acts to counteract to the upward movement of the riser;

(2) a thrust force to the bottom of the riser which accelerates the upward movement of the riser.

F_{mud_drag} is the mud drag force applied on the riser node and the LMRP due to the mud flow friction.

$$F_{mud\_drag} = \rho_{mud} f (L_{riser} - x_{mud}) \dot{x}_{mud} |\dot{x}_{mud}| A_r / d_r \tag{4.2}$$

where f is the friction factor between the mud and riser internal tube, d_r is the diameter of the riser joint.

F_{thrust} is the thrust force applied at the LMRP, the bottom of the riser, caused by the mud discharge.

$$F_{thrust} = 0.5 \rho_{mud} \dot{x}_{mud} |\dot{x}_{mud}| A_r \tag{4.3}$$

where ρ_{mud} is the mud density.

4.2.3. Electrical Tensioner Model

An electrical winch driven by a permanent magnet synchronous motor drive (PMSM) is considered to be the main component of the electrical tensioner. This is the same for the active heave compensation design.

The system model of a PMSM in the rotor rotating reference frame is repeated as follows:

$$\begin{cases} v_q = R_E i_q + \dot{\lambda}_q + \omega_s \lambda_d \\ v_d = R_E i_d + \dot{\lambda}_d - \omega_s \lambda_q \end{cases} \tag{4.4}$$

where $\lambda_q = L_q i_q$, $\lambda_d = L_d i_d + L_{md} i_{fd}$ and $\omega_s = P\omega_r$. v_d, v_q are the d, q axis stator voltages and i_d, i_q are the d, q axis stator current. L_d and L_q are the d, q axis stator flux linkage, R_E is the stator resistance, ω_s is the motor electrical frequency, ω_r is the rotor speed, i_{fd} is the equivalent d-axis magnetizing current, L_{md} is the d-axis mutual inductance, P is the number of pole pairs.

The tension force delivered by the electrical tensioner can be expressed:

$$F_{ET} = \frac{3}{2r_{winch}} P\left[L_{md} i_{fd} i_q + \left(L_d - L_q\right) i_d i_q\right] - \frac{b}{{r_{winch}}^2} \dot{x}_{ET} \tag{4.5}$$

where x_{ET} is the line displacement of the wire on the electrical tensioner, b represents the dampening coefficient of the electrical system and r_{winch} is the radius of the winch drum.

A wire rope tension force F_{L_ET} is applied on the electrical winch due to elongation of a wire. This is the counter force to the force delivered by the electrical tensioner F_{ET}.

$$F_{L\_ET} = \begin{cases} k_w\left(x_{ET} - x_{ship} - x_{TR}\right) + d_w\left(\dot{x}_{ET} - \dot{x}_{ship} - \dot{x}_{TR}\right) & when\ \left(x_{ET} - x_{ship}\right) \geq x_{TR} \\ 0 & when\ \left(x_{ET} - x_{ship}\right) < x_{TR} \end{cases} \tag{4.6}$$

The same electrical tensioner model for the active heave compensation control design in Chapter 3 is used in this process model.

The electrical tensioner system model can be rewritten as:

$$\begin{cases} \frac{J_{eff}}{{r_{winch}}^2} \ddot{x}_{ET} = \frac{3PL_{md}I_{fd}}{2r_{winch}} i_q - \frac{b}{{r_{winch}}^2} \dot{x}_{ET} - F_{L\_ET}/cos\theta \\ L_q \dot{i_q} = v_q - R_E i_q - \frac{L_{md} I_{fd} P}{r_{winch}} \dot{x}_{ET} \end{cases} \tag{4.7}$$

It is worth to mention that the time constant in the electrical system is significantly faster than that of the mechanical system. Therefore, any dynamic change of tension required by the mechanical system can be satisfied easily by the controlled electrical system. The control design in the next section can be facilitated, relying on this advantage.

4.2.4. Hydro-pneumatic Tensioner Model

The tensioner cylinder and associated hydraulic and pneumatic components are shown in Fig. 4.2. The tension force F_{HT} indicates the tension force delivered by the hydro-pneumatic tensioner. In case of the wire-line tensioner, this tension force F_{HT} is one fourth of the compression force F_p applied on the piston rod in the downward compression direction, depending on the number of sheaves. The same force F_{HT} is applied at the bottom of the cylinder in the downward expansion direction for the N-line tensioner.

The cylinder divides its housing into a high pressure hydraulic chamber and a low pressure gas chamber. The force F_p is developed by means of the pressure difference between the high pressure and low pressure chambers applied on the cylinder piston rod.

Hydraulic fluid in the high pressure hydraulic chamber is maintained under pressure by a hydraulic/pneumatic accumulator, which includes a floating piston separating hydraulic fluid in the bottom half of accumulator from the compressed air in the top half of the accumulator. Since the hydraulic fluid is not compressible, compared to gas, the volume change of the hydraulic fluid is not considered in this study.

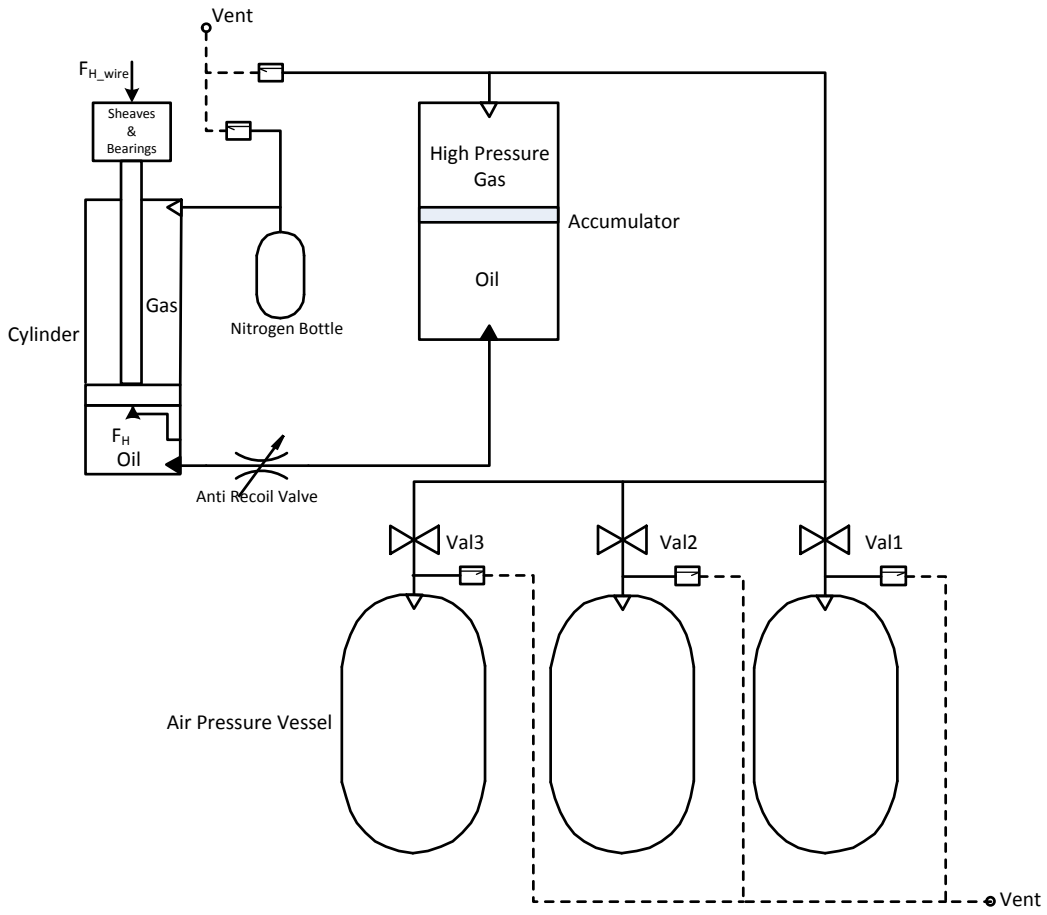

Fig. 4.2 Simplified Layout of Hydro-pneumatic Tensioning System

The top half of the accumulator is connected through a pneumatic pressure line to a high pressure gas bank used to maintain a preset high pressure level in the accumulator. As shown in Fig. 4.2, the number of online air pressure vessel (APV) can be controlled by the valves, Val_1, Val_2, Val_3. The high air pressure P_h of the accumulator and the APVs varies with the air volume, which changes by the position of the cylinder piston rod, as shown in the equation (4.8).

$$P_h = P_{h,0}\left(\frac{V_{h,0}}{V_{h,0} + A_{hc}(x_p - x_{p0} - x_{ship})}\right)^{\eta} \tag{4.8}$$

where the $P_{h,0}$ indicates the initial high pressure of the high pressure APVs. The x_{ship} is the vessel heave motion relative to the seabed coordinate frame. The constant η is the polytrophic

constant for practical air compression and expansion process. The $V_{h,0}$ represents the initial air volume in the APVs, the accumulators and the air pipe.

$$V_{h,0} = V_{APV}N_{APV} + A_{pipe}l_{pipe} + V_{acc}N_{acc}(1 - r_{acc}) \tag{4.9}$$

where r_{acc} represents the fluid fullness ratio of the accumulator with respect to air.

Because the piping connecting the working APVs and accumulators is usually long (more than 30m), the pressure drop due to the imposed flow restrictions ΔP_{pipe} is considered in this model, as shown in equation (4.10):

$$\Delta P_{pipe} = \frac{f_{air}\rho_{air}\dot{x}_p^2 l_{pipe}}{2d_{pipe}} \tag{4.10}$$

where f_{air} is the coefficient of air friction in pipe, ρ_{air} is the air density, d_{pipe} is the inner diameter of the air pipe.

The friction force due to the hydraulic fluid flow in the pipe connecting the accumulator and the cylinder, is also taken into consideration here. The pressure drop ΔP_{fluid} is represented in equation (4.11):

$$\Delta P_{fluid} = \frac{8f_{fluid}\rho_{fluid}l_{fluid}Q_{fluid}|Q_{fluid}|}{\pi^2 g d_{fluid}^5} \tag{4.11}$$

where ρ_{fluid} is the fluid density, d_{fluid} is the inner diameter of the fluid line.

Q_{fluid} is the flow rate into and out of the cylinder, $Q_{fluid} = A_{hc}\dot{x}_p$, where A_{hc} is the area of the high pressure side tensioner cylinder.

f_{fluid} is the coefficient of fluid friction, which changes with the fluid flow rate. The formula is developed based on the Darcy–Weisbach equation.

$$f_{fluid} = \begin{cases} \dfrac{0.25}{log_{10}\left(\dfrac{\varepsilon}{3.7d_{fluid}} + \dfrac{5.74}{5000^{0.9}}\right)} & when\ Re < 5000 \\ \dfrac{0.25}{log_{10}\left(\dfrac{\varepsilon}{3.7d_{fluid}} + \dfrac{5.74}{Re^{0.9}}\right)} & when\ 5000 \le Re \le 10^9 \\ \dfrac{0.25}{log_{10}\left(\dfrac{\varepsilon}{3.7d_{fluid}} + \dfrac{5.74}{10^{9^{0.9}}}\right)} & when\ Re > 10^9 \end{cases} \tag{4.12}$$

where ε here represents the material roughness height, $0.6 \times 10^{-3}\, m$. Re is the Reynold Number, $Re = \frac{\rho_{fluid} v_{fluid} d_{fluid}}{\mu_{fluid}}$ with μ_{fluid} to be the fluid dynamic viscosity, $0.9 \times 10^{-3}\, Pa \cdot s$.

Once the system is switched to the disconnect mode, the solenoid is energized to send the pilot pressure to the main control valve and the main control valve can control the position of the main Olmsted valve to close at a certain rate. The main Olmsted valve can be modeled as a variable throttle valve, to be controlled by a control structure to be elaborated as follow:

$$\Delta P_{olm} = \begin{cases} SG \dfrac{Q_{fluid}|Q_{fluid}|}{C_V(y)^2} & when\ activated \\ 0 & when\ not\ activated \end{cases} \tag{4.13}$$

where SG is the specific gravity of the tensioner hydraulic fluid, $SG = \frac{\rho_{fluid}}{\rho_{water}}$.

$C_V(y)$ is the flow coefficient of the Olmsted valve, as a function of valve closure and stroke position. It describes the relationship between the pressure drop across the valve orifice and the corresponding flow rate. y represents the cylinder piston stroke position, $y = x_p - x_{p0} - x_{ship}$. The value of this C_V is usually provided by the Olmsted valve manufacture, as a function of Olmsted valve closure, as shown in Fig. 4.3.

Furthermore, the anti-recoil control algorithm in this model sets the valve closure position to be in a pre-set non-linear relationship with the cylinder piston stroke. Fig. 4.4 shows an example characteristic curve.

To sum all the pressure drops along the load path, we get the pressure acting on the high pressure side of the riser tensioner piston rod to be:

$$P_{hc} = P_h - \Delta P_{pipe} - \Delta P_{fluid} - \Delta P_{olm} \tag{4.14}$$

The low pressure gas chamber keeps gas pressure around atmosphere pressure, as shown in the equation (4.15):

$$P_{lc} = P_{l,0}\left(\frac{V_{l,0}}{V_{l,0} - A_{lc}(x_p - x_{p0} - x_{ship})}\right)^{\eta} \tag{4.15}$$

The main force applied on the tensioner cylinder due to the hydraulic and pneumatic pressure can be written as:

$$F_p = A_{hc}P_{hc} - A_{lc}P_{lc} \tag{4.16}$$

Other associated forces are captured in this model. The hydrodynamic friction force is captured in this model. This is a velocity dependent part of the friction force:

$$F_{fr} = F_{seal}tanh[k_v(\dot{x}_p - \dot{x}_{ship})] \tag{4.17}$$

where F_{seal} is the static seal friction force between the piston rod and the cylinder inner wall, k_v is the friction factor and $(\dot{x}_p - \dot{x}_{ship})$ represents the piston velocity with respect to the ship position.

The impact force F_{impact} of the piston rod is zero when the rod travels in the cylinder and doesn't hit both ends, but increases dramatically after the piston reaches the stroke limit.

$$F_{impact} = \begin{cases} 10^7(x_p - x_{p0} + S_{init} - S_{limit}) & when\ (x_p - x_{p0} + S_{init}) \geq S_{limit} \\ 0 & when\ 0 < (x_p - x_{p0} + S_{init}) < S_{limit} \\ 10^7(x_p - x_{p0} + S_{init}) & when\ (x_p - x_{p0} + S_{init}) \leq 0 \end{cases} \tag{4.18}$$

where S_{init} is the initial stroke of the piston before simulation, S_{limit} is the maximum length of stroke. The position of the piston varies from 0 to S_{limit}.

The counter force to the pressure force of the cylinder, the wire rope tension force applied on the piston rod due to elongation of a wire is given by the equation (4.19):

$$F_{L\_HT} = \begin{cases} k_w\left(R_{td}x_p - x_{ship} - x_{TR}\right) + d_w\left(R_{td}\dot{x}_p - \dot{x}_{ship} - \dot{x}_{TR}\right) & when\ \left(R_{td}x_p - x_{ship}\right) \geq x_{TR} \\ 0 & when\ \left(R_{td}x_p - x_{ship}\right) < x_{TR} \end{cases} \quad (4.19)$$

where R_{td} is the turn down ratio of the number of wire ropes on tensioner. k_w and d_w are wire rope material stiffness and dampening. Because the wire line works only in tension, it is assumed that the tension exists only when the elongation is positive.

The dynamic equation governing the tensioner cylinder motion x_p is as follow:

$$m_p\ddot{x}_p = F_p - R_{td}F_{L\_HT}/cos\theta - W_p - F_{impact} - F_{fr} \quad (4.20)$$

where W_p is the weight of the moving piston.

The wire-line tension delivered by the hydro-pneumatic tensioner F_{HT} is:

$$F_{HT} = F_p/R_{td} \quad (4.21)$$

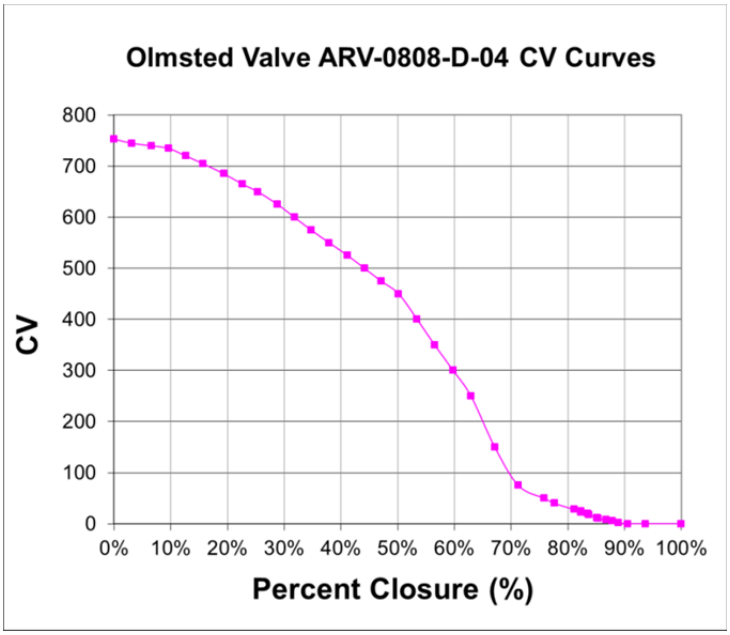

Fig. 4.3 Olmsted valve C_V as a function of valve closure

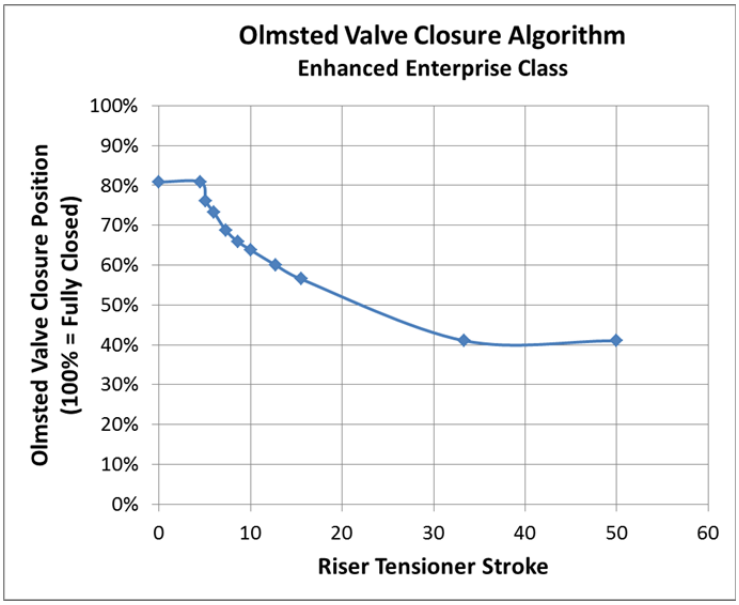

Fig. 4.4 Example Olmsted Valve closure algorithm

4.2.5. Modification for the Control Plant Model

4.2.5.1. Keep near constant tension on hydro-pneumatic tensioners

Since the dynamically controlled motors of the electrical tensioners are fully capable to reduce their delivered tensions instantaneously, so that the total tension applied on the tension ring is fully controllable and predictable, even though the tension delivered by the hydro-pneumatic tensioners is not capable to meet the required rate of change. With this new system characteristic, the anti-recoil equipment installed in the hydro-pneumatic tensioners can be kept open during riser recoil process. In this way, the hydro-pneumatic tensioners are running as a passive heave compensation device. This makes the whole anti-recoil process much more testable and predictable.

For riser parting incident, the riser string breaks in the middle. The up-part of riser accelerates fast due to the big over-pulling tensions before breakage. A big step change of tension is required immediately, to avoid the riser to from hitting the drill floor. Even the electrical tensioners stop delivering any tension immediately; the other hydro-pneumatic ones are

still delivering approximately the same amount of tensions, which should be alleviated as fast as possible. In this scenario, the anti-recoil valves of the hydro-pneumatic tensioners should be activated to reduce their delivered tension.

The tension change of the hydro-pneumatic tensioners should be activated only in the following two AND conditions, when the riser is moving up:

(1) the wire tensions measured on the electrical tensioners almost reaches their minimum limit: $F_{ET} = F_{ET\_min}$

(2) two OR conditions:

a) The riser top is still accelerating at the moment of measurement: $a_{TR} > 0$;

b) The remaining predicted displacement of the riser top exceeds the maximum cylinder stroke: $x_{TR} + \frac{1}{2}\frac{v_{TR}^2}{a_{TR}} > x_{TR\_max}$

After the riser reaching the highest point, it is possible that the riser is not stabilized at the preset height; if the whole tensioning system is under-damped. The riser starts to fall down. In this case, the tension change of the hydro-pneumatic tensioners should also be activated, in the following two AND conditions, when the riser is falling down:

(1) the wire tensions measured on the electrical tensioners almost reaches their maximum limit: $F_{ET} = F_{ET\_max}$

(2) two OR conditions:

a) The riser top is still decelerate at the moment of measurement: $a_{TR} < 0$;

b) The remaining predicted displacement of the riser top exceeds the maximum cylinder stroke: $x_{TR} + \frac{1}{2}\frac{v_{TR}^2}{a_{TR}} < x_{TR\_min}$

4.2.5.2. The simplification of the mud column and the water drag force model

The mud column has been modeled as a slug load in the process plant model in preparation for validation of our control design performance: (1) the shedding loads from the mud column are applied in each riser node model. (2) and the thrust force is also applied on the LMRP at the bottom of riser.

However, from both the process plant simulation and empirical study, we find that the peak mud drag force due to the friction F_{mud_drag} is less than $1/500$ of the tensioner pulling tension, and the mud thrust force F_{thrust} applied on the LMRP is only $1/5000$ of the tensioner pulling tension, as shown in Fig. 4.5. They are not dominant effects in the system. Hence, they are neglected in the following control plant model.

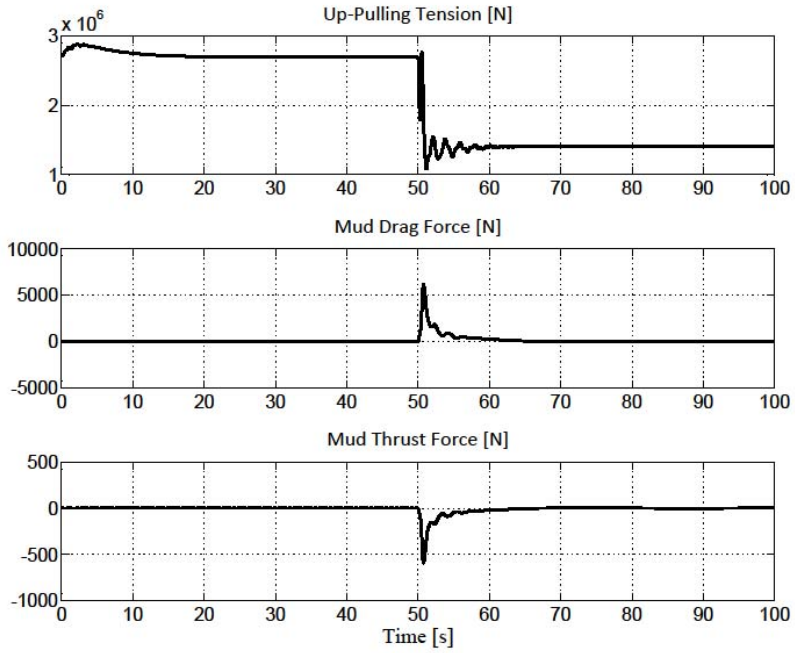

Fig. 4.5 Example Comparison of the Up-Pulling Tension, Mud Drag Force and Mud Thrust Force

The water drag force is also neglected in the control plant, since it is also considerably smaller than the riser weight and the up-pulling tension at the top.

But these effects are all included back into the numerical simulation in the section 4.4, so that the feedback control gain is tuned again based on the sum of the linear tension from the top and the non-linear auxiliary forces mentioned above.

Now the control plant model becomes a linear state space model, as shown in equation (4.22).

$$\begin{bmatrix} \dot{v}_{TR} \\ \dot{x}_{TR} \\ \dot{v}_{N-1} \\ \dot{x}_{N-1} \\ \vdots \\ \vdots \\ \dot{v}_n \\ \dot{x}_n \\ \vdots \\ \vdots \\ \dot{v}_2 \\ \dot{x}_2 \\ \dot{v}_{LMRP} \\ \dot{x}_{LMRP} \end{bmatrix} = \begin{bmatrix} -\frac{d_r}{\varphi_{TR}} & -\frac{k_r}{\varphi_{TR}} & \frac{d_r}{\varphi_{TR}} & \frac{k_r}{\varphi_{TR}} & & & & & & & & & & \\ 1 & 0 & 0 & 0 & & & & & & & & & & \\ & & & & \ddots & & & & & & & & & \\ & & & & & \frac{d_r}{m_n} & \frac{k_r}{m_n} & -\frac{2d_r}{m_n} & -\frac{2k_r}{m_n} & \frac{d_r}{m_n} & \frac{k_r}{m_n} & & & \\ & & & & & 0 & 0 & 1 & 0 & 0 & 0 & & & \\ & & & & & & \vdots & & & & & \ddots & & \\ & & & & & & & & & & & \frac{d_r}{m_{LMRP}} & \frac{k_r}{m_{LMRP}} & -\frac{d_r}{m_{LMRP}} & -\frac{k_r+k_{LMRP}}{m_{LMRP}} \\ & & & & & & & & & & & 0 & 0 & 1 & 0 \end{bmatrix} \begin{bmatrix} v_{TR} \\ x_{TR} \\ v_{N-1} \\ x_{N-1} \\ \vdots \\ \vdots \\ v_n \\ x_n \\ \vdots \\ \vdots \\ v_2 \\ x_2 \\ v_{LMRP} \\ x_{LMRP} \end{bmatrix} + \begin{bmatrix} -\frac{F_{ET}N_{ET}+F_{HT}N_{HT}}{\varphi_{TR}} \\ 0 \\ 0 \\ 0 \\ \vdots \\ \vdots \\ 0 \\ 0 \\ \vdots \\ \vdots \\ 0 \\ 0 \\ 0 \\ 0 \end{bmatrix}$$

$$\begin{bmatrix} v_{TR} \\ x_{TR} \end{bmatrix} = \begin{bmatrix} 1 & 0 & 0 & \dots & \dots & 0 \\ 0 & 1 & 0 & \dots & \dots & 0 \end{bmatrix} \begin{bmatrix} v_{TR} \\ x_{TR} \\ v_{N-1} \\ x_{N-1} \\ \vdots \\ \vdots \\ v_n \\ x_n \\ \vdots \\ \vdots \\ v_2 \\ x_2 \\ v_{LMRP} \\ x_{LMRP} \end{bmatrix} \tag{4.22}$$

With

$\varphi_{TR} = m_{TR} + N_{HT}m_p + N_{ET}J_{winch}/r_{winch}^2$.

4.3. Control Design

4.3.1. Literature Review of Available Control Strategies

The electrical motor based electrical tensioner provides faster and more flexible control solution for the anti-recoil operation. The fundamental control goal of the riser anti-recoil is, in fact, to control the position of the riser. The whole riser string should be brought upward to a certain height within a certain velocity profile. Based on this concept, a position control strategy is proposed with the control objective of moving the riser body to a desired elevation in a predictive manner.

The most essential characteristic requirement for this anti-recoil system is to maneuver large inertia. If the lifting tensions don't decrease in a predictive manner before reaching the target position, the riser would easily overshoot and hit any equipment in the load path from the telescopic joint to the drill floor.

One and also the only similar application of high inertia load on marine vessel is the drawworks, which is designed to handle more than 1200 metric tons of loads nowadays. The only literature available to public discussing the position control of the drawworks is by H. Zinkgraf, D. O'Brien, et al [54]. This paper examined general design requirements for achieving automatic positioning of the drawworks traveling block. The system provided closed-loop braking control while monitoring the traveling block position. The control loop was designed using the velocity feedback, and a math model was running as background to calculate the predicted position. Various parameters were constantly monitored to prevent moving the traveling block to collide with pipe handling equipment above the traveling block. However, this paper, which was published 20 years ago, relied on the velocity control on the software side, the mechanical disk brake and the eddy current brake system on the hardware side. Current technology uses mainly four-quadrant motor drive to decelerate the traveling block. The kinetic energy is regenerated to electrical power, then either transferred to energy storage units or burnt into heat to the braking resistors.

The current drawworks designed by National Oil Varco still uses motor speed feedback control with a slow rate of change ramping function to prevent overshot of the heavy load of high speed [55] - [58]. A controlled stop with speed ramp down of machines is executed before any mechanical brakes are applied. Several levels of safety distances are set in the control logic based on the calculated remaining stop length. The anti-recoil control to which we are aiming, is more similar to an inertial control system. No publication in such position control algorithm design is specialized in the oil/gas area.

However, the position control of electrical motor has been widely used in many other applications, such as robot industry, mining industry. E. Bizzi and N. Hogan [60] discussed rapid movements of robot arm are generated by a pulsatile contraction force and slower ramp movements. Reflecting this analysis to the riser tensioning system application, the pulsatile force can be understood as the acceleration force which pushes the big inertia up to speed. And the slower ramp force brings this load to the new end position smoothly. W. Wang et al [61] discussed the position control of a flexible arm by using an output feedback controller with a shaft encoder. A modified PID feedback loop was used to control the position in this paper. R. Cannon and E. Schmitz [62] developed a control algorithm using LQG approach and a good tip control response was achieved with a good dynamic model. All these position control strategies sets a good starting point for the control design of the riser hybrid tensioning system.

4.3.2. The Goal of Predictability and Testability Improvement

This riser hybrid tensioning system aims to make the riser system more testable. The lifting displacement of the LMRP can be set as an adjustable parameter in the control firmware, which can be easily changed to fit a particular test. For example, instead of lifting the riser the full retraction of 30 ft., it can be lift only $1/3$ of the full retraction. This functionality allows us to perform any maintenance tests more frequently. More importantly, it highly reduces the risk of damage. This anti-recoil control strategy becomes much more predictable, and can be

performed as a routine maintenance procedure, and brings back operator's confidence, which is reduced exponentially by time since the last test.

The dynamically controlled electrical tensioners aim to increase the predictability of the riser anti-recoil system. The anti-recoil equipment installed in the hydro-pneumatic tensioners could be kept open during the riser recoil process, to avoid the unpredictability of complicated hydraulic valve system. The tension in electrical tensioners should be increased to its maximum value, so that it lifts the LMRP from BOP fast and straight to avoid any collision or damage. Then the tension is reduced rapidly to avoid hitting the rig floor. Before the riser reaching the target height, the electrical tensioners should reversely increase tension very slowly to lift the weight of the riser to the target position gradually. On the other hand, the hydro-pneumatic tensioners are not able to reverse the rate of change of tension easily within short time span.

The electrical tensioner could still be under position control mode, during the normal operation of active heave compensation when the riser bottom is connected to the sea bed. The target displacement of the riser top can be set to lift 5 feet, by simply typing the value into computer. The lower maximum tension limit of the electrical tensioners is set to the nominal tension calculated by riser engineers. In this way, the position control error is always saturated and the electrical tensioners always output the maximum tension limit, i.e., the nominal required tension, and the whole riser string keeps under constant tension during this operation mode. This operation method will significantly increase the vessel predictability. Especially for the unplanned riser parting incident, the riser top position will be safely lifted by a certain distance, instead of any overshot due to the lighter weight of the broken riser string.

4.3.3. Position Control Design

Several boundary conditions are set :

(1) the riser bottom needs to be lifted rapidly to separate the approximation of the LMRP and the BOP in order to avoid any kind of vertical or horizontal collision of the overlap section.

(2) the overshot of the riser top from the target position should be predicted and limited by varying the tension of the electrical tensioners, to prevent the telescopic joint and other items in the load path from damage, such as the drill floor.

(3) each wire rope of the tensioner needs to be under tension all the time, in order to avoid any slack which may cause the wire rope to jump off one of their sheaves and also may cause shock load on the rope and the tensioners.

According to above conditions, a position control strategy is proposed. The target displacement reference can be set as the position of the tension ring x_{TR_ref}. Several PID based position control schemes have been investigated at first using simulation, such as the schemes shown in Fig. 4.6.

However, we found that simple PID loop is not satisfactory in this application. The proportional and integral gains become very sensitive and difficult for tuning, because of the large inertia, and the large amount of kinetic energy stored in such long and heavy riser string. Therefore, we seek for other optimal control strategy.

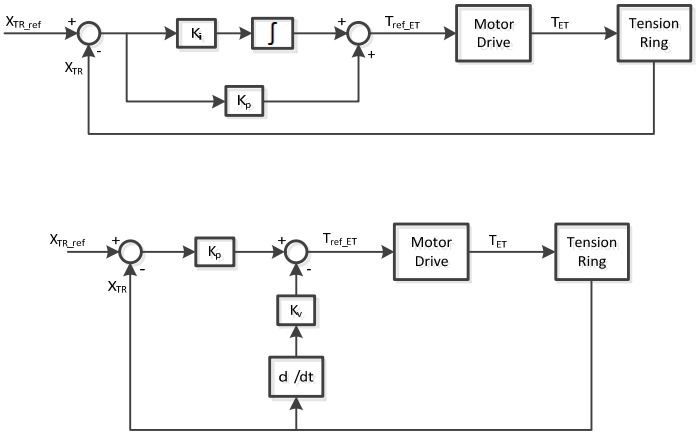

Fig. 4.6 Attempted PID Position Control Schemes

A model prediction control (MPC) method, previously used in chemical process and oil refinery industry, overcomes the above difficulties for PID controller. It aims to predict the future control input to make the future system response well behaved following the desired reference command for a specific time length N of moving horizon. This method starts to be applied in other industry nowadays. Graichen [106] developed a MPC control strategy for the laboratory crane application. Van den Broeck [107] developed a Time Optimal MPC and is validated using a linear motor drive and an overhead crane. Graichen [108] reformulated the problem of the MPC scheme into an unconstrained counterpart and solve with a fast MPC algorithm. However, a drawback of MPC is the considerable computational effort that is required to solve the constrained optimal control problem. This typically limits the use of MPC to slow or low dimensional systems. Therefore, we tried to investigate the Linear-Quadratic Regulator (LQR) with the Kalman state variable estimator for the first trial.

A LQG controller, as an optimal control design technique, produces a linear dynamic feedback control law that is easy to compute and implement in industrial hardware. It gives a simple and more stable solution to control the kinetic energy of riser. The LQR control method also provides the flexibility to control the position of any node location along the riser string from top to bottom.

The target reference for the final state variables of the overall control system can be set as the desired positions and velocities of the riser top, riser bottom and each node chosen along the riser pipe, i.e. $[v_{TR} \quad x_{TR} \quad v_{N-1} \quad x_{N-1} \quad \cdots \quad v_{LMRP} \quad x_{LMRP}]^T$. The control input of the system is the motor q-axis stator voltage v_q.

An estimator of the riser string dynamic motion is built using Kalman Filter. The combination of this Kalman estimator and the LQR combined Linear-Quadratic Guassian (LQG) controller topology is shown in Fig. 4.7. The LQG controller, as a fundamental optimal control design technique, has the advantage of good disturbance attenuation and robust performance. Therefore, the heave motion or other disturbance should not affect the position of the riser using this control design method.

The design problem of the optimal controller is to determine the optimal control input $\tilde{u}(t) = v_q(t)$ which minimizes a cost function:

$$J = \int_0^\infty \left(\tilde{x}(t)^T Q \tilde{x}(t) + \tilde{u}(t)^T R \tilde{u}(t)\right) dt \tag{4.23}$$

The value of matrix Q and R, as constant weighting matrices, are selected and determined respectively, by the "trial and error method". Q is a diagonal matrix of the size of the $\tilde{x}(t)$ with $Q(1,1) = 2 \times 10^6$, $Q(2,2) = 2 \times 10^5$, which are the weight of the state variables representing the riser top node velocity and position. And $R = 1 \times 10^{-5}$, which represents the weighting factor of the electrical tensioner input.

The optimal control law which minimizes the equation (4.23) for any initial state is given by [63]:

$$\tilde{u}(t) = -K_r \tilde{x}(t) \tag{4.24}$$

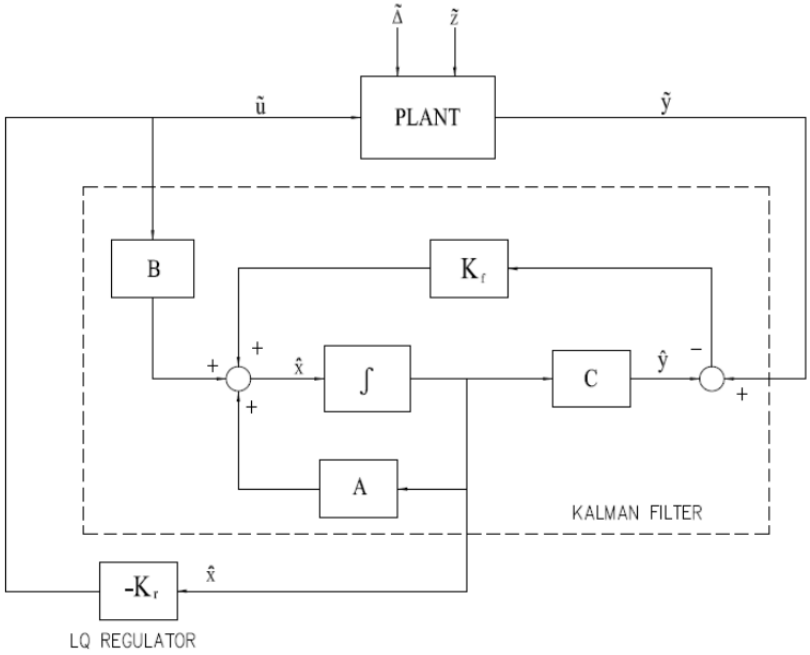

Fig. 4.7 The LQR Controller with Kalman Filter

And the feedback matrix is

$$K_r = R^{-1}B^T X \tag{4.25}$$

where $X = X^T \geq 0$ is the unique solution of the algebraic Riccati equation $A^T X + XA - XBR^{-1}B^T X + Q = 0$.

Since the state space variables are not directly accessible, a Kalman filter is constructed to find an optimal estimate $\hat{x}$ of the state $\tilde{x}$ from the system output $\tilde{y}$. The required solution to the LQR problem is then found by replacing $\tilde{x}$ by $\hat{x}$. The observer can be described as:

$$\dot{\hat{x}} = A\hat{x} + B\tilde{u} + K_f(\tilde{y} - C\hat{x}) \tag{4.26}$$

Also by "trial and error method," the W and V are chosen to be: $W = 1$ and

$$V = \begin{bmatrix} 1 \times 10^{-12} & \\ & 1 \times 10^{-11} \end{bmatrix}$$

The optimal choice of K_f is given by:

$$K_f = YC^T V^{-1} \tag{4.27}$$

where $Y = Y^T \geq 0$ is the unique solution of the algebraic Riccati equation $YA^T + AY - YC^T V^{-1} CY + W = 0$.

4.4. Simulation Results

4.4.1. Set Up

A closed-loop system simulation has been carried out using Matlab Simulink to demonstrate the performance of the proposed controller and the estimator.

The dynamic behavior of riser string is simulated using the model developed in equation (4.1), including all the water drag force, mud drag and mud shedding effect. The vessel heave is simulated using a sinusoidal waveform of the worst case scenario (the amplitude of $2m$ and the period of $5s$).

The model implemented in Simulink runs at $1000\ m$ water depth, with five nodes $N = 5$ for 1000 meter riser string, which gives the element length of 200m. In order to limit the computation time for real-time control applications, it is of interest to minimize the number of elements applied in the riser model, while still maintaining a sufficient level of accuracy, such that the implemented model can represent the geometry of the real world.

The hydro-pneumatic tensioners are modeled as a passive heave compensator using equation (4.8) - (4.21). A big impact force is applied when the piston rod hits both ends. The anti-recoil valve is activated, only when the tension delivered by the electrical tensioner reaches the minimum setting, following the criterions described in the section 4.2.5. Little tension variation caused by the heave motion should be experienced before and after riser recoil.

The detailed numerical data adapted in this simulation are collected from the new built drilling rig Deepwater Thalassa, and shown below:

Table 4.1: Detailed Numerical Simulation Values of the Riser

Parameter	*Description*	*Value*	*Unit*
k_r	Riser Stiffness	2.54×10^8	N/m
k_{LMRP}	Connection Stiffness of the LMRP	2.54×10^8	$N.s/m$
d_r	Riser Damping Coefficient	5.1×10^5	$N.s/m$
m_{TR}	Mass of Tension Ring and the Nth Node of Riser	5.45×10^4	kg
W_{TR}	Weight of Tension Ring and the Nth Node of Riser	5.34×10^5	N
m_n	Mass of the nth Node of Riser	2.41×10^5	kg
W_n	Wet Weight of the nth Node of Riser	3.17×10^5	N
m_{LMRP}	Mass of LMRP and the 1st Node of Riser	3.76×10^5	kg
W_{LMRP}	Wet Weight of LMRP and the 1st Node of Riser	1.41×10^6	N
ρ_w	Seawater Density	1000	kg/m^3
ρ_{mud}	Mud Density	1025	kg/m^3
C_d	Drag Force Coefficient of Sea Water	0.1	
C_{d_LMRP}	Drag Coefficient of LMRP	2	
A_r	Riser Cross Sectional Area	0.0357	m^2
A_{LMRP}	Surface Area of LMRP	27.9	m^2
A_i	Inner Area of Riser	0.198	m^2
L_{riser}	Length of Riser Pipe	1000	m
f	Friction Factor between Mud and Riser	0.08	

Table 4.2: Detailed Numerical Simulation Values of the Hydro-pneumatic Tensioner

Parameter	*Description*	*Value*	*Unit*
N_{ET}	Number of Electrical Tensioners	8	
N_{ET}	Number of Hydro-pneumatic Tensioners	8	
A_{hc}	Area of High Pressure Side of Cylinder	0.23	m^2
A_{lc}	Area of Low Pressure Side of Cylinder	0.15	m^2
A_{pipe}	Inner Area of Air Pipe	0.0035	m^2
V_{APV}	Volume of each APV	2.35	m^3
V_{acc}	Volume of each Accumulator	1.05	m^3
l_{pipe}	Length of Air Pipe	30	m
d_{pipe}	Inner Diameter of Air Pipe	0.13	m^2
N_{APV}	Number of APVs	2	
N_{acc}	Number of Accumulators	1	
r_{cc}	Fluid Fullness Ratio of the Accumulator	0.98	
f_{fluid}	Friction Factor of Hydraulic Fluid	0.0385	
ρ_{fluid}	Density of Hydraulic Fluid	1025.16	kg/m^3
d_{fluid}	Inner Diameter of Fluid Line	0.125	m
μ_{fluid}	Dynamic Viscosity of Hydraulic Fluid	0.9×10^{-3}	$Pa \cdot s$
SG	Special Gravity of Tensioner Hydraulic Fluid	1.025	
F_{seal}	Static Seal Friction Between Piston and Cylinder	22685.9	N
k_v	Friction Factor Between Piston and Cylinder	0.01	
R_{td}	Return Down Ratio of the Number of Wires	4	
k_w	Wire Rope Material Stiffness	4.06×10^6	N/m
d_w	Wire Rope Damping Coefficient	1617.5	$N.s/m$
m_p	Mass of Moving Piston Rod	8643.6	kg
W_p	Weight of Moving Piston Rod	84707.4	N

Table 4.3: Detailed Numerical Simulation Values of the Electrical Tensioner

Parameter	*Description*	*Value*	*Unit*
J_{eff}	Effective Moment of Inertia of All Moving Part	1580	$kg.m^2$
r_{winch}	Radius of Winch Drum	0.62	m
b	Damping Coefficient	200	$N.m.s$
L_q	q-Axis Stator Flux Linkage	12.66×10^{-3}	H
L_{md}	d-Axis Stator Mutual Inductance	0.2	H
i_{fd}	Equivalent d-Axis Magnetizing Current	167	A
R_E	Stator Resistance	0.2159	kg
P	Number of Pole Pairs	15	
GR	Gear Ratio	10.5	

4.4.2. Control Design Configuration

The simulated initial conditions of the state variables before riser disconnect is listed below:

$$[v_{TR} \quad x_{TR} \quad v_{N-1} \quad x_{N-1} \quad \dots \quad v_{LMRP} \quad x_{LMRP}]^T_{initial}$$

$$= [0 \quad 0.18 \quad 0 \quad 0.14 \quad 0 \quad 0.09 \quad 0 \quad 0.45 \quad 0 \quad 0]^T$$

The initial values of the node positions are not zero. This is because that the applied tension pulls and stretches the riser string of 1000m to elongate.

The initial total up-pulling force applied on the tension ring is $4200\,kN$ s. The total stroke of the hydro-pneumatic tensioner cylinder is $7.62\,m$. The initial stroke position of the hydro-pneumatic tensioner cylinder piston moves with the heave motion at the center of $1.61\,m$ from the dead end of oil side.

The LQG controller is designed by using the Maltab Control System Toolbox, based on the control plant model of equation (4.22). Numerical values of the LQR controller K_r and the Kalman estimator K_f are given respectively as below:

$$K_r = 10^6 \times [0.97 \quad 1.61 \quad -0.06 \quad -0.45 \quad -0.09 \quad -0.53 \quad -0.05 \quad -0.30 \quad -0.02 \quad -0.14]$$

$$K_f = \begin{bmatrix} 4.15 & 0.91 & 1.87 & 0.83 & 0.49 & 0.84 & -0.14 & 0.88 & -0.35 & 0.90 \\ 0.09 & 0.32 & 0.09 & 0.31 & 0.09 & 0.31 & 0.09 & 0.31 & 0.09 & 0.31 \end{bmatrix}^T$$

The LMRP is disconnected from the BOP at 50s.

4.4.3. Simulation Results

For comparison purpose, Fig. 4.8 shows the performance of the anti-recoil control by using 16 pure hydro-pneumatic tensioners. The retrieve distance is preset to be $9.15m$ $(30\,ft)$ for every anti-recoil operation. This value is preset and tuned by engineers before the new system launching into service, so it is not adjustable after the engineer is departed from rig.

The performance of the riser hybrid tensioning system is simulated using 8 electrical tensioners and 8 hydro-pneumatic tensioners. The target displacement is not fixed to a preset height any more. Instead, it can set its target position to any position with respect to the sea bed, by simply typing the desired value into the control firmware. In the first part of this study, the riser top is set to lift $9.15m$ ($30\ ft$), $6.10m$ ($20\ ft$) and $3.05m$ ($10\ ft$) with respect to the sea bed. At last, the position reference will change to lift the riser bottom by $9.15m$ ($30\ ft$), instead of the riser top. This new anti-recoil control scheme gives good flexibility, which allows the system to fit any kind of tests.

4.4.3.1. Position Simulation for Different Position References

In Fig. 4.9, we can see that the riser top is settled to $9.15m$ smoothly without over shoot, following its position reference. It took 12 seconds for the riser string to stabilize into new position without overshot, which is about the same time duration for the hydro-pneumatic tensioners.

The simulation cases of $6.10m$ ($20\ ft$) and $3.05m$ ($10\ ft$) are shown in Fig. 4.10 and Fig. 4.11. Both waveforms demonstrate that the position reference can be easily changed, and set to any reasonable value depending on test environments. The position control strategy brings the riser top to the desired height with approximately the same rate of change. The only requirement is to configure the firmware to include a manual position reference input on the maintenance test page of the human machine interface computer.

After the riser is retrieved and soft hang-off on hydro-pneumatic tensioners, from 60 second and later in Fig. 4.8, we can see that the riser string is under constant oscillation. This behavior is dangerous and unavoidable by using only hydro-pneumatic tensioners. It exposes the choke and kill line seals to severe wear and tear, and usually is not permitted to last long under harsh weather or other conditions. However, by using the hybrid tensioning system, the riser string is constantly under position control mode, the riser and the vessel motion are completely decoupled. The vessel heave oscillation, or any other motion, does not affect the position of

riser, as shown in Fig. 4.9. So this position control strategy using hybrid tensioning system allows the riser to be free hanging in water without position fluctuation.

The same level of tension compensation also applies to the riser soft hang-off on tensioners. This feature will increase the operability of the drilling vessel. This will allow the vessel to move from one well center to other locations with the riser free hanging in water, instead of disconnect and retrieve on board.

4.4.3.2. Tension Simulation for the case of $9.15m$ ($30\ ft$) reference

The following simulation is performed based on the $9.15m$ ($30\ ft$) position reference. Fig. 4.12 illustrates that the tension delivered by the electrical tensioner is increased to its maximum value, so that it lifts the riser bottom from BOP fast and straight to avoid any collision or damage. Then the tension is reduced rapidly to decelerate the riser string from hitting the drill floor. And eventually the tension would increase gradually until it reaches the target position. The tension oscillation on the electrical tensioner from 52-60s appears, because the feedback controller was trying to correct the error produced by the state estimator.

Fig. 4.13 is the enlarged section of tension waveform from 80s to 100s in Fig. 4.12. It is obvious that the tension delivered by electrical tensioners compensates the tension variation cause by the hydro-pneumatic tensioners by $180°$, so that the total tension applied on the tension ring is smooth and constant, as shown in Fig. 4.14.

4.4.3.3. Control Input and Estimator Results

The motor stator q-axis voltage, as system control input, is shown in Fig. 4.15. A high peak voltage is expected during recoil process, which illustrates the big electrical power peak fluctuation is expected for the vessel power system.

The results of the Kalman estimator, in Fig. 4.16, show that the estimated state variables following the actual measurements. It demonstrates the effectiveness of the riser system math model. However, we can observe that the estimated position of the riser bottom has $0.2\ m$ error

against the actual measurement. A more accurate riser control plant model including non-linear effects should be considered for further control design.

4.4.3.4. Position Simulation for Other Position Reference

The target position reference is now set as lifting the riser bottom, i.e. the LMRP, by $9.15m$ ($30\ ft$), instead of the riser top. The position of the riser bottom is not measureable in this study. Therefore, this position feedback actually relies on the estimated value from the dynamic math model. Fig. 4.17 shows that the control goal is achieved; even the actual measurement is not accessible. It demonstrates that the control plant model built in this study is accurate enough for anti-recoil control purpose. It also indicates that the position of any location node along the riser string can be controlled and can be brought to a certain height to fulfill different demands. We can see that the position of riser top is slightly above $9.15m$ ($30\ ft$). It is because the heavy weight of riser puts the free-hanging riser pipes under tension and elongates the steel material. The elongation in this case is less than 0.4m.

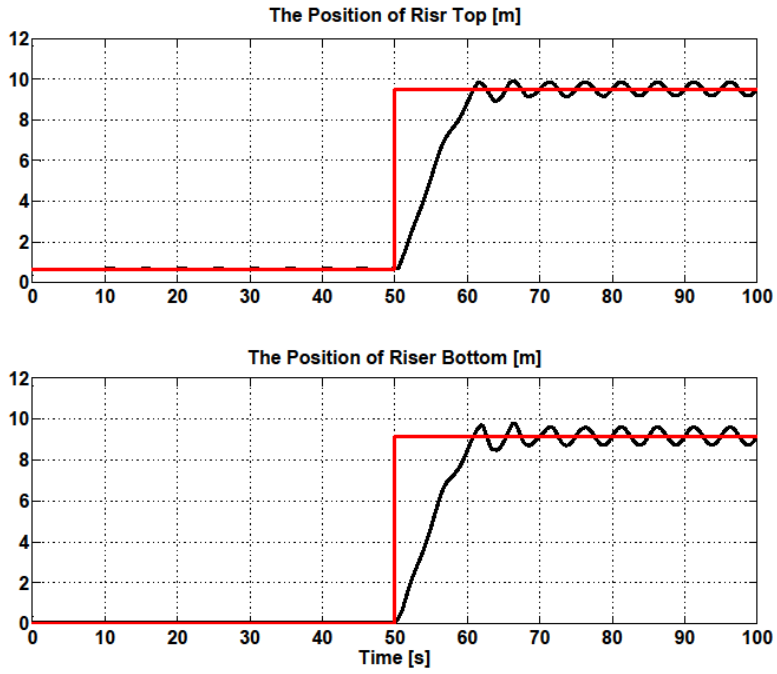

Fig. 4.8 The position of riser top and bottom using hydro-pneumatic tensioners with $9.15m$ displacement

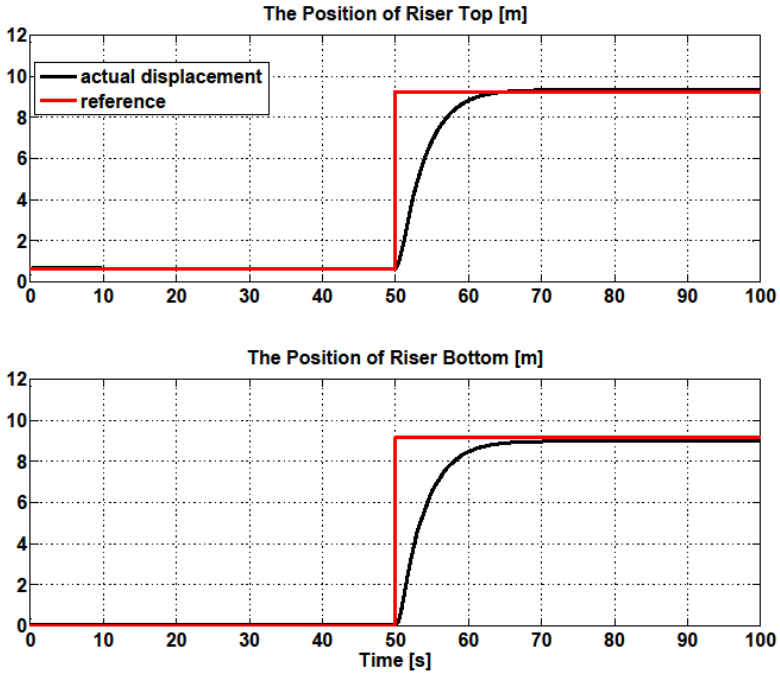

Fig. 4.9 The position of riser top and bottom using hybrid tensioning system with $9.15\ m$ displacement

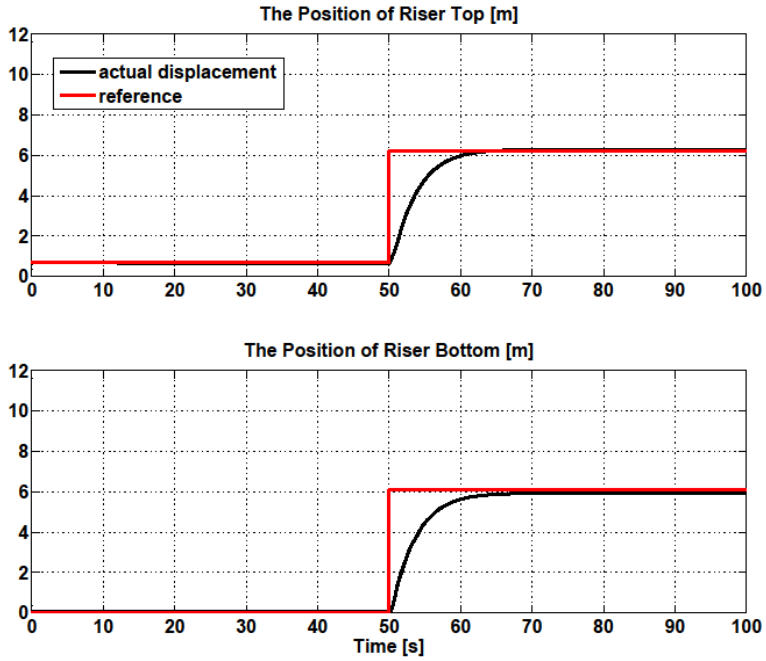

Fig. 4.10 The position of riser top and bottom using hybrid tensioning system with 6.10 m displacement

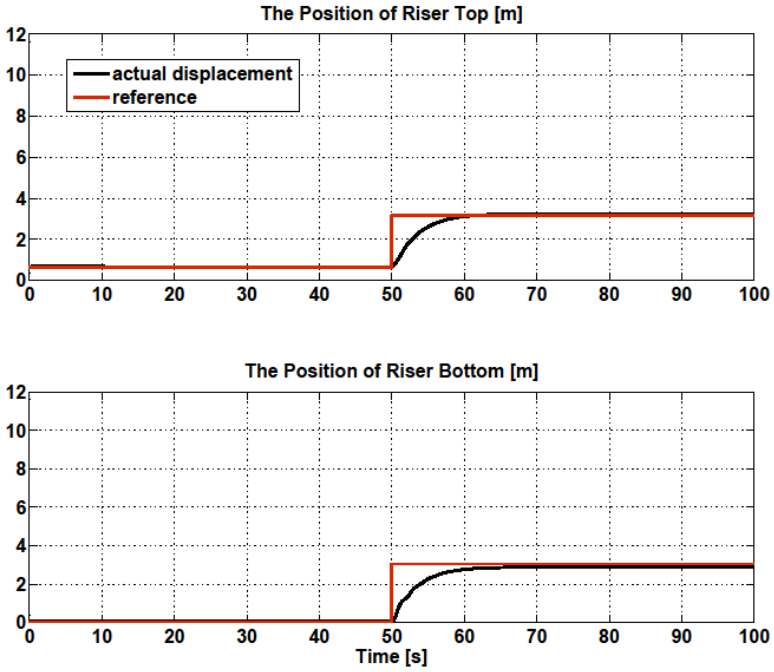

Fig. 4.11 The position of riser top and bottom using hybrid tensioning system with 3.05 m displacement

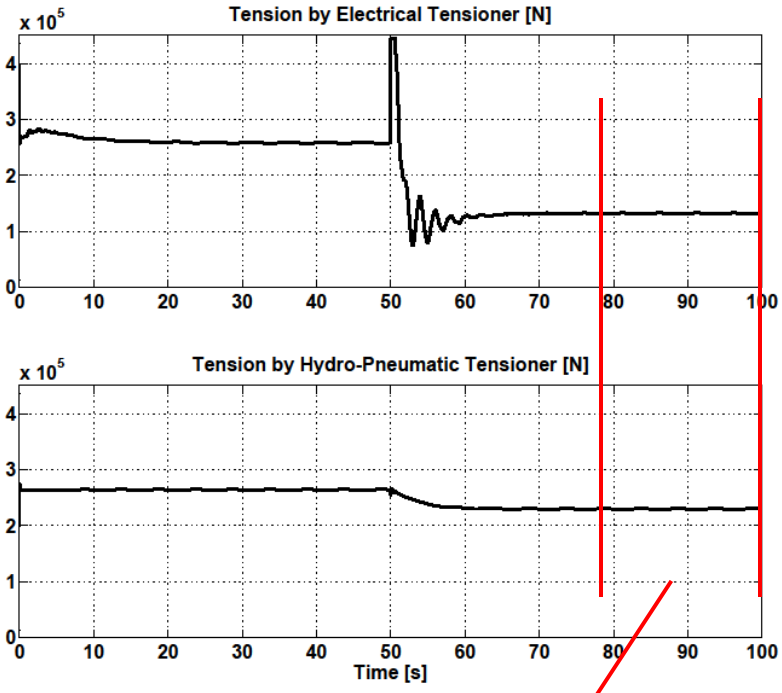

Fig. 4.12 The Tension Delivered by Electrical and Hydro-Pneumatic Tensioners

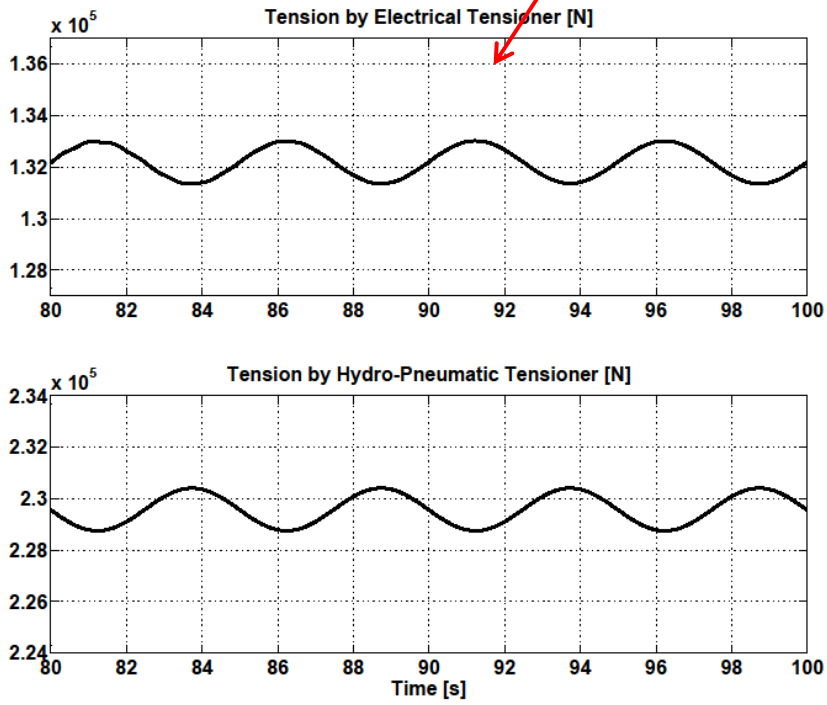

Fig. 4.13 The Tension Delivered by Electrical and Hydro-Pneumatic Tensioners (Enlarged from 80s to 100s)

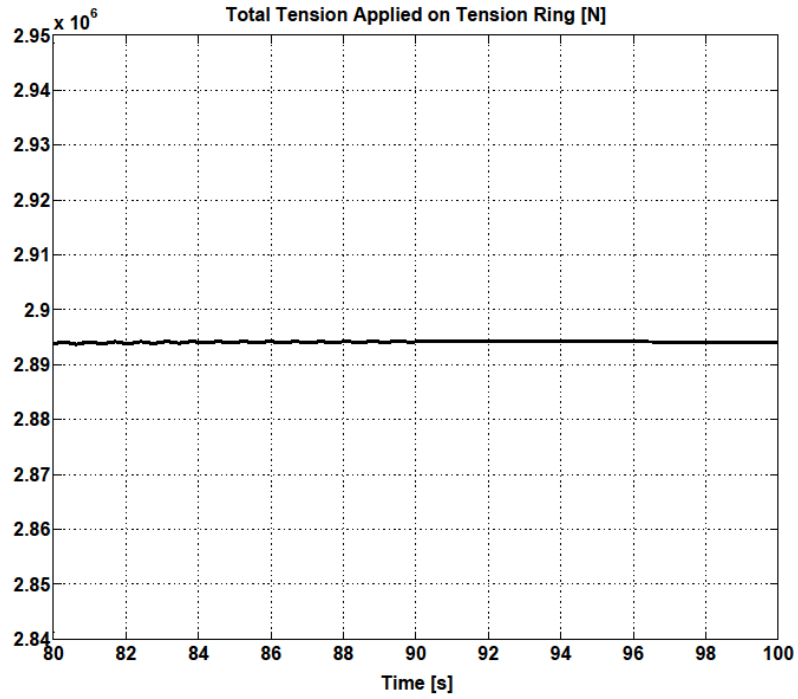

Fig. 4.14 The Total Tension Applied on the Tension Ring

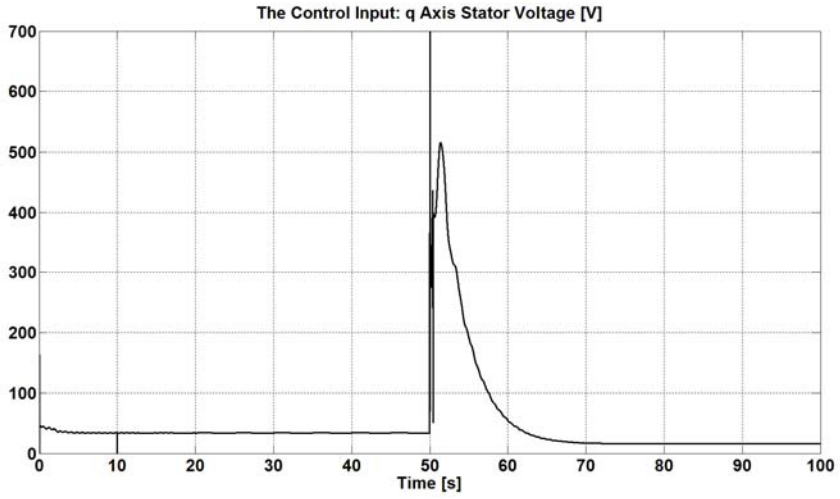

Fig. 4.15 The control input: motor stator q-axis voltage

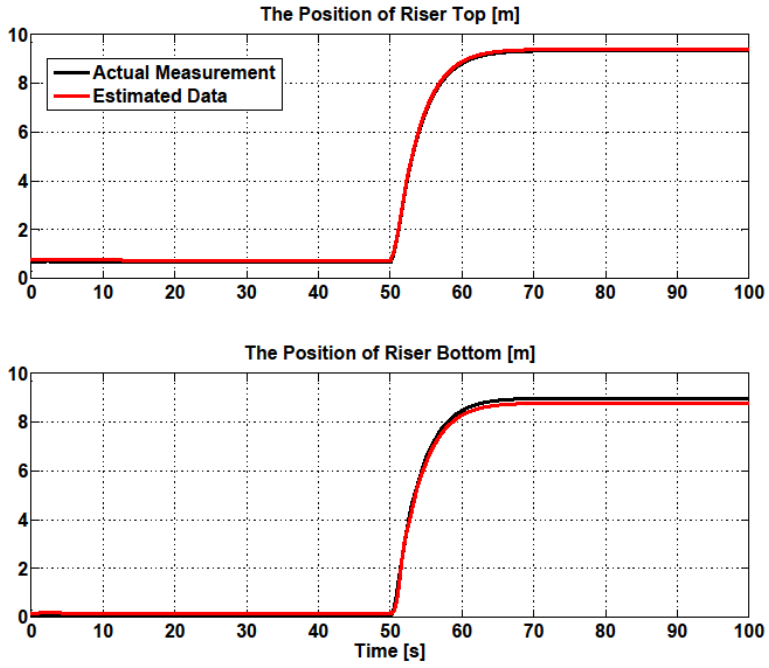

Fig. 4.16 The measured and estimated position of riser top and bottom by using the Kalman Filter

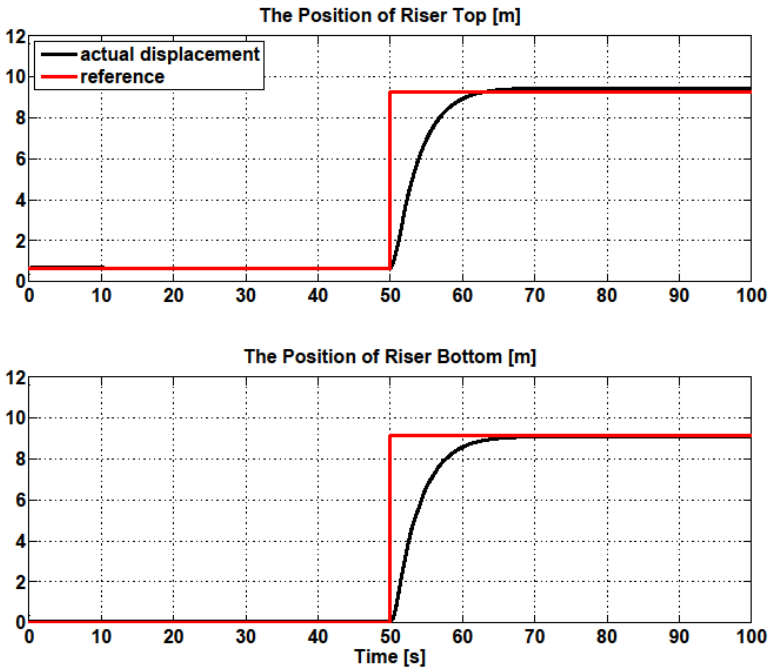

Fig. 4.17 The position of riser top and bottom by using the bottom position reference of 9.15 m

4.5. Conclusion and Discussion

By taking advantage of the novel riser hybrid tensioning system, an enhanced riser anti-recoil control strategy is developed in this chapter.

This innovation that we bring forward here is all designed to increase operating envelop of the vessel. By using the riser hybrid tensioning system, the whole riser package now becomes predictable and testable with lower risk. It highly reduces the potential damage and increases operator's confidence. The new proposed data logging system improves the detectability of the anti-recoil system. And the position control when the riser string soft hang-off on the tensioners opens the possibility to extend the operability to other operations.

A system model integrating both electrical and hydro-pneumatic tensioners and the riser string is built for anti-recoil control purpose. A LQG control design technique, as a modern optimal control design technique, is applied here, aiming for position control of the riser string. A feedback controller with the system state variable estimator is designed and implemented. The Matlab simulation helps to demonstrate the concept feasibility of the anti-recoil control and further verifies a more robust and accurate control performance.

Chapter 5: Modeling and Implementation of the VIV Suppression Control Mode

5.1. Review of the Vortex-Induced Vibration Control

Operation of a riser system in currents exceeding two knots can cause high drag loads on the riser, and may be in consequence of vortex-induced vibrations, and in turn, further increases drag and pre-mature fatigue damage. There have been a lot of studies carried out towards controlling the phenomenon of VIV for the marine riser when the vibration structure is not rigid.

A wide range of devices and control methods are used and can be classified into two broad classes: passive and active. The passive method does not require motive power, usually requires add-on structures with flow influencing characteristics; whereas the active class requires motive power, typically employing air or water pumps to disrupt vortex shedding mechanisms.

Nowadays, passive devices are mostly used on deep-water drilling risers. Several types of this class are available to the operators [66]. According to API Recommended Practice [67], one of the means to control the VIV is to increase the reduced damping (Scruton number, k_s) of the fluid-structure system. The damping could be varied by changing the mass per unit length of the structure, the fluid density and the cross stream dimension of the body. Higher damping could be introduced by utilizing materials having high internal damping such as visco-elastic materials between structural members or by using external dampers, such as Stockbridge damper [68][69]. Avoiding the occurrence of resonant condition is a possible method to reduce the excitation level and to ensure structural safety. This could be achieved by stiffening the structure (by increasing its natural frequency). The method that catches most attention is by stream-lining the structural geometry [70].

The vortex formation and shedding giving rise to pressure fluctuations is the primary cause for the occurrence of VIV and occurs in structures with bluff sections. When vortex shedding is weakened or suppressed, the drag also would be reduced. Streamline fairings (also called tear-drop fairings) are one of the most effective devices generally used to mitigate vortex-

induced vibrations. As shown in Fig. 5.1, the fairings align with the currents streamline, effectively dispersing the vortices that cause oscillating forces on its surface. The fairings are designed to rotate freely around the tubular and self-oriented with the tail pointing downstream. The forces induced due to vortex shedding could be reduced by more than two-thirds. Fairings are especially beneficial in high-current regions or near the water column where surface current dominates. Nevertheless they are sensitive to marine growth; require robustness in their mechanical design, particularly in their ability to weathervane [71], [72], [73]. Introducing add-on devices, such as helical strakes or perforated shroud, is also one of the proved and widely used control measures in various industrial and offshore applications to contain VIV. Typical helical strakes, as shown in Fig. 5.2, disrupt the correlation of vortex shedding of vortices and produce random alternating forces along the tubular length. The helical strakes usually have the pitch per start in the range of 12 to 20 times the tubular diameter, and the fin height of 25 percent of the diameter. Other add-on passive device designs are carried out in literature, such as pivoted guiding vanes, spoiler plates, perforated shroud and slats, etc [74], [75]. Kitada [105] proposed a Vortex Induced Vibration suppression method for the long-term borehole monitoring system installation by attaching the VIV reduction ropes.

Key to the operational evaluation of the workability and performance claims made was the recognition that a deep water drilling riser needs to be deployed and recovered in the shortest time possible. The passive control devices are effective in vibration suppression. However, they are expensive and cumbersome to install and remove. They will significantly slow down riser deployment and retrieval. And in absence of vibrations, some of the add-on devices experience higher drag loads than a bare riser does. [70].

Fig. 5.1 Rotatable Streamline Fairings on Drilling Riser

Fig. 5.2 Helical Strakes Wrapped on Drilling Riser

Active suppression of vortex-induced structural vibration through modification of wake vortex dynamics has attracted great attention. Existing control strategies may be categorized into two groups: flow control, which targets only vortex shedding to suppress vortex-induced vibration; and structural vibration control, which directly controls the structural vibration [76][78]. A wide variety of flow control techniques have been proposed. Muddada and Patnaik [83] implicated the direct input of energies by means of actuators driven by external sources through a controller to bring about desirable changes to the flow structure. Shaharuddin [103] developed a PID active vibration controller using iterative learning algorithm, by implementation of rotary actuators on the cylinder, and further developed Fuzzy–PID control of transverse vibrating pipe [104]. Meliga [84] used the asymptotic analysis of a low-cylinder model and proposed the possibility of dissipating vibration energy at dispose. This feedback control method has effect on lift coefficient, oscillation amplitude and harvested energy eventually. Mehmood [85] indicates that the variation of the load resistance of piezoelectric transducer during the vortex stress could be used to dissipate vibration energy. Baz and Ro (1991) [77] investigated the use of a simple velocity feedback controller, based on its operation on an internally mounted electromagnetic actuator and hotwire flow measurement, to monitor and actively attenuate

vortex-induced vibrations of a flexible circular cylinder. The method was shown to be very effective in attenuating the vibration of a single vibration mode in the synchronization regime by using a single collocated sensor/actuator pair. Venkatraman and Narayanan (1993) [86] studied the active control of vortex-induced oscillations of circular cylinders and galloping vibrations of a square prism modeled as a single dof linear damped oscillator, by using the disturbance accommodating control (DAC) philosophy. Baz (1993) [87] [88] proposed an independent modal space controller utilizing collocated piezoelectric actuators and sensors bonded to the root of a flexible cantilevered cylinder to suppress the vortex-induced vibrations of the dominant modes in cross flow. Carbonell et al.(2003) [89] formulated a control algorithm with three different schemes for suppression of flow-induced vibration (FIV) of fluid–structure interaction systems with bounded disturbance and variable parameters. The classical model of a uniform flow past an elastically supported rigid cylinder was considered to simplify the illustration. Cheng et al.(2003) [90] proposed a novel perturbation technique involving curved surface-embedded piezo-ceramic actuators to modify the interactions between synchronizing vortex shedding and structural vibration of a flexibly supported bluff body (square cylinder) in cross flow. However, their open-loop control technique (i.e., lacking the feedback of either flow or structural vibration information), suffered from two main short comings; namely, a relatively narrow perturbation frequency range to achieve the desired performance near the resonance region, and a relatively large required perturbation amplitude (i.e., about 25% of the cylinder vibration amplitude). The performance of the latter control system was greatly enhanced by Zhang et al. (2004) [90] with the deployment of a closed-loop control system perturbing the cylinder surface using piezo-ceramic actuators activated by a feedback hot- wire signal via a proportional-integral-derivative (PID) controller. It was demonstrated that the best performance can be achieved in terms of both suppressing vortex shedding and FIV of the flexibly supported square cylinder provided that feedback signal is properly chosen. Chen and Aubry (2005) [91] developed a closed-loop control algorithm by application of arrays of Lorentz force actuators for suppressing one-degree-of-freedom vortex-induced vibration of a circular cylinder in cross-flow

direction. Li et al. (2007) [92] using surface-embedded PZT micro-actuators to experimentally control vortex-induced vibration of two side-by-side circular cylinders in across flow. Wu et al.(2007) [93] proposed a multi-high-frequency perturbation controller with a feedback closed-loop system for FIV control of an elastically mounted square cylinder using surface-embedded actuators. The experimental performance of the proposed controller was found to outperform other traditional controllers, while the controller was robust towards variations in both controller parameters and physical plant conditions.

Among the above listed articles, most of them are based on installing additional electrical devices in the riser cylinder under water, to generate the control action necessary to resist the flow-induced excitations [94]. The active control may either be an open or closed loop depending on whether a feedback signal is deployed. Recently, with the development of electrical motor control technique, controlling riser behavior from the top vessel becomes a potential solution. The only material published is by Choo in 2009 [79] and consecutive papers in 2010 and 2011 [80][81]. A boundary control concept at the upper riser end is proposed, for top riser angle and forced vibration reduction, through two additional torque actuators in transverse and longitudinal directions. In his papers, the dynamic behavior of the flexible riser is represented by a distributed parameter system with partial differential equations. And boundary control laws at the top boundary of the riser are constructed to minimize the riser top ball joint angle.

The electrical tensioning system, which is able to alter the top tension dynamically within milli-second, opens the possibility of the vortex-induced vibration suppression by controlling the structural natural frequency without any add-on devices. Inspired by the physics of violin strings [95], the tension is an important factor of the tonal quality of the sound. Increasing the playing tension on a string results a higher frequency note, and decreasing the tension results in a lower frequency note. The same principle applies on the riser string in deep water drilling. The riser hybrid tensioning system makes this control concept possible to apply on the riser system.

5.2. Problem Formulation of the Vortex-Induced Vibration

5.2.1. Vortex Shedding

Vortex shedding is an oscillating flow that takes place when a fluid such as air or water flows past a bluff (as opposed to streamlined) body at certain velocities, depending on the size and shape of the body. It is a result of the basic instability which exists between the two free shear layers released from the separation points at each side of the cylinder into the downstream flow from the separation points.

Well documented experimental data have confirmed that the vortex shedding frequency for a fixed cylinder is a function of the ratio of current velocity to diameter as given by the Strouhal relation [97],[98]:

$$f_s = S_t \frac{U}{D} \tag{5.1}$$

where the Strouhal number is related to the characteristic shape and dimension of the body (diameter in the case of a cylinder), is generally about 0.2. D is the hydraulic diameter of the cylinder, and U is the flow velocity.

However if the cylinder is elastically supported and has a natural frequency close to the one given by the equation (5.1), then the vortex shedding frequency will adapt itself to the natural frequency of the cylinder and the Strouhal relation will be modified. This situation is known as “lock-in”. When this happens large and damaging vibrations can result. The drilling rig usually suspends the operation until the VIV excitation conditions cease away, which may take several days.

5.2.2. Governing Model of the Forced Vibration of the Flexible Marine Riser

The reference frame for the riser is shown in Fig. 5.3 with the origin set on top of the LMRP and BOP package. We can derive the equations of motions for the flexible riser

independently for each principle reference plane, $x, y\, z$. As such, only lateral dynamics of the riser system is considered in this chapter.

In general, two methods of modeling have been used to predict riser response to the external excitation force. They are finite element method (FEM) in the time domain and the modal method in the frequency domain [83]. The finite element method is based on the mass and stiffness matrices and the load vector of beam. The riser string is replaced by $(n-1)$ discrete elements which are connected by n nodal points. The interfacial nodes can be subjected to external forces, moments or both, and depend on the nature of support condition at the node.

In this study, we implement the modal analysis approach, because the control objective of this study is set to change the stiffness of the pipe, hence to change the natural frequency of the riser system. The modal analysis provides an easy way to identify the candidate frequencies for lock-in oscillation. It is also more explicit to control the vibration level of each frequency mode. Furthermore, both time domain and frequency domain solutions can be directly obtained from eigenvalue equations and classical mechanical vibrations.

The dynamics of the riser system is idealized as a tensioned Euler-Bernoulli beam for small angles of deflection. The lateral displacement of a point along the length of the riser is represented by $y(x,t)$, a function of space $x \in [0, L]$ and time $t \in [0, \infty)$.

The vessel horizontal offset and platform motions are not considered, as these effects is considered constant mean displacement, distinguishing from the oscillation pattern. And they can be included through displacement influence functions or shifting functions by following the guidance in [79],[99].

The transverse vibration of the beam is assumed to be a plane of symmetry for any cross section. Fig. 5.4 shows the force diagram of the beam element of dx. The transverse vibration of the beam is derived in reference [99]. And the governing equation for the flexible marine riser is shown in the equation (5.2). It is a fourth order Partial Differential Equation (PDE) with axial tension, structure damping and external disturbances terms [67].

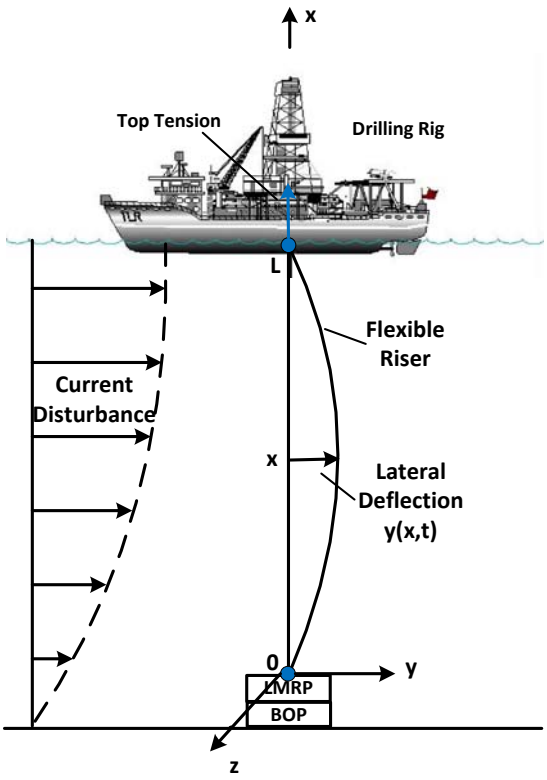

Fig. 5.3 System Overview and Assigned Reference Frame

Consider a uniform elastic beam with length L, axial co-ordinate X ($0 \leq X \leq L$), flexural rigidity EI, vertical tension applied on the beam top T, uniform mass per unit length $m_z > 0$, viscous damping coefficient of the linear structural damping $c > 0$,

$$EI\frac{\partial^4 y(x,t)}{\partial x^4} - T\frac{\partial^2 y(x,t)}{\partial x^2} + m_z\frac{\partial^2 y(x,t)}{\partial t^2} + c\frac{\partial y(x,t)}{\partial t} - f(x,t) = 0 \tag{5.2}$$

And its boundary conditions are:

$$y(0,t) = 0 \tag{5.3}$$

$$EI\frac{\partial^2 y(0,t)}{\partial x^2} = 0 \tag{5.4}$$

$$y(L,t) = 0 \tag{5.5}$$

$$EI\frac{\partial^2 y(L,t)}{\partial x^2} = 0 \tag{5.6}$$

where equation (5.3) - (5.6) represent a pin-pin supported long beam at $x = 0$ and $x = L$ respectively. The governing equation (5.2) for the flexible marine riser pipe is a fourth order PDE with vertical tension, structural damping and external disturbance terms, remaining in the same consistent form with Ref [79].

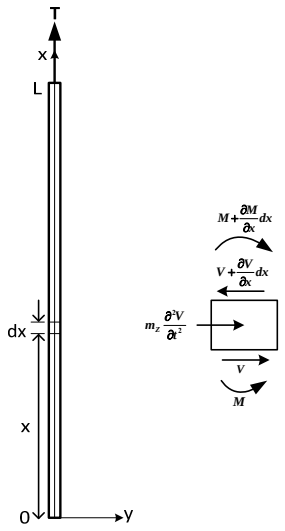

Fig. 5.4 Force Diagram of the Beam Section dx

5.2.3. Effects of time-varying current and waves

The riser is exposed to both current and waves. The cyclical surface current and the cyclical wave are the dominant vortex excitation sources. The distributed load on a 3D riser structure, $f(x,z,t)$ can be simulated as a combination of the in-line drag force $f_D(x,t)$, comprising of a mean drag force and a sinusoidal oscillating drag force about the mean, as shown below:

$$f_D(x,t) = \frac{1}{2}\rho_s C_D U(x,t)^2 D + A_D cos(4\pi f_s t + \beta) \tag{5.7}$$

and the oscillating lift force $f_L(z,t)$, which is perpendicular to $f_D(x,t)$, about a mean deflected profile,

$$f_L(z,t) = \frac{1}{2}\rho_s C_L U(x,t)^2 D cos(2\pi f_s t + \alpha) \tag{5.8}$$

where z is an axis perpendicular to the plane XOY as shown in Fig. 5.3.

The $f_D(x,t)$ is applied in the y axis and reduces gradually from $x = L$ to $x = 0$. $U(x,t)$ is the time varying surface current. C_D and C_L are the dimensionless drag and lift coefficient respectively, which characterize the drag and lift resistance of the riser pipe in the fluid environment, highly depending on the Reynold number. The f_s is the shedding frequency, expressed in equation (5.1). ρ_s is the sea water density. β and α are the phase angles. A_D is the amplitude of the oscillation part of the drag force.

The vector sum of the two perpendicular forces result in a force with oscillating magnitude and direction, therefore producing a shape of "8" vibration displacement in the riser, as shown in Fig. 5.5, in addition to the mean non-oscillating displacement. It would be helpful to build an accurate model in both axis and control design applied to these two cases for vibration reduction of the VIV problem. However, the interaction between two separate axes and a lot of other effects, such as the variable thermal density of water, the buoyancy of different floatation sections, etc, would affect the accuracy of the model by various coefficients which are hard to predict. Furthermore, the objective of this study is to demonstrate the control strategy reducing the fatigue caused by cyclical loading. By modulating the tension applied on top of the riser string, the cyclical loading of the whole riser string will be significantly reduced and the overall system will become more stationary. It will be impossible for this study to compensate the cyclical loading to zero perfectly. In order to demonstrate this control objective, only one

direction of riser deflection is considered. Hence, the distributed excitation force is considered as the drag force of equation (5.7), $f(x,t) = f_D(x,t)$.

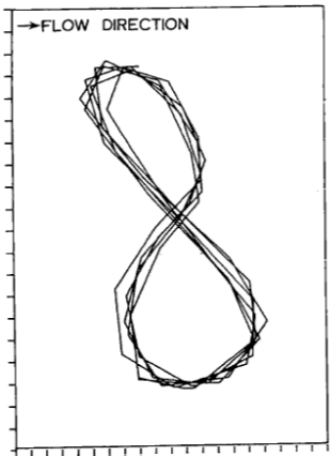

Fig. 5.5 Displacement Pattern of a Riser at Resonant Vortex-Induced Vibration

A typical surface current profile can be expressed as Fig. 5.6. The ocean surface current velocity $U(L,t)$ can be modelled as a mean non-oscillating flow with worst case sinusoidal components to simulate the riser with a mean deflected profile. The sinusoids should include all possible natural modes of the riser, which may excite the vortex shedding. The surface current $U(L,t)$ can be expressed as:

$$U(L,t) = \overline{U} + U_m \sum_{i=1}^{N} sin(\omega_i t)\,, \qquad i = 1,2,\dots,N \tag{5.9}$$

where $\overline{U}$ represents the mean flow non-oscillating current and U_m is the amplitude of the oscillating flow. The amplitude of the total ocean surface current profile $U(x,t)$ is related to the depth of the ocean, linearly declines from V_4 to V_3, then from V_2 to V_1 at the ocean floor.

The wave can also be described as the sum of sinusoidal components with frequencies of all possible natural modes of the riser that excites the vibration, and can be simulated as addition or subtraction of the current cyclic force, as shown in Fig. 5.6. The surface peak to peak amplitude is H, and declines from the ocean surface at the rate of a quadratic function.

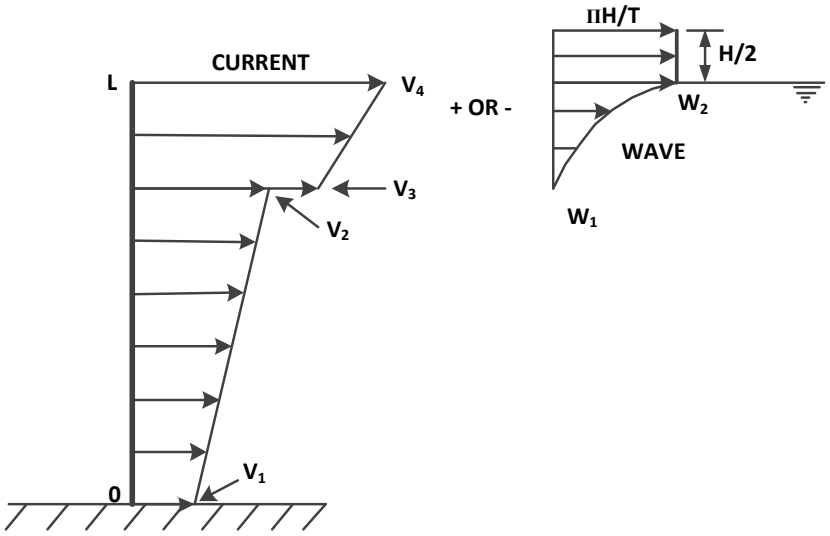

Fig. 5.6 Example of Current and Wave Profile

5.2.4. Modal Analysis of the Governing Model of the Riser String

As the governing equation of the riser system (5.2) and its boundary conditions (5.3) - (5.6) derived in this study, is a fourth order partial differential equation (PDE), does not have an easily obtainable closed-form solution. Hence, numerical methods are used to obtain an approximate solution of the problem with sufficient accuracy [79][100].

Step I :

The natural modes of the vibration can be obtained by setting external forces in equation (5.2) to zero and solving the homogenous equation (5.10) which represents the free vibration characteristic of the plant.

$$EI\frac{\partial^4 y(x,t)}{\partial x^4} - T\frac{\partial^2 y(x,t)}{\partial x^2} + m_z\frac{\partial^2 y(x,t)}{\partial t^2} + c\frac{\partial y(x,t)}{\partial t} = 0 \tag{5.10}$$

Step II :

By the "method of separating variables", and using Assumed Mode Method (AMM) with constrained modes, we set the solution $y(x,t)$ to take form of: [79], [80]

$$y(x,t) = \sum_{i=0}^{\infty} \phi_i(x) q_i(t) \tag{5.11}$$

where $\phi_i(x)$ are the mode shape functions, which are orthogonal polynomials satisfying the boundaries. $q_i(t)$ are the generalized coordinates. The integer i is the i^{th} mode. The natural frequencies of the riser can be expressed as

$$\omega_i^2 = \frac{1}{m_z}(\frac{i\pi}{L})^2 [EI\left(\frac{i\pi}{L}\right)^2 + T] \tag{5.12}$$

where the ω_i is the natural frequency of the i^{th} mode.

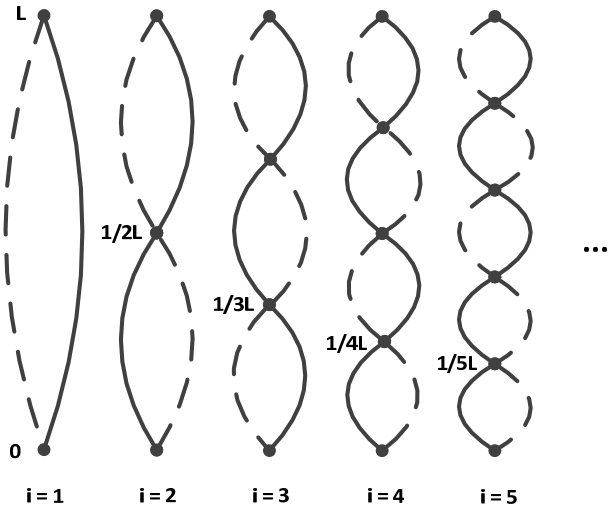

Fig. 5.7 First 5 Modes of Free Vibration Forms of a Riser

ϕ_i should meet orthogonality condition of,

$$\int_0^L \phi_i \phi_j dx = \begin{cases} 0, & i \neq j \\ 1, & i = j \end{cases} \tag{5.13}$$

Step III :

Arranging equation (5.10) into two ordinary differential equations (ODE) with one dependent on x and the other purely time varying. Each mode shaper function $\phi_i(x)$ should satisfy the boundary conditions (5.3)-(5.6) with associated natural frequencies. The mode shaper functions are, following [162]:

$$\phi_i(x) = \frac{\sqrt{2L}}{L}(sins_{2i}x - \frac{sins_{2i}L}{sinhs_{1i}L}sinhs_{1i}x) \tag{5.14}$$

where

$$s_{1i} = \{\frac{1}{2EI}[T + (T^2 + 4EIm_z\omega_i^2)^{1/2}]\}^{1/2} \tag{5.15}$$

$$s_{2i} = \{\frac{1}{2EI}[-T + (T^2 + 4EIm_z\omega_i^2)^{1/2}]\}^{1/2} \tag{5.16}$$

Step IV :

We now bring the solution (5.11) into the governing equation (5.2) and its boundaries:

$$\int_0^L m_z\ddot{y}\delta ydx + \int_0^L (EIy'''' - Ty'')\delta ydx + \int_0^L c\dot{y}\delta ydx = \int_0^L f\delta ydx \tag{5.17}$$

Here and below, primes and dots are the abbreviations of the derivatives with respect to the coordinate x and time t, respectively. The forced vibration partial differential equation can be transformed into the following equation (5.18), by substituting the mode shaper (5.14) into the governing equation:

$$\sum_{i=1}^{\infty}[m_z\ddot{q}_i(t) + c\dot{q}_i(t) + m_z\omega_i^2 q_i(t)] = \sum_{i=1}^{\infty}\int_0^L f(x,t)\phi_i(x)dx \tag{5.18}$$

Each $q_i(t)$ corresponds to a modal frequency of the system.

Wave spectra of ocean show that the ocean wave periods in offshore drilling areas are usually high in comparison with the periods of the natural vibration modes in marine risers. For

example, periods of dominant wave components in the North Sea ae around 10-12s while the fundamental natural period of a 1000 meter riser is around 7.2 second. The nature period of second mode is around 3.4 second. Higher order modes have even smaller natural periods. It is therefore reasonable to anticipate that only the first few natural vibration modes particularly dominant in the dynamic response of marine risers. The infinite series in equation (5.18) can be assumed into a finite equation as follow:

$$\sum_{i=1}^{N}[m_z\ddot{q}_i(t) + c\dot{q}_i(t) + m_z\omega_i^2 q_i(t)] = \sum_{i=1}^{N}\int_0^L f(x,t)\phi_i(x)dx \tag{5.19}$$

where N is the number of mode shapers taken in consideration. The corresponding solution $y(x,t)$ can be assumed as follow:

$$y(x,t) = \sum_{i=0}^{N}\phi_i(x)q_i(t) \tag{5.20}$$

The solution $y(x,t)$ can be obtained for any water depth x by calculating the mode shaper equations (5.14) and solving the generalized coordinates $q_i(t)$ in the equation (5.19).

5.3. Control Design of the Vortex-Induced Vibration

5.3.1. Concept of Control Design

The control objective of this chapter is to control the tension of the riser string, at frequencies and magnitudes made available by the electrical tensioning system, to reduce the oscillating part of the riser lateral displacement $y(x,t)$, subjected to the time-varying distributed transverse load from ocean current and waves. This objective is achieved by avoiding the excitation of the oscillation into resonance by disturbing the resonant condition and avoiding oscillation energy to be built in riser, and furthermore, to reduce the amplitude of the vibration in case that the riser is locked into resonant condition by damping the accumulated kinetic energy. By applying dynamically changing vertical tension on the riser top, we alternate and disturb the

riser string's natural resonant frequencies and stiffness. A control law is designed by using the feedback signals of the position and velocity of the top of riser and the lateral displacement of the riser in water.

The data logging system installed on the top of riser provides necessary information on the riser bending amplitude and frequency. Since the elasticity of the riser string is relatively small compared to the resonant amplitude, the total length of the riser will not have visible change during VIV. The vertical vibration amplitude and frequency of the riser top accurately reflects the riser string lateral vibration under water. Hence, by monitoring the vertical position and velocity of the riser top, we are able to estimate the riser string vibration [101].

We assume that the riser string oscillates around the both sides of a constant center position. The riser string captures a certain amount of ocean energy initially, and is forced to start oscillating. As shown in Fig. 5.8, during the period that the riser leaves the center, swinging towards the maximum amplitude, the whole riser pipe stretches and decelerates. The vertical tension applied on each small section of pipe increases due to the material stretch. The riser kinetic energy transfers into potential energy. Thus, if we decrease the tension applied on top of the riser, then the tension stress on each small section decreases, the riser outward movement slows down. And during the period that the riser swings back towards the center position, the riser accelerates and returns back to the original shape. The tension put on each small section of the riser decreases. The riser potential energy transfers back into kinetic energy. If we increase the tension applied on top of the riser, the tension stress on each small section increases, this accelerates the riser inward movement, until the maximum tension applied when the riser is at the center.

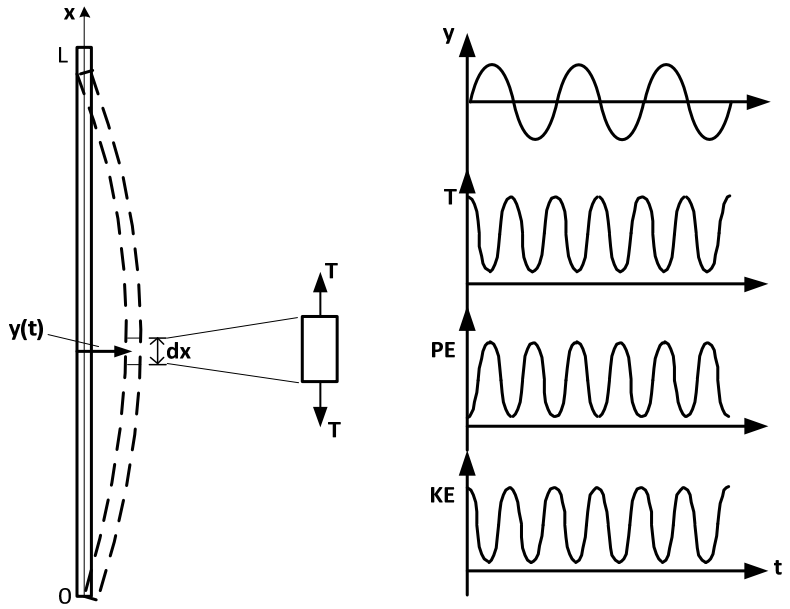

Fig. 5.8 The Variation of Different Variables during VIV (the Lateral Displacement y, the Tension T, the Potential Energy PE and the Kinetic Energy KE)

5.3.2. Energy Perspective Analysis

From the system governing equation (5.2), we can see that the only damping element of this system is the structural damping coefficient c. This inherited structural damping nature is usually not sufficient for large external excitation force during harsh weather or loop current conditions. The riser pipe locks into a resonant condition and the vibration amplitude increases until reaching the equilibrium point against the damping, or even until tearing apart the riser string. The objective is to control the time-varying tension ΔT, in order to damp out the oscillation energy excited by the external forces.

The kinetic energy of the riser system E_k can be represented as a function of time t, in Refs [79], [99]

$$E_k = \frac{1}{2} m_z \int_0^L [\frac{\partial y(x,t)}{\partial t}]^2 dx \tag{5.21}$$

The potential energy for the flexible riser due to the bending stress E_p can be represented as

$$E_p = \frac{1}{2} EI \int_0^L [\frac{\partial^2 y(x,t)}{\partial x^2}]^2 dx \tag{5.22}$$

The work done by the top tension in elongating the riser is

$$W_t = -\frac{1}{2} T \int_0^L [\frac{\partial y(x,t)}{\partial x}]^2 dx \tag{5.23}$$

and the total work done on the system, W, is given by

$$W = W_t + W_f + W_d \tag{5.24}$$
$$= \int_0^L \left\{ -\frac{1}{2} T \left[\frac{\partial y(x,t)}{\partial x} \right]^2 + \left[f(x,t) - c \frac{\partial y(x,t)}{\partial t} \right] y(x,t) \right\} dx$$

where W_f is the work done by the distributed transverse load $f(x,t)$ and W_d is the work done by the structural damping coefficient c.

Given the extended Hamilton's principle, we get

$$\int_{t_1}^{t_2} \delta \big(E_k - E_p + W \big) dt = 0 \tag{5.25}$$

where $t_1 < t < t_2$, and δ implies a variation in the system. Substituting equations (5.27)-(5.24) into equation (5.25), we obtain:

$$\int_{t_1}^{t_2} \int_0^L \delta \left\{ \frac{1}{2} m_z [\frac{\partial y(x,t)}{\partial t}]^2 - \frac{1}{2} (T_0 + \Delta T(t)) \left[\frac{\partial y(x,t)}{\partial x} \right]^2 - \frac{1}{2} EI \left[\frac{\partial^2 y(x,t)}{\partial x^2} \right]^2 \right. \tag{5.26}$$
$$\left. + \left[f(x,t) - c \frac{\partial y(x,t)}{\partial t} \right] y(x,t) \right\} dx\, dt = 0$$

The first and the second terms in Equation (5.26) are opposing each other. It indicates that by modulating the work done by the top tension, W_t, we are able to dissipate the

accumulated kinetic energy E_k caused by the external load W_f. So the total oscillation energy can be reduced by manipulating the applied top tension.

5.3.3. Constant Gain Velocity Control using Lateral Displacement Measurement

Assume that the tension applied on top of the riser consists of two parts, a constant T_0, and a time-varying $\Delta T(t)$

$$T_{ref}(t) = T_0 + \Delta T(t) \tag{5.27}$$

We propose the time-varying part of the tension $\Delta T(t)$ to be controlled based on the feedback measurement from the sensor installed on riser. Assuming an accelerometer type of sensor is installed in the middle of the riser, i.e., at the water depth of $0.5L$. We choose $\Delta T(t)$ to be proportional to the sensor velocity measurement. The control law can be represented in following:

$$\Delta T_1(t) = \mu \frac{\partial y(x,t)}{\partial t}\Big|_{x=0.5L} \tag{5.28}$$

where μ is the proportional constant which determines the magnitude of the control tension.

$\Delta T_1(t)$ is a generic controller that injects damping coefficient and is implemented as a user-defined function. Now the equation (5.17) becomes:

$$\int_0^L m_z \ddot{y}\delta y dx + \int_0^L (EIy'''' - T_0 y'')\delta y dx + \int_0^L (c + \dot{y}y'')\delta y dx = \int_0^L f\delta y dx \tag{5.29}$$

The modal form of the governing equation becomes:

$$\sum_{i=1}^{N} \{m_z \ddot{q}_i(t) + c\dot{q}_i(t) + \mu q_i(t)\dot{q}_i(t)|_{x=0.5L} + m_z\omega_i^2 q_i(t)\} = \sum_{i=1}^{N} \int_0^L f(x,t)\phi_i(x)dx \tag{5.30}$$

Fig. 5.9 shows the system response to a pulse signal of load force. The second graph indicates that the first cycle of lateral displacement is reduced by the CGVC controller. The

amplitude of the displacement is reduced by 18.2%. The oscillation period becomes longer by using the control method. Hence, the duration of the vibration also becomes longer. This indicates that the top tension variation has visible influence on the system natural frequency. We can say that, the controlled time-varying tensioner $\Delta T_1(t)$ is able to reduce the vibration amplitude and can be served as an active damping device.

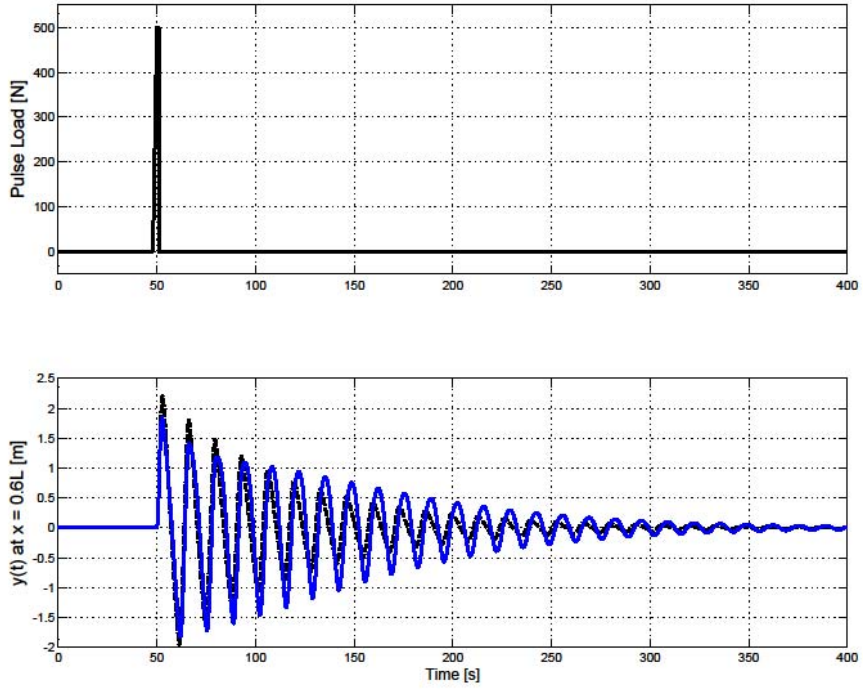

Fig. 5.9 (a) External Pulse Force Applied on Riser (b) Riser Displacement Response $y(t)$ at $x = 0.5L$ with Control $\Delta T_1(t)$ (Blue Solid) and Without Control (Black Dash)

The problem of using the feedback of $\frac{\partial y(x,t)}{\partial t}\Big|_{x=0.6L}$ is that installing sensor on riser and transferring feedback signals from deep water, does not have an easy solution, due to high noise content, signal transferring speed and signal reliability issues from water to surface. A sensor measuring the lateral movement closer to the top may be more feasible in practical rig installation, such as $\frac{\partial y(x,t)}{\partial t}\Big|_{x=0.99L}$. However, the accuracy of that signal needs to be examined more carefully, since the lateral movement of this point is very limited, comparing to the lateral

movement in the middle of the riser. Therefore, an improved and easy to access measurement method is required.

5.3.4. Constant Gain Velocity Control using Longitudinal Position Measurement

Assuming that the material elongation of the riser pipe is due to vibration is very small. As shown exaggerated in Fig. 5.10, the total length of the riser is L. During the period that the riser is traveling laterally from the center to the maximum amplitude, the longitudinal position h decreases. And during the period that the riser is returning back to the center, the longitudinal position increases.

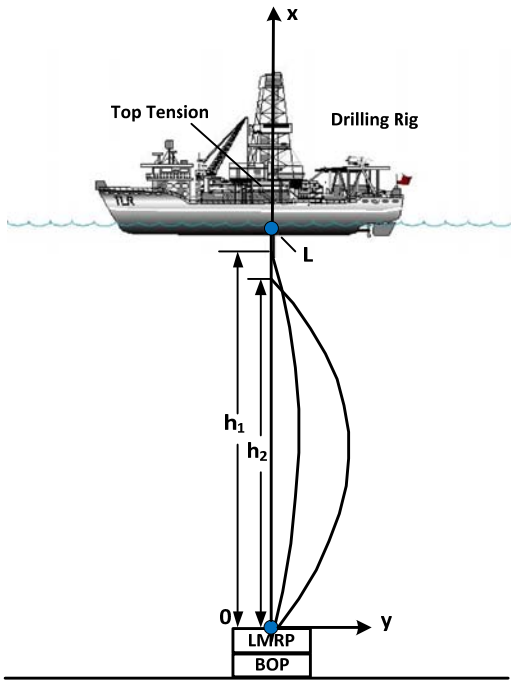

Fig. 5.10 The Longitudinal Position of the Riser during Oscillation

A closed-loop controller is proposed here using the rise top longitudinal position $h(t)$. The control law is represented in the form:

$$\Delta T_2(t) = \sigma \frac{\partial h_{x=L}}{\partial t} \tag{5.31}$$

where σ is proportional constant which controls the magnitude of the control tension $\Delta T_2(t)$. It is clear that controller (5.31) admits simpler implementation compared to the controller of equation (5.28), since there is no data acquisition problem. The $\Delta T_2(t)$ alternates the system stiffness and adds larger damping coefficient into the governing equation.

The system response to the pulse load change is shown in Fig. 5.11. In the graph (b), we can see that, this controller $\Delta T_2(t)$ is able to reduce the system response by 45%, depending on the choice of the proportional gain σ. The controller $\Delta T_2(t)$ has very good damping effect on the resonant amplitude of the dominant frequency.

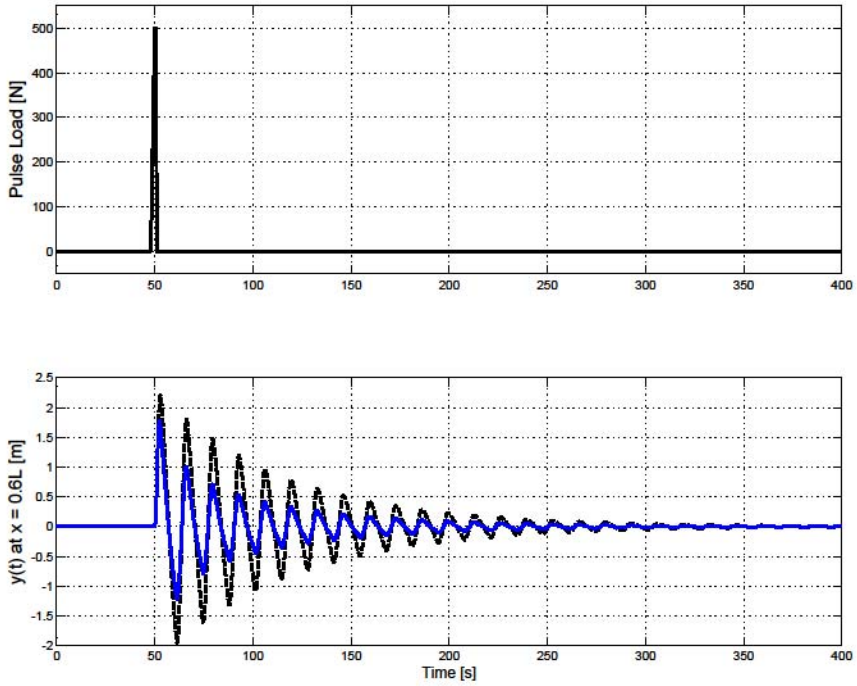

Fig. 5.11 (a) External Pulse Force Applied on Riser (b) Riser Displacement Response $y(t)$ at $x = 0.5L$ with Control $\Delta T_1(t)$ (Blue Solid) and Without Control (Black Dash)

From Fig. 5.12, we can see that, the most significant difference between the controller $\Delta T_1(t)$ and $\Delta T_2(t)$ is that the oscillation frequency of the longitudinal movement is twice comparing to the frequency of the lateral displacement.

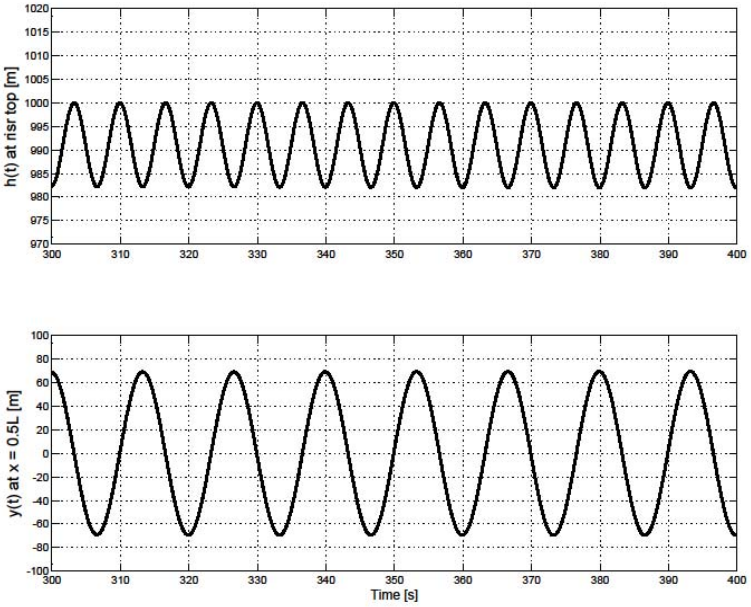

Fig. 5.12 (a) Response to the Riser Top Longitudinal Displacement $h(t)$ Control (b)) Response to the Riser Lateral Displacement $y(t)$ at $x = 0.5L$

5.4. Simulation

The closed loop system (5.2) is simulated to investigate the performance of control laws (5.28) and (5.31). Detailed parameters are listed below:

Table 5.1: Detailed Numerical Values of the system simulation

Parameter	*Description*	*Value*	*Unit*
E	Young's Modulus	2.07×10^8	kN/m^2
d_o	Outer Diameter	0.5334	m
d_i	Inner Diameter	0.4826	m
L	Length of Riser	1000	m
m_z	Mass per Unit Length	440	kg/m
c	Structural Damping	12.0	
T_0	Steady State Tension	9×10^6	N
ρ_s	Sea Water Density	1024	kg/m^2
C_d	Drag Coefficient	1.361	
f_v	Vortex Shedding Frequency	2.625	Hz
n_{sim}	Number of simulation points along L	100	

The system is simulated using the model (5.19) developed in the previous section, where the first five modes are considered, $N = 5$. 100 simulated points are evenly distributed along the riser, in order to simulate the overlay riser profile in water. The riser lateral displacement is simulated using (5.20) with 10 meter interval. A Matlab Simulink model is built and the ODE is numerically solved using the Dormand-Prince Method with adaptive step size.

5.4.1. Simulation of the Ocean Current and the Vortex Excitation Force

The riser is initially at rest, and is excited by a distributed transverse load, caused by current and wave, in Fig. 5.6. A depth dependent ocean current profile is simulated. The amplitude of the ocean surface current in equation (5.9) is distributed and linearly declines from surface $V_4 = U(L,t)$ at $x = L$ to $V_3 = 0.7U(L,t)$ at $x = 0.7L$, then $V_2 = 0.6U(L,t)$ at $x = 0.7L$ to $V_1 = 0.1U(L,t)$. And the surface amplitude of wave speed is simulated as a superposition to the current, $H = 0.3U(L,t)$. It also declines from the surface at the rate of a quadratic function to zero at $x = 0.7L$.

The surface current $U(L,t)$ in equation (5.9) is the addition of non-oscillating mean flow $\overline{U} = 2\,m/s$ and the oscillating flow $U_m = 0.2\,m/s$. Large vibration stresses are normally associated with a resonance that exists when one of the natural frequencies is tuned to the frequency of the imposed force. So the current frequencies are simulated to correspond to the first five natural modes of the vibration, $\omega_i = \{0.4494 \quad 0.8994 \quad 1.3506 \quad 1.8035 \quad 2.2588\}$ for $i = 1\ to\ 5$. The simulated surface current velocity is shown in Fig. 5.13.

The vortex excitation force $f(x,t)$ is simulated using equation (5.7), which is repeated below with $C_d = 1.361$, and $\beta = 0^{\circ}$. A_D is the amplitude of the oscillatory part of the drag force, typically 20% of the first term in $f_D(x,t)$. f_s is the vortex shedding frequency, which is defined in (5.1), with a reasonable Strouhal number of $S_t = 0.2$, resulting in a vortex shedding frequency of $f_s = 0.7499\,Hz$. Fig. 5.14 shows the vortex excitation force $f(x,t)$, as a mean drag force and an oscillating force.

$$f(x,t) = \frac{1}{2}\rho_s C_D U(x,t)^2 D + A_D cos(4\pi f_s t + \beta)$$

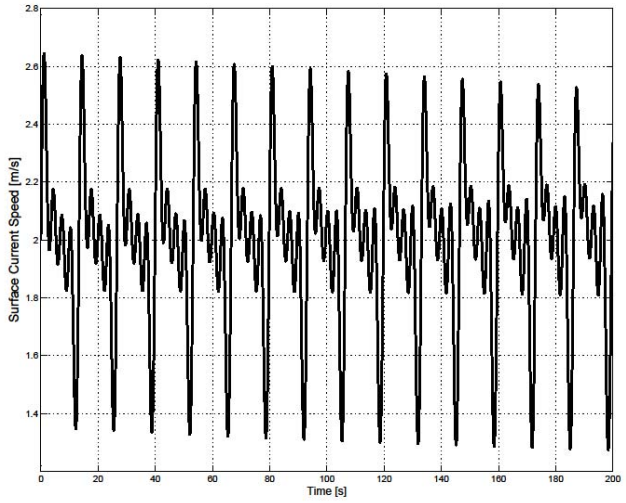

Fig. 5.13 Ocean Surface Current Speed Modeled as a Mean Current and Sinusoids of Riser Natural Frequencies

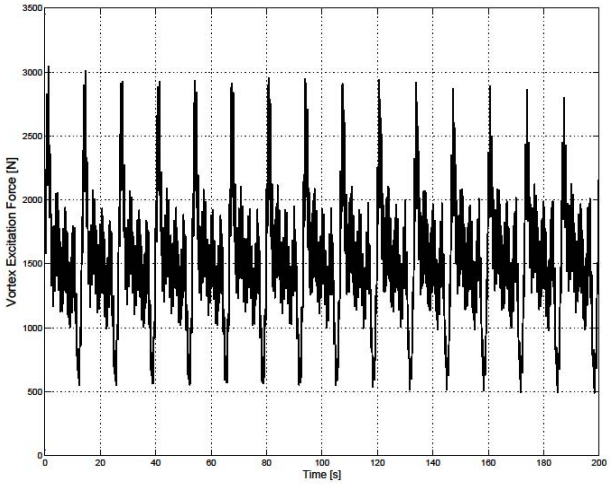

Fig. 5.14 Vortex Excitation Force at Ocean Surface Modeled as a Mean Drag Force and an Oscillating Force

5.4.2. Simulation of the Non-Controlled System Behavior

The uncontrolled lateral vibration magnitude of the riser is examed at $x = 400m$ and $x = 750m$, as shown in Fig. 5.15 and Fig. 5.16. The resonant kinetic energy is built up over time by the repetitive excitation force, until the damping energy into losses becomes balanced with the external excitation energy. The amplitude of the lateral vibration stays at the equilibrium point. At the worst location along the riser string, $x = 400m$, the amplitude of vibration reaches $22\,m$. And at the location closer to the surface, $x = 750m$, the amplitude stays at $18\,m$. The period of the vibration is $13.5\,sec$. This matches well the first natural frequency of the rise system, which is $0.4494\,rad/s$, i.e., $13.98\,sec$.

The most severe lateral displacement $y(400, t)$ can be separated into each natural coordinate: $y(x,t) = \sum_{i=0}^{\infty} \phi_i(x) q_i(t)$. Fig. 5.17 below shows the decomposition of the first five $\phi_i(x) q_i(t)$. It is obvious that the first order natural mode has amplitude of $22m$, which dominates the resonant behavior. Under this simulated current and wave condition, the riser "locks-into" the vortex-induced vibration of its first order natural frequency mode.

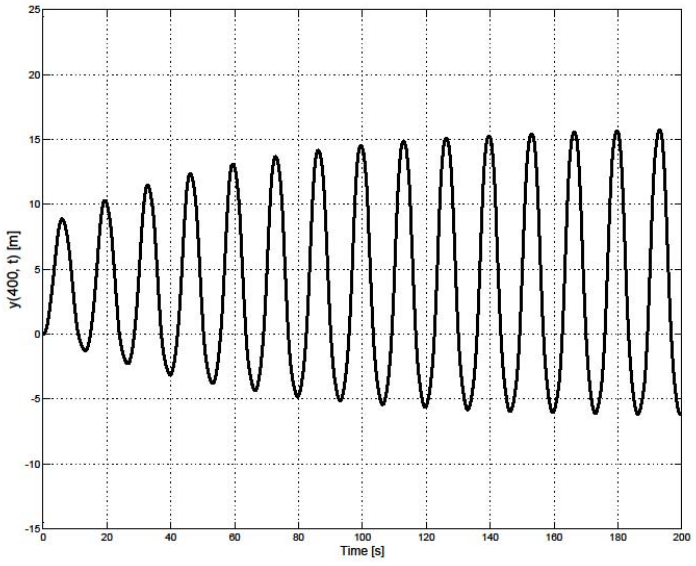

Fig. 5.15 Riser Displacement at $x = 400m$, Without Control

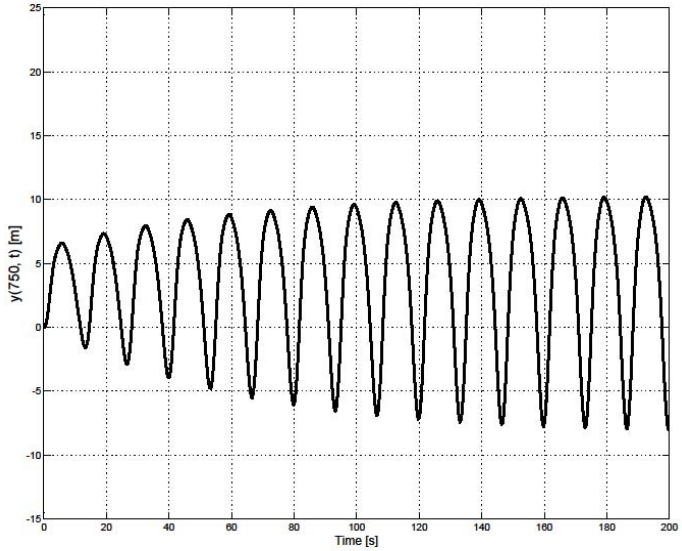

Fig. 5.16 Riser Displacement at $x = 750m$, Without Control

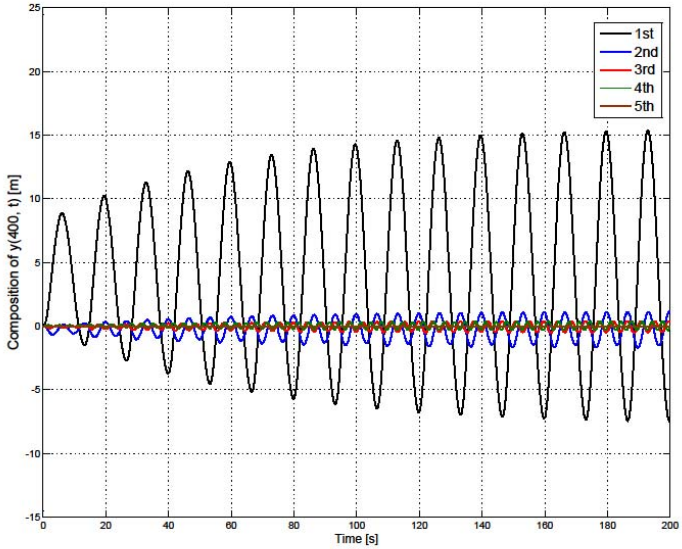

Fig. 5.17 The Decomposition of $y(400, t)$ for all System Natural Modes without Control

5.4.3. Simulation using Lateral Displacement Measurement

The control law $\Delta T_1(t) = \mu \frac{\partial y(x,t)}{\partial t}\Big|_{x=0.5L}$ is implemented in the simulation with proportional gain $\mu = 1.5 \times 10^6$ by "trial and error" method. The lateral vibration amplitude of the riser is examed at $x = 400m$ and $x = 750m$ respectively. The controlled (blue solid) and uncontrolled (black dash) results are shown in Fig. 5.18 and Fig. 5.19. It can be observed that the peak vibration amplitudes are reduced significantly at both locations. At $x = 400m$, the amplitude reduced from 22m to 5m. And at $x = 750m$, the amplitude reduced from 18m to less than 5m.

The time domain profile of the uncontrolled system shows that the vibration amplitude grows, the profile expands until it reaches the equilibrium point. By using the controller $\Delta T_1(t)$, the vibration profile does not expand. Instead, it converges as soon as the controller takes effect.

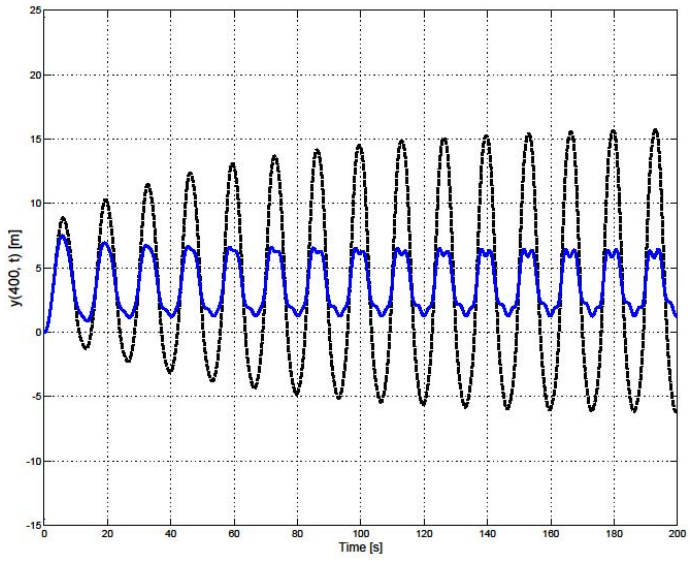

Fig. 5.18 Riser Displacement at $x = 400m$, With CGVC using Lateral Displacement Measurement or Estimation

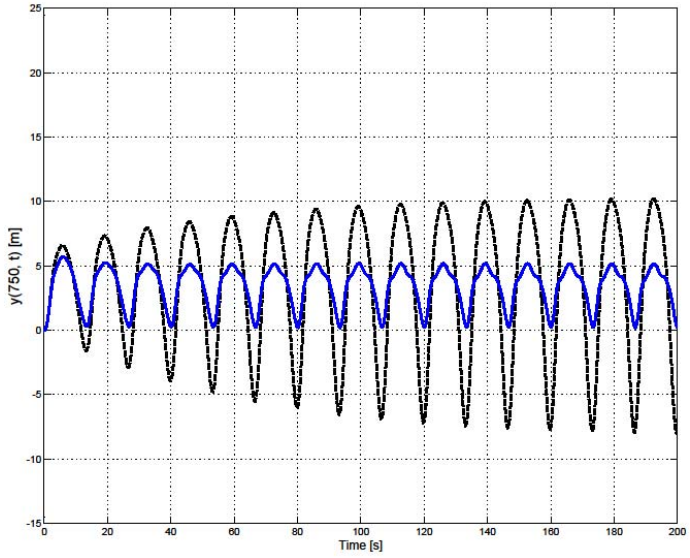

Fig. 5.19 Riser Displacement at $x = 750m$, With CGVC using Lateral Displacement Measurement or Estimation

In Fig. 5.20, it is shown that the first mode resonance has been reduced significantly, compared to Fig. 5.17. The first order resonance has less dominant influence on the shape of the actual resonance waveform, in Fig. 5.18 and Fig. 5.19.

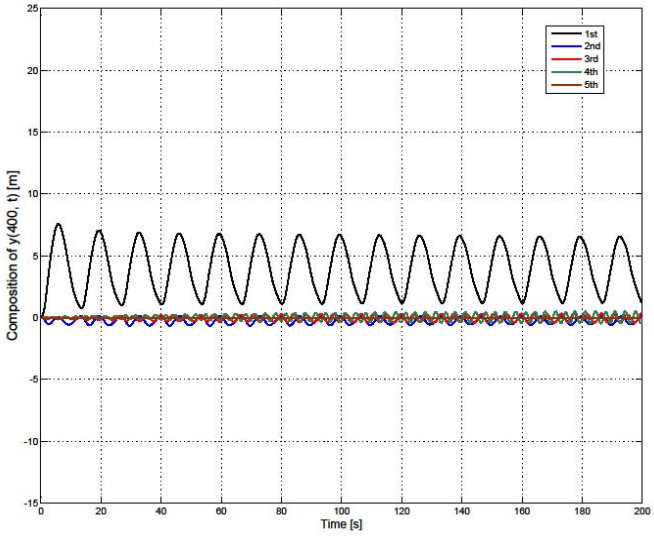

Fig. 5.20 The Decomposition of $y(400, t)$ for all System Natural Modes with CGVC using Lateral Displacement Measurement or Estimation

As the control input, the tension variation applied on top of the riser varies with the amplitude of 2.8×10^6 on both sides of the constant tension $T_0 = 9.0 \times 10^6$. For demonstration purpose, this tension variation is about 30% of the constant tension value, may be high with respect to the actual electrical machine capability. The engineer, who designs the tensioning system, may have more financial and dimensional concern for sizing the machine capacity. Depending on the rated maximum tension limit of the electrical machine, the proportional gain μ can be set lower. So the controller may have derated performance, but still providing effective control result.

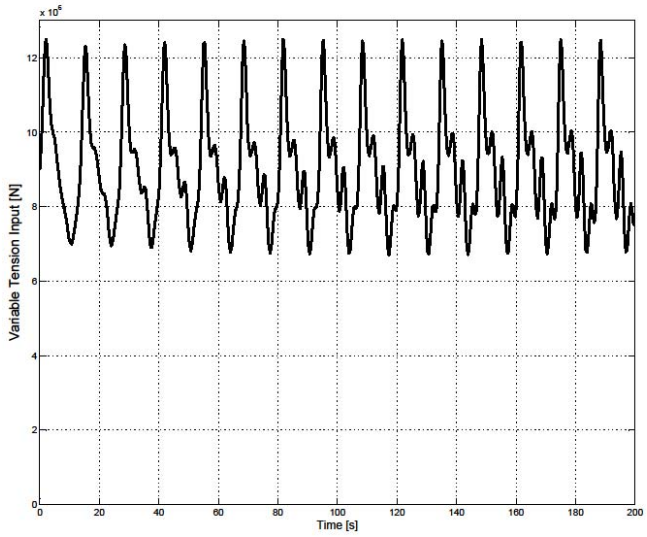

Fig. 5.21 The Tension $T_0 + \Delta T(t)$ applied on Riser Top with CGVC using Lateral Displacement Measurement or Estimation

5.4.4. Simulation using Longitudinal Position Measurement

The control law $\Delta T_2(t) = \sigma \frac{\partial h_{x=L}}{\partial t}$ is implemented in the simulation with proportional gain $\sigma = 5 \times 10^7$. The lateral vibration amplitude of the riser is examed at $x = 400m$ and $x = 750m$ respectively. The controlled (blue solid) and uncontrolled (black dash) results are shown in Fig. 5.22 and Fig. 5.23. It can be observed that the peak vibration amplitudes are reduced significantly at both locations. At $x = 400m$, the amplitude reduced from 22m to 3m. And at $x = 750m$, the amplitude reduced from 18m to 3m. The same principle as above, the controller $\Delta T_2(t)$ also converges the vibration, as soon as taking effect.

In Fig. 5.24, the first mode has been reduced even further than that of the previous control method. This means that when the first mode is less dominating mode shape, the other higher order mode shapes become more pronounced.

Fig. 5.25 shows the tension variation as the control input. The amplitude is around $2.3 \times 10^6 N$, which is 21% of the constant tension value. It indicates that in order to get this control performance, the tension variation is much less than the previous control method, using the lateral displacement measurement or estimation. Hence, this control method puts less stress on the electrical machine.

Fig. 5.26 shows that the riser profiles for uncontrolled and controlled responses under excitation were overlaid for different time instances. The riser lateral displacements are significantly reduced when either control is active. The method using longitudinal position feedback gives better control result while applying less control input. Hence, the VIV control above reduces the bending stresses of the riser and its auxiliaries, prevents fatigue damage and improves lifespan.

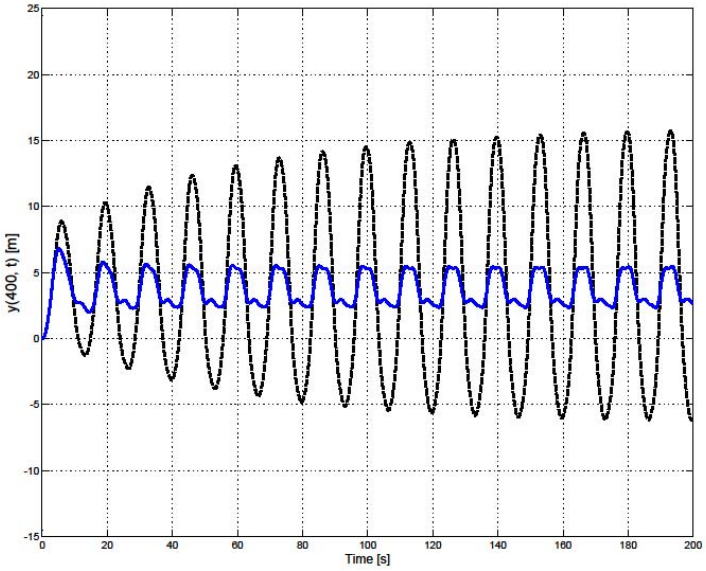

Fig. 5.22 Riser Displacement at $x = 400m$, with CGVC using Longitudinal Position Measurement

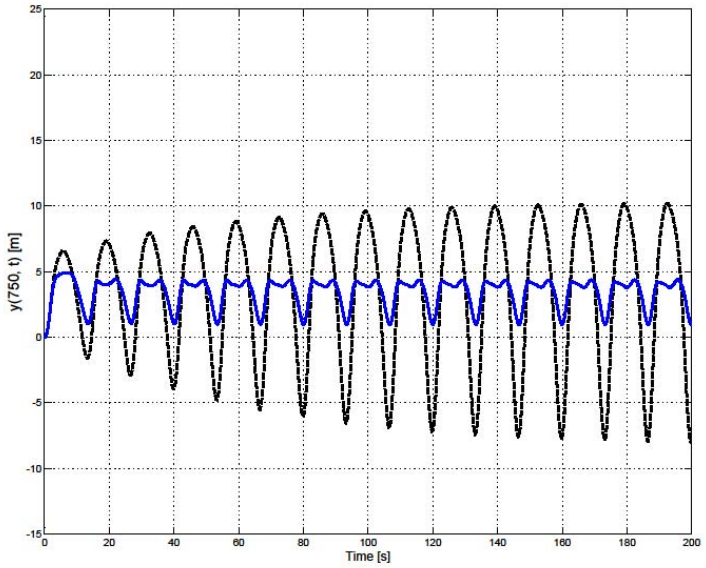

Fig. 5.23 Riser Displacement at $x = 750m$, with CGVC using Longitudinal Position Measurement

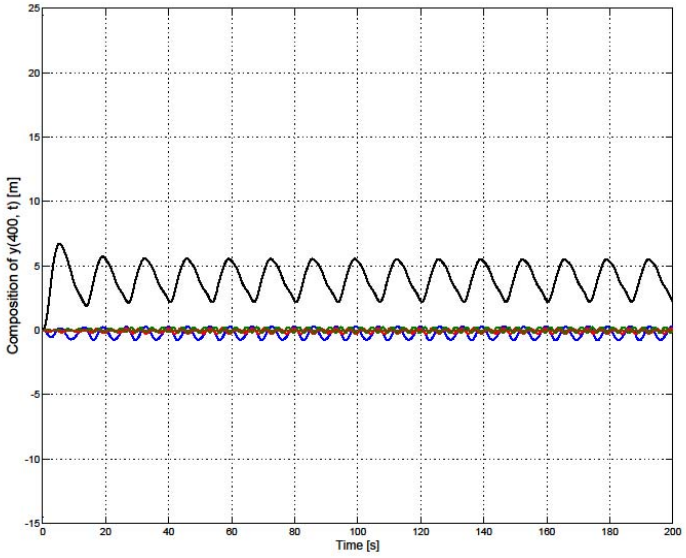

Fig. 5.24 The Decomposition of $y(400, t)$ for all System Natural Modes with CGVC using Longitudinal Position Measurement

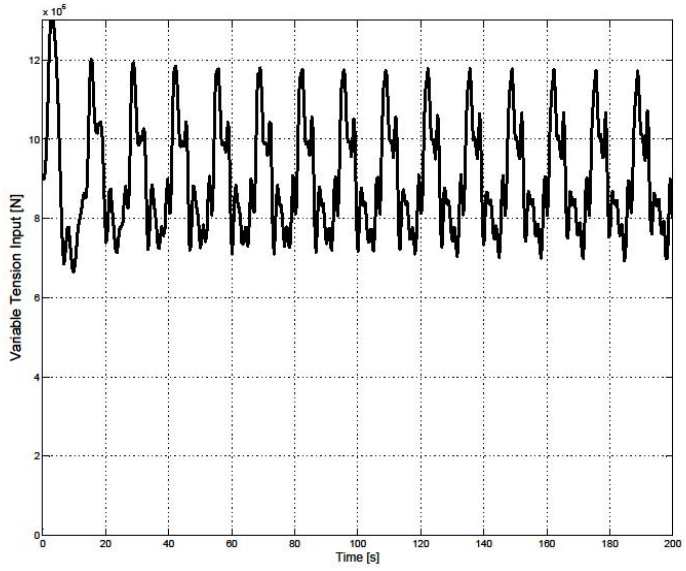

Fig. 5.25 The Tension $T_0 + \Delta T(t)$ applied on Riser Top with CGVC using Longitudinal Position Measurement

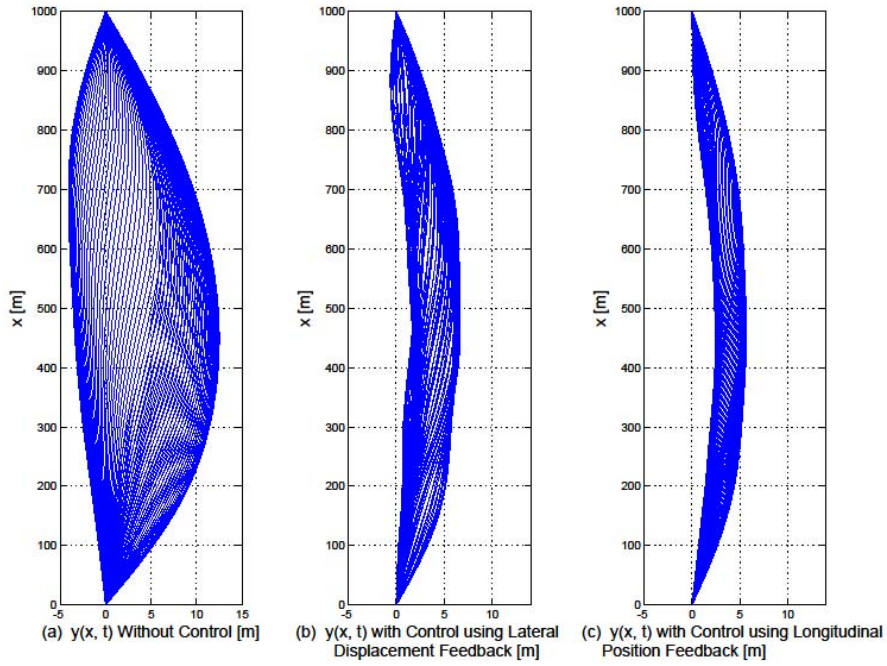

Fig. 5.26 Overlay of Riser Profiles

5.5. Conclusion and Discussion

A hydro-dynamic basic knowledge study has been carried out and a literature review has been studied in order to understand the current available control solutions of the Vortex-Induced Vibration. The control objective of these two methods is to prevent the riser system locking into the VIV condition or to reduce the VIV oscillation magnitude, by varying the applied top tension at frequencies and magnitudes made available by the electrical tensioning system. A mathematical model has been used and two control methods have been proposed and implemented in simulation.

The study carried out above demonstrates the fundamental idea and gives experimental exercise of the VIV control using variable top tension of the electrical tensioners. The simulations show satisfactory result, however, a lot of influencing factors need to be included in study, before putting the real system into service. The lifting force caused by ocean current

needs to be included in simulation. This requires a three dimensional riser model to be built. This model also is need to exam the interaction between the y and z axes. The longitudinal position of the riser top is now calculated assuming that the riser top is right above the wellhead. However, the vessel dynamics of floating rigs may have pronounced effect on the riser top longitudinal position. This needs to be included in the simulation study, to develop more accurate riser position acquisition for control.

Chapter 6: Motion Stabilizer for Drill Stem Test

6.1. The Conventional Motion Compensation Methods

The Drill Stem Test (DST) is usually performed to exam the pressure and permeability and the productive capability of the formation, after the well is drilled and cased. The test is important to determine if a well has found a commercial hydrocarbon reservoir. In the drill stem test, the drilling pipe is modified and includes a DST tool. This DST tool and the connected pipe or tubing must remain stationary with respect to the well. Since the rig or vessel holding the drill pipe is floating, there is a need to compensate for the motion of the vessel in the load path supporting the drill string. A Drill Stem Test can take many months to complete and the compensation system must operate reliably for the duration of the test. Failure of the compensation system can damage equipment, lead to activation of emergency counter measures and take considerable time to re-start the test.

Fig. 6.1 Drill String Compensator

Fig. 6.2 Drill String Compensator

In the industry, several ways are used to compensate for vessel motion, all of them involving a dedicated compensation system in the load path supporting the drill string. One of the common methods is using the drawworks to take up and pay out the cable supporting the drill

pipe or tubing in synchronism with the vessel movement. This is often called active compensation, as it actively uses electrical power to move the drawworks. Another common way is to use hydraulic pistons pressured by a large gas reservoir that maintains constant tension on the drill pipe or tubing. This is mounted in the derrick and is supported by the drawworks travelling block. This is called a drill string compensator, as shown in Fig. 6.1. A third method is to use hydraulic pistons pressured by a large gas reservoir in a special frame designed specifically to support the tubing used during the DST. This is called a Compensating Coil Tubing Lift Frame (CCTLF), as shown in Fig. 6.2.

6.2. The Novel Motion Compensation Method by using the Riser Tensioning System

A novel way to support the drill string such that it is stationary with respect to the well is to use the marine riser pipe as a support. The marine riser pipe is connected on the well head and is kept in tension by being pulled by nearly constant tension wires that are connected to the rig. The lower end of the riser is pinned to seabed and does not move with respect to the well. The top of this riser string does not move vertically with respect to the sea floor. By supporting the weight of the drilling pipe on this riser string, the drill pipe would also be stationary with respect to the sea floor.

Fig. 6.3 depicts the conceptual scheme. The method of supporting the drill pipe on the riser would include a new pipe holder that will suspend the drill string on the riser, so that the drill string is fixed on the riser and thus stationary with respect to the well. The riser tensioning system holds the weight of both riser and drill string. The transfer of the weight of the drill pipe or tubing is achieved by fitting to the pipe a load bearing device such that when the pipe is lowered, this load bearing ring connects to the riser and transfers the load to the riser. The weight of the drill string is usually less than 20% of the riser string of the same length. Use of a sensor pack on the riser allows the tension of the compensation tension wires to be automatically adjusted manage the load of the drill string. The pipe is then left supported by the riser. And

valves, instruments and a flexible tube are hard-connected to the stationary pipe with respect to the well, and are connected to the vessel such that vessel movement is allowed by the flexing of this connection hose.

6.3. The Benefits of this Novel Motion Compensation Solution

Since the drill string is suspended on the riser, other motion compensation systems such as the drawworks active heave compensation system or a compensated coil tube lift frame (CCLF) will not be used during the test.

Benefits of using the passive compensation of the riser tensioning system:

(1) reduces risk of a problem with the drawworks affecting the drill stem test;

(2) removes the requirement to mount CCLF;

(3) places the load of the drill string at a lower center of gravity improving rig stability and;

(4) leaves the drawworks available to manage other activities such as making up pipe or other inventory control matters;

(5) uses a reliable and existing compensating system that is in continuous duty while drilling.

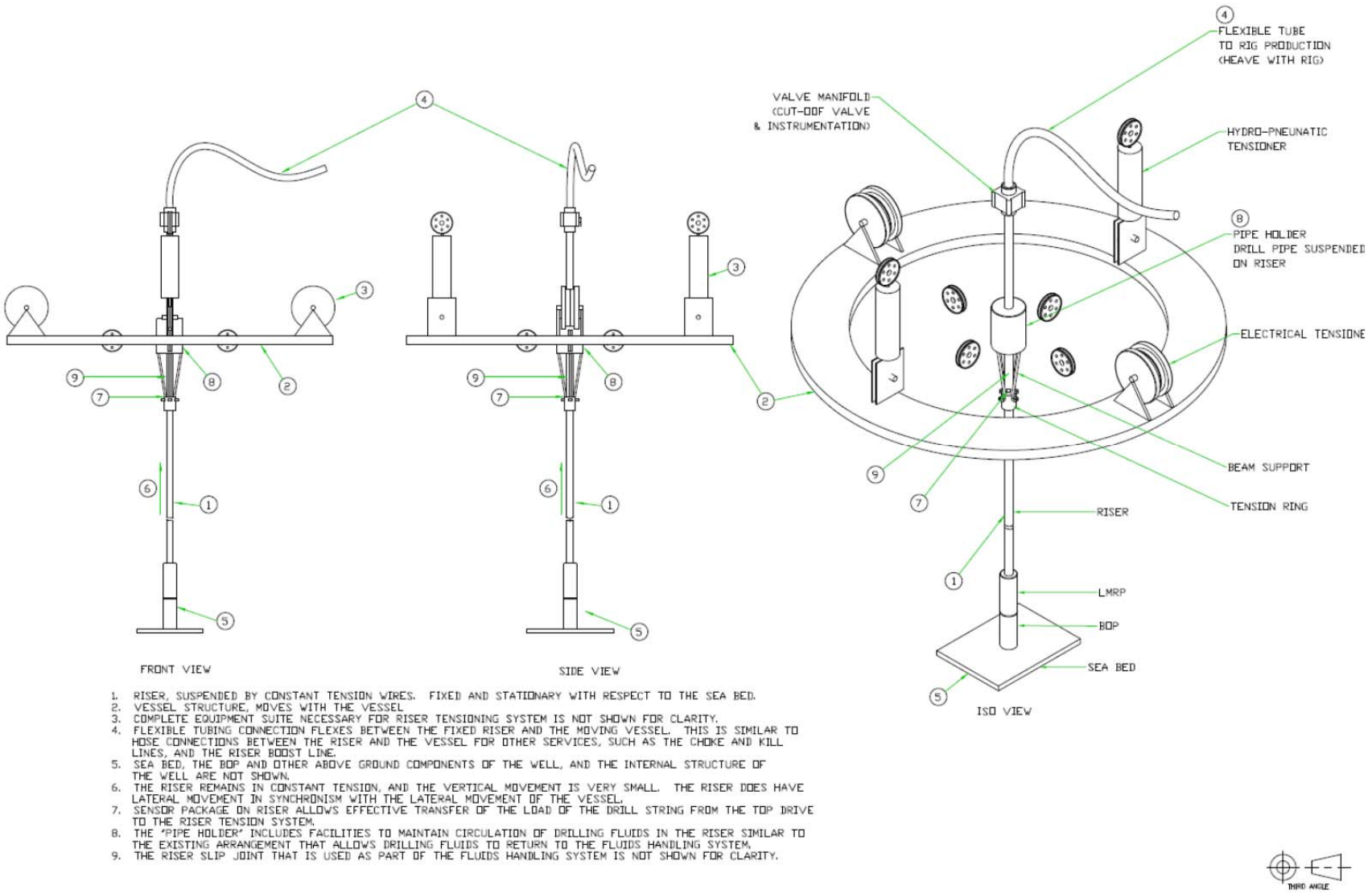

Fig. 6.3 Conceptual Scheme of the Riser Motion Compensation System for Drill Stem Test

Chapter 7: Conclusion

7.1. Summary

This dissertation discusses a systematic solution to the marine riser control system, with focus on the design of the riser hybrid tensioning system. This riser hybrid tensioning system is used to overcome the limited predictability and operability of the conventional hydro-pneumatic tensioners, and to extend the operability of the riser tensioning system into other operations.

The study starts with analyzing the existing barriers of the current hydro-pneumatic tensioner into deeper water operation. The proposed riser hybrid tensioning system provides the accessibility of the dynamically variable tension of the electrical tensioners with high accuracy. An overall structure framework is proposed, which comprises: (1) AFPM direct driven electrical tensioners, (2) hydro-pneumatic tensioners, (3) a super-capacitor based energy storage system, (4) a resistor type power dissipaters. A riser data logging system is introduced. It can work as an inertial navigation system installed on the riser top and closely monitors the riser status. Hardware topologies are suggested. The power management control strategy and the overall tension control architecture of this integrated hybrid riser tensioning system are proposed. Matlab simulation helps us to visualize and verify the performance of the hybrid riser tensioning system. The results show not only the promising improvement of control accuracy, but also the feasibility of the potential of wave energy generation.

As a main functionality of the riser tensioning system, the active heave compensation operation mode is analyzed in detail, using this new hybrid riser tensioning system. A LQG controller and a H_∞ controller are designed and implemented. Even the displacement of the tensioners are not controllable in the active heave compensation mode, the position chasing technique produces predictive and accurate tension commands for the electrical tensioners. The simulation demonstrates that the electrical tensioner is able to generate dynamically changed tension within mille-seconds, which compensates the tension fluctuation caused by the pressure change in hydro-pneumatic tensioners. Both Matlab simulation and hardware implementation

help us confirming the concept feasibility, and further verified that a more robust and accurate control performance could be achieved by this hybrid riser tensioning system.

A testability and predictability enhanced anti-recoil control algorithm is implemented, achieving a desirable dynamic position and velocity response profile. A system model integrating the riser string, the electrical tensioners and hydro-pneumatic tensioners is built for anti-recoil control design. Control boundary conditions are proposed. A position control strategy is proposed with the control objective of moving the riser body to a desired elevation height in a predictive manner. A linear feedback controller and a system state variable estimator are designed by using the Linear-Quadratic Gaussian method. The Matlab simulation helps to demonstrate the concept feasibility of this anti-recoil control. It also shows that the riser lifting height can be set to be adjustable for any test environment. This anti-recoil control design highly reduces the risk of catastrophic damage, allows us to perform the functionality tests much more often to bring back operator's confidence.

The VIV control mode is a new concept by using the dynamic control of the hybrid tensioning system, at frequencies and magnitudes made available by the electrical tensioning system. The dynamically changed riser top tension alternates the riser natural frequencies and material stiffness. This objective of VIV suppression is achieved by avoiding the excitation of the oscillation locking into the resonance conditions, and by avoiding oscillation energy to be built in riser. A modal analysis of a tensioned Euler-Bernoulli beam is studied and applied in the control design. Two control methods are proposed by using the lateral displacement and the longitudinal position measurement, respectively. Simulations results help to verify this control concept. The oscillation is effectively reduced at the dominant lock-in frequency. This control mode would reduce the down-time which carries huge amount of financial losses and increase the operability of drilling rig.

Furthermore, the hybrid riser tensioning system opens up a wide horizon of various riser control strategies from the top of the riser. It opens the possibility to extend the operability to other operations. A motion stabilizer supporting the heave compensation of the drill pipes and

the DST tools can be eliminated by connecting the drill pipes onto the telescopic joint. Another application would be that the electrical tensioners can run under position control mode after the riser is recoiled and soft hang-off on tensioners. The riser string position with respect to the seabed can still be controlled, during the vessel moving among different well heads.

7.2. Future Work

This work is focused on the conceptual proposal and computer realization of the riser hybrid tensioning system. The mathematical models used in each controller are design purpose oriented. Further model development should build a more comprehensive model which involves all the control objectives. A 3-D model and the state variable estimator are in need to be studied. The supervisory switched controller should be adapted for switching among different control modes.

Small scale experiments for every control modes will be conducted to gain confidence and proof the real operability of this system. Then higher scale comprehensive tests should be developed to eliminate all possible failure modes, before putting into real operation.

Appendix A

Due to the large size of this 3D model, please see the attached document: Riser Hybrid Tensioning System 3D Model.pdf

Appendix B

Due to the large size of the schematic, please see the attached document: Riser Tensioner Test Bench Schematics.pdf

References

[1] Chastain, T., and Stone, D, "Deepwater Drilling Riser System", SPE Drilling Engineering, Aug. 1986, pp 325-328.

[2] Control Flow, "120K Dual Riser Tensioning System with RIMAC", 2006.

[3] National Oil Varco, "N-Line Riser Tensioning System User Manual", 2010, T9601-Z-MA-001.

[4] Transocean, "Riser Recoil Analysis for the Discoverer Clear Leader", 2008.

[5] Hydralift Inc., "Functional Description of Hydralift Drilling Riser Tensioner System on Transocean Discover Enterprise", 1997.

[6] Gabbai, R.D. and Benaroya, H., "An overview of modeling and experiments of vortex-induced vibration of circular cylinders", J. of Sound and Vibration, 2005, Vol. 282, pp 575–616.

[7] Koch, S.P. and Barker, J.W., "The Gulf of Mexico Loop Current and Deepwater Drilling", J. of Petroleum Technology, 1991, Vol. 43, pp 1046-1119.

[8] Shaughnessy, J.M & Cleaver, M.A., 1999, "Problems of Ultra-Deepwater Drilling", SPE/IADC 1999-52782.

[9] Transocean, "Discoverer Clear Leader Emergency Disconnect Test Report", 2009.

[10] Reynolds, G., "Tensioner/Slip-Joint Assembly", 2003, Patent No. US 6,739,395 B2.

[11] Sten, R and Hansen, M," Force Variations on Heave Compensating System for Ultra-deep-water Drilling Risers', OMAE 2010-20011.

[12] Yin Wu, "A New Safety And Stability Enhanced Riser Control System - An Integrated Hybrid Riser Tensioning System", OMAE 2012-84235.

[13] Yin Wu, "Enhanced Active Heave Compensation Control Design for New Riser Hybrid Tensioning System in Deepwater Drilling", OMAE 2015- 41675.

[14] Yin Wu, "An Anti-Recoil Control Design using the New Riser Hybrid Tensioning System in Deepwater Drilling", OMAE 2015- 42022.

[15] Krishnan, R., "Permanent Magnet Synchronous and Brushless DC Motor Drives", 2010, CRC Press, FL, US, Chapter 1.

[16] Aydin, M., & Lipo, T. A., "Axial flux permanent magnet disc machines: A review", SPEEDAM, Capri, Italy, 2004

[17] Nasiri, Z. & Lesani, H, "A Survey on Axial Flux Induction Motors", PRZEGLĄD ELEKTROTECHNICZNY (Electrical Review), ISSN 0033-2097, R. 88 NR 2/2012

[18] Merzoug, M.S. & Naceri, F., "Comparison of Field-Oriented Control and Direct Torque Control for Permanent Magnet Synchronous Motor (PMSM)", 2008, World Academy of Science, Engineering and Technology.

[19] Maxwell Technologies, "Maxwell Technologies' Test Procedures for Capacitance, ESR, Leakage Current and Self-Discharge Characterizations of Ultra-capacitors", 2009.

[20] Maxwell Technologies, “Application Note - Mean Service Life Estimation: A Case Study”, 2009.

[21] William, K., “Flywheel-Based Energy Storage on a Heave-Compensation Drawworks”, 2009, Patent No. US 7,633,248 B1.

[22] Delrue, A., 2011, “The Application of Super-capacitors Based Energy Storage Systems on Heave Compensation Systems for Offshore Lifting Equipment”, OMAE 2011-49688.

[23] National Oil Varco, “Product Data Sheet of AHD-1000-6900-73 Drawworks”, 2006.

[24] Roodenburg, J., “Heave Compensation System and Method”, 2009, Patent No. US 2011/0100279 A1.

[25] Fossen, T.I., “Guidance and Control of Ocean Vehicles”, Wiley, New York, 1994.

[26] Lloyd, A.R.J.M., “Sea keeping Ship Behavior in Rough Weather”, Ellis Harwood Ltd, 1998.

[27] Nguyen, D. & Sorensen, A., “Switching control for thruster-assisted position mooring”, J. of Control Engineering Practice 17, pp 985-994, 2009.

[28] Konsberg, “Riser Management System – Advisory and Monitoring System”, September 2011

[29] Do, K. & Pan, J., “Nonlinear control of an active heave compensation system”, J. of Ocean Engineering, 2008, Vol. 35, pp 558–571.

[30] Do, K. & Pan, J., “High performance control of an active heave compensation system”, IFAC 2008, pp 5059-5064

[31] Leira, B. and Blanke, M., “Vertical position control for top tensioned riser with active heave compensator”, OMAE 2011-49778.

[32] TAMU, “Active Heave Compensator”, Ocean Drilling Program, www.oceandrilling.org

[33] Sebastian Kuchler, Tobias Mahl, J¨org Neupert, et al, “Active Control for an Offshore Crane Using Prediction of the Vessel’s Motion”, IEEE Trans. On Mechatronics, Vol.16, No. 2, pp 297-309.

[34] Li, L. and Liu, S, “Modeling and simulation of active-controlled heave compensation system of deep-sea mining based on dynamic vibration absorber”, IEEE International Conference on Mechatronics and Automation 2009, 1337-1341.

[35] Korde, Umesh, “Active heave compensation on drill-ships in irregular waves”, J. of Ocean Engineering, Vol. 25, Issue 7, July 1998, Pages 541–561.

[36] Leonhard, W., “Control of electrical drive”, Berlin: Springer, 1996.

[37] Novotny, W. and Lipo, T. A., “Vector control and dynamics of AC drives”. New York: Oxford University Press, 1996.

[38] Rustad, A., 2007, “Modeling and Control of Top Tensioned Risers”, Doctor Thesis of Norwegian University of Science and Technology, 2009.

[39] Hock, J. and Young, D., “Design Installation and Testing of a Deepwater Riser Emergency Disconnect Anti-Recoil System”, IADC/SPE23858, New Orleans, February 1992, pp.151-164.

[40] Young, R.D., and Hock, C.J., “Comparison of Analysis and Full-Scale Testing of Anti-Recoil System for Emergency Disconnect of Deepwater Riser”, OTC6892, Houston, May 1992, pp.173-182.

[41] Young, R. & Karlsen, G., “Analysis and Design of Anti-Recoil System for Emergency Disconnect of a Deepwater Riser: Case Study”, OTC 6891, Offshore Technology Conference, 1992.

[42] Hock, C.J. and Young, R.D., “A Deepwater Riser Emergency Disconnect Anti-recoil System”, J. of Petroleum Engineering, Vol. 45, No. 8, Aug, 1993.

[43] Stahl, M., & Hock, C, “Design of a Riser Recoil Control System and Validation Through Full-Scale Testing”, SPE 62959, Society of Petroleum Engineers, 2000.

[44] Stahl, M, “Controlling Recoil in Drilling Riser Following Emergency Disconnect”, ETCE2000/Drill-10105, Proceedings of ETCE/OMAE2000 Joint Conference, New Orleans.

[45] Stahl, M. & Brekke, J., “Riser Recoil Analysis at a Harsh Environment, Deepwater Site”, OMAE2004-51628, 2004.

[46] Yu, A., & Bhat, S., “Evaluation of Key Hydraulic Tensioner Performance Parameters for Ultra Deep Water Application”, OMAE2008-57465, 2008.

[47] Grytoyr, G. et al, “Marine Drilling Riser Disconnect and Recoil Analysis”, AADE-11-NTCE-80, American Association od Drilling Engineers, 2011.

[48] Suzuki, H & Tanaka, S., “Basic Research on an Anti-Recoil System of a Deepsea Riser”, The Society of Naval Architects of Japan, No. 186, pp 393-400, 2011.

[49] Lang, D., Lane, M., “Recent Development in Drilling Riser Disconnect and Recoil Analysis for Deepwater Application”, OMAE2009-79427, 2009.

[50] Grytoyr, G. et al, “Methodology for Disconnect Analysis of CWO Risers in Random Seas”, OMAE2009-79130, 2009.

[51] Control Flow, “120K Dual Riser Tensioning System with RIMAC”, 2006.

[52] National Oil Varco, “N-Line Riser Tensioning System User Manual”, 2010, T9601-Z-MA-001.

[53] Transocean, “Riser Recoil Analysis for the Discoverer Clear Leader”, 2008.

[54] ZInkgraf, H.L., O’Brien, M, “Smooth Block Control: Automation of Traveling Block Positioning Using Existing Drilling Equipment”, IADC/SPE 27514, 1994.

[55] National Oil Varco, “S01G8289-COM-001 - Rev 1 - Commissioning Procedure for Deepwater Thalassa”, 2015;

[56] National Oil Varco, “S01G8289-OPM-001 - Rev 0 - Operation Manual for Deepwater Thalassa”, 2015;

[57] National Oil Varco, “S01G8289-TD-001 - Rev 4 - Technical Description AHD for Deepwater Thalassa”, 2015;

[58] National Oil Varco, “S01G8289-TDO-002 - Rev 0 - Technical Document for Deepwater Thalassa”, 2015;

[59] Williams, D. et al, “Optimization of Drilling Riser Operability Envelopes for Harsh Environments”, OTC-20775, 2010.

[60] Bizzi, E., Hogan, N., “Posture Control and Trajectory Formation During Arm Movement”, the journal of neuroscience, Vol. 4, No.11, pp. 2738-2744, 1984;

[61] Wang, W.J., & Hsu, C., “Experiments on the Position Control of a One-Link Flexible Robot Arm”, IEEE Transactions on Robotics and Automation, Vol. 5, No. 3, 1989;

[62] Cannon, R., et al, “Initial Experiments on the End-Point Control of a Flexible One-Link Robot”, the International Journal of Robotics Research, Vol. 3, No. 3, 1984;

[63] Skogestad, S. and Postlethwaite, I., “Multivariable Feedback Control Analysis and Design”, England: Joh

[64] Grytoyr, G., “Improving Operating Window for Disconnect Operations of CWO Risers”, OMAE2010-20976, 2010.

[65] Aaron Barr, “N-Line Tensioner Riser Recoil Modeling Practice”, Transocean, 2014

[66] Kumar, R & Sohn, Chan-Hyun, “Passive Control of Vortex-Induced Vibrations: An Overview”, Recent Patents on Mechanical Engineering 2008, Vol. 1, No. 1.

[67] American Petroleum Institute, “Recommended Practice for Design, Selection, Operation and Maintenance of Marine Drilling Riser Systems”, API 16Q RP, 1993.

[68] Dulhunty, P.W.: US20040035601A1 (2004).

[69] Dulhunty, P.W.: US 6943290 (2001).

[70] Taggart, S. and Tognarelli, M.A., “Offshore Drilling Riser VIV Suppression Devices – What’s available to Operators?”, OMAE2008-57047, 2008.

[71] Lie, H.: US20070215028A1 (2007).

[72] Allen, D.W., Henning, D.L.: US20016223672B1 (2001).

[73] Coakley, D.B., Knutson, R.K.: US20036517289B1 (2003).

[74] Trim, A.D., “Experimental Investigation of Vortex-Induced Vibration of Long Marine Risers”, J. of Fluids and Structures, 2005, Vol. 21, No. 3, pp 335-361.

[75] Vandiver, J.K., “Research Challenges in the Vortex-Induced Vibration Prediction of Marine Risers.”, OTC-8698, 1998.

[76] Zhang, M. M., “Control of Vortex-Induced Non-Resonance Vibration using Piezo-ceramic Actuators Embedded in a Structure”, J. of Smart Materials and Structures, 2005, Vol. 14, No. 6, pp 1217-1226.

[77] Baz, A. and Ro, J., “Active Control of Flow-Induced Vibrations of a Flexible Cylinder using Direct Velocity Feedback”, J. of Sound and Vibration, 1991, Vol. 146, No. 1, pp 33-46.

[78] Howells, H, 1998, “Deep Water Drilling Riser Technology, VIV & Fatigue Management”, 4th Quarter Meeting of Drilling Engineering Association.

[79] Choo Y.S. et al., “Active control of flexible marine risers”, J. of Sound and Vibration, 2008, Vol. 320, pp 758–776.

[80] Choo Y.S. et al. “Boundary control of a coupled nonlinear flexible marine riser”. IEEE Trans. on Control Systems Technology, 2010, Vol. 18(5), pp 1080–1091.

[81] Choo Y.S. et al. “Robust Adaptive Boundary Control of a Flexible Marine Riser With Vessel Dynamics”, J. of Automatica, 2011, Vol. 47, No. 4, pp 722-732.

[82] Sparks, C.P., “Transverse Modal Vibrations of Vertical Tensioned Risers – A Simplified Analytical Approach”, J. of Oil & Gas Science and Technology, 2002, Vol. 57, No. 1, pp. 71-86.

[83] Muddada, S. & Patnaik, B, “An active flow control strategy for the suppression of vortex structures behind a circular cylinder”, European Journal of Mechanics/Fluid 29, 2010, 93-104.

[84] Meliga, P & Chomez, J.M., “Extracting energy from a flow: an asymptotic approach using vortex-induced vibrations and feedback control”, J. of Fluids and Structures 27, 861 – 874.

[85] Mehmood, A, Abdelkefi, A. et al, “Piezoelectric energy harvesting from vortex-induced vibrations of circular cylinder”, J. Sound and Vibration 332, 2013, 4656-4667.

[86] Venkatraman, K. & Narayanan, S., “Active Control of Flow-Induced Vibration”, J. of Sound and Vibration 162, 1993, 43-55.

[87] Baz, A., “Active modal control of vortex-induced vibrations of a flexible cylinder”, J. of Sound and Vibration 165(1), 1993, 69-84.

[88] Baz, A. & Poh, S., “A Demonstration of Adaptive Least-Mean-Square Control of Small Amplitude Vortex-Induced Vibrations”, J. of Fluids and Structures 10, 615-632, 1996.

[89] Carbonell, P., et al, “On the suppression of flow-induced vibration with a simple control algorithm”, J. of Communications in Nonlinear Science and Numerical Simulation 8, 2003, 49-64.

[90] Cheng, L., Zhou, Y, et al, “Perturbed interaction between vortex shedding and induced vibration”, J. of Fluids and Structures 17, 2013, 887-901.

[91] Chen, Z. & Aubry, N., “Closed-loop control of vortex-induced vibration”, J. of J. of Communications in Nonlinear Science and Numerical Simulation 10, 2005, 287-297.

[92] Li, B., Liu, Y., et al, “Vortex-Induced Vibration Control by Micro Actuator”, J. of Mechanical Science and Technology 21, 2007, 1408-1414.

[93] Wu, W, et al, “Multi-high-frequency Perturbation Effects on Flow-induced Vibration Control”, J. of Sound and Vibration 305, 2007, 226-242.

[94] Wu, X., Ge, F., Hong, Y., “A Review of Recent Studies on Vortex-Induced Vibrations of Long Slender Cylinders”, J. of Fluids and Structures 28, 2012, 292-308.

[95] Marshall, K. D., “Modal Analysis of a Violin”, J. of Acoustic Society 77, 1985, 695.

[96] Kamran Koushan, "Vortex Induced Vibrations of Free Span Pipelines", Ph.D. Thesis, Norwegian University of Science and Technology, 2009.

[97] Blevins, R. D., "Flow Induced Vibrations", Van Nostrand, New York, 1977.

[98] Sarpkaya, T. and Isaacson, M. "Mechanics of Wave Forces on Offshore Structures", Van Norstrand, New York, 2010.

[99] W. Weaver, S. Timoshenko, D Young, "Vibration Problems in Engineering", Wiley, New York, 1990.

[100] Furnes, G., "On Marine Riser Responses in Time and Depth Dependent Flows", J. of Fluids ad Structures, 2000, 14 257-273.

[101] Virgin, L, "Effects of Axial Loads on Forced Vibration of Beams", J. of Sound and Vibration, 1993, 142(3) 481-489.

[102] Tolbert, L & Lee, S, "Analytical Method of Torque Calculation for Interior Permanent Magnet Synchronous Machines", IEEE Energy Conversion Congress and Exposition, 2009, 173-177.

[103] Shaharuddin, N., Darus I., "Active Vibration Control of Marine Riser", IEEE Conference on Control, Systems and Industrial Informatics", 2012.

[104] Shaharuddin, N., Darus I., "Fuzzy-PID Control of Transverse Vibrating Pipe due to Vortex Induced Vibration", 15th International Conference on Computer Modeling and Simulation, 2013.

[105] Kitada, K. & Expedition 332 shipboard science party, "Vortex Induced Vibration Suppression of the Drill Pipe for te Long-Term Borehole Monitoring System Installation", IEEE Symposium on Scientific Use of Submarine Cables and Related Technologies, 2011.

[106] Graichen, K. & Kugi, A., "Suboptimal Model Predictive Control of a Laboratory Crane", IFAC Symposium on Non Linear Control Systems, 2010

[107] Van den Broeck, L. & Swevers, J., "A Model Predictive Control Approach for Time Optimal Point-to-Point Motion Control", Journal of Mechatronics 21, 2011, pp 1203-1212.

[108] Graichen, K. & Kapernick, B., "Model Predictive Control of an Overhead Crane Using Constraint Substitution", American Control Conference 2013.

Vita

Yin Wu was born in China in 1980. She received the Diploma of Engineering in Industrial Automation Control from the École Polytechnique Universitaire de Lille, France in 2006. She received the first Master of Science degree in Electrical Engineering from Hohai University, China in 2006 and the second Master of Science degree in Energy System from the University of Texas at Austin in 2013. She enrolled in the Ph.D. program in Electrical Engineering at the University of Texas at Austin in 2007. And In 2010, she joined the Transocean Deepwater Drilling Inc. as a staff electrical engineer, where she was engaged in the high reliability power system design for offshore marine vessel application. She is currently a senior electrical design engineer. Her research interests include offshore marine vessel power system, riser tensioning system, drilling riser system, subsea drilling operation, linear and non-linear control theory.

Email Address: wuyin2000@gmail.com

This dissertation was typed by the author.